Model-based design of MEMS resonant pressure sensors

Citation for published version (APA):
Suijlen, M. A. G. (2011). *Model-based design of MEMS resonant pressure sensors*. [Phd Thesis 1 (Research TU/e / Graduation TU/e), Applied Physics and Science Education]. Technische Universiteit Eindhoven. https://doi.org/10.6100/IR716458

DOI:
10.6100/IR716458

Document status and date:
Published: 01/01/2011

Document Version:
Publisher’s PDF, also known as Version of Record (includes final page, issue and volume numbers)

Please check the document version of this publication:

• A submitted manuscript is the version of the article upon submission and before peer-review. There can be important differences between the submitted version and the official published version of record. People interested in the research are advised to contact the author for the final version of the publication, or visit the DOI to the publisher's website.
• The final author version and the galley proof are versions of the publication after peer review.
• The final published version features the final layout of the paper including the volume, issue and page numbers.

Link to publication

General rights
Copyright and moral rights for the publications made accessible in the public portal are retained by the authors and/or other copyright owners and it is a condition of accessing publications that users recognise and abide by the legal requirements associated with these rights.

- Users may download and print one copy of any publication from the public portal for the purpose of private study or research.
- You may not further distribute the material or use it for any profit-making activity or commercial gain
- You may freely distribute the URL identifying the publication in the public portal.

If the publication is distributed under the terms of Article 25fa of the Dutch Copyright Act, indicated by the “Taverne” license above, please follow below link for the End User Agreement:

www.tue.nl/taverne

Take down policy
If you believe that this document breaches copyright please contact us at:

openaccess@tue.nl

providing details and we will investigate your claim.

Download date: 15. May. 2025

Model-based design of MEMS resonant pressure sensors

PROEFONTWERP

ter verkrijging van de graad van doctor aan de Technische Universiteit
Eindhoven, op gezag van de rector magnicus, prof.dr.ir. C.J. van Duijn, voor
een commissie aangewezen door het College voor Promoties, in het
openbaar te verdedigen op maandag 29 augustus 2011 om 16.00 uur

door

Matthijs Alexander Gerard Suijlen

geboren te Gouda

De documentatie van het proefontwerp is goedgekeurd door de promotoren:

prof.dr. H.C.W. Beijerinck
en
prof.dr. P.J. French

Copromotor:
dr.ir. J.J. Koning

Druk: BOXPress BV, Oisterwijk
ISBN: 978-90-8891-306-8
NUR: 926

Trefwoorden: MEMS resonator / MEMS life-time testing / resonant pressure sensor / free molecular flow / Monte Carlo simulation / squeeze-film damping

Contents

Chapter 1

Introduction

1.1 MEMS technology

Birth

Following its release in the early 1950s the transistor revolutionized the field of electronics, and launched an extensive industry for miniaturized electronic circuits. It replaced the bulky vacuum tubes customary to amplifying and switching signals until then. Today the transistor is the fundamental building block of modern electronic devices, and is ubiquitous to daily life technology. Obviously industry has undergone a tremendous development to create this massive spread. The major contribution arguably is the integration of circuit components in one and the same substrate material. Fifty years ago, Jack Kilby from Texas Instruments gave the outset to this integration with his primevally integrated circuit of a phase-shift oscillator [1]. He looked for a solution known as ”The Monolithic Idea” in which circuit elements as resistors, capacitors, distributed capacitors and transistors are all included in a single chip of semiconductor material. The integrated circuit’s mass production capability, reliability, and building-block approach to circuit design ensured the rapid adoption of standardized ICs in stead of designs using discrete transistors.

There are two main advantages of ICs over discrete circuits: cost and performance. Cost is low because the chips, with all their components, are printed as a unit by photolithography rather than being constructed one transistor at a time. Moreover, much less material is used to construct a packaged IC die than a discrete circuit. Performance is high since the components switch quickly and consume little power (compared to their discrete counterparts) because the components are small and positioned close together. As of 2010, chip areas range from a few to many tens of square millimeters, with up to three million transistors per mm^2 (IBM z196 microprocessor) [2].

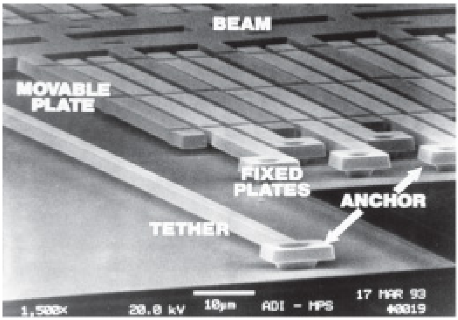

Figure 1.1: MEMS accelerometer structure of Analog Devices.

Besides IC processing the available microfabrication technology nowadays offers machining of mechanical elements, like cantilevers and membranes in or over chip substrates (Fig. 1.1). These small elements can be integrated with electronics to form, so called micro-electromechanical systems or MEMS. Here the mechanical structure interacts with an electronics environment to convert mechanical into electrical signals and vice versa. The massive integration of these structures on ICs to allow microsystems to sense and control the environment is expected to be one of the most important technological breakthroughs of the future. Over the past several decades MEMS researchers and developers have demonstrated an extremely large number of microsensors for almost every possible sensing modality including temperature, pressure, inertial forces, chemical species, magnetic fields, radiation, etc.

Micromachining

For machining mechanical parts on the microscale a wealth of techniques is available. In the context of MEMS these techniques concern etching processes for the removal of silicon in a substrate or thin film. Silicon has excellent mechanical properties [3] making it an ideal material for machining. An early silicon sensor was made by Honeywell in 1962 by using isotropic etching [4]. In 1966 Honeywell developed a technique to fabricate thin membranes using mechanical milling. Crystal orientation dependent etchants led to more precise definition of structures and increased interest [5]. Anisotropic etching was introduced in 1976 and applied for the processing of an early silicon pressure sensor by Greenwood [6] in 1984. Today, wet anisotropic etching of the silicon substrate is the most mature technology and the most widely used process for the fabrication of mechanical microstructures for commercially available microsensors, such as pressure sensors and accelerometers. The relatively high etch rates that can be achieved, the low cost due to the low complexity equipment, the availability of masking materials for selective processing are among the major reasons for the large use of wet silicon etching.

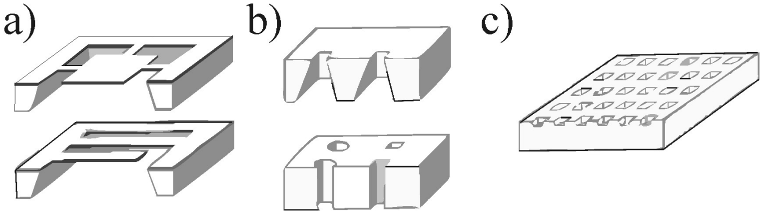

Figure 1.2: Typical bulk micromachined structures: a) membranes and beams, b) wafer-through holes, b) microwells.

If significant amounts of the substrate (bulk) material must be removed to release a functional structure, the application of etching processes results in *bulk micromachining*. Bulk micromachining can be accomplished using chemical or physical means, with chemical means being far more widely used in the MEMS industry. Typical bulk micromachined structures, like wafer-through holes for interconnects in chip stacks and cavities/channels to form reservoirs for biochemical applications, are shown in Fig. 1.2.

Another very popular technology used for the fabrication of MEMS devices is *surface micromachining*. Contrary to bulk micromachining, the formation of microstructures is not realized by etching for silicon *removal* in the wafer. It involves the deposition of *additional* layers on the wafer surface and selectively removing one or more of these layers to leave free-standing structures. There are a very large number of variations of how surface micromachining is performed, depending on the materials and etchant combinations that are used. However, the common theme involves a sequence of steps (Fig. 1.3) starting with the deposition of some thin-film material to act as a sacrificial layer onto which the actual device layers are built; followed by the deposition and patterning of the thin-film device layer of material which is referred to as the structural layer; then followed by the removal of the sacrificial layer to release the mechanical structure layer from the constraint of the underlying

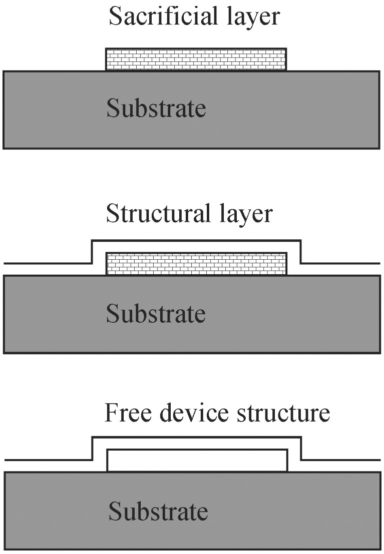

Figure 1.3: Basic surface micromachining process.

layer, thereby allowing the structural layer to move.

Some of the reasons surface micromachining is so popular is that it provides for precise dimensional control in the vertical direction. This is due to the fact that the structural and sacrificial layer thicknesses are defined by deposited film thicknesses which can be accurately controlled. As a result of the commonly high fidelity of the photolithography and etch processes, surface micromachining also provides for precise dimensional control in the horizontal plane. Other benefits of surface micromachining are that a large variety of structure, sacrificial and etchant combinations can be used; some are compatible with microelectronics devices to enable integrated MEMS devices. Surface micromachining frequently exploits the deposition characteristics of thin-films such as conformal coverage using LPCVD. Lastly, surface micromachining uses single-sided wafer processing and is relatively simple. This allows higher integration density and lower resultant cost per die compared to bulk micromachining.

Benefits

By far miniaturization is often the main driver of MEMS development. The common perception is that miniaturization reduces cost, by decreasing material consumption and allowing batch fabrication, but an important collateral benefit is also in the increase of applicability. Actually, reduced mass and size allow placing the MEMS in places where a traditional system would not be able to fit. Finally, these two effects concur to increase the total market of the miniaturized device compared to its costlier and bulkier predecessor. A typical example is found in the accelerometer developed as a replacement for traditional airbag triggering sensor and that is now used in many appliances, as in digital cameras to help stabilize the image or even in the contactless game controller integrated in the latest cellphones. However often miniaturization alone cannot justify the development of new MEMS. After all if the bulky component is small enough, reliable enough, and particularly cheap then there is probably no reason to miniaturize it. Micro-fabrication process cost cannot usually compete with metal sheet punching or other conventional mass production methods.

But MEMS technology allows something different, at the same time you make the component smaller you can make it better. The airbag crash sensor gives us a good example of the added value that can be brought by developing a MEMS device. Some non-MEMS crash sensors are based on a metal ball retained by a rolling spring or a magnetic field. The ball moves in response to a rapid car deceleration and shorts two contacts inside the sensor. A simple and cheap method, but the ball can be blocked or contact may have been contaminated. Moreover, when your start your engine, there is no easy way to tell if the sensor will work or not. MEMS devices can have a built-in self-test feature, where a micro-actuator will simulate the effect of deceleration and allow checking the integrity of the system every time you startup the engine. Another advantage that MEMS can bring relates with the system integration. Instead of having a series of external components (sensor, inductor...) connected by wire or soldered to a printed circuit board, the MEMS on silicon can be integrated directly with the electronics. Whether it is on the same chip or in the same package it results in increased reliability and decreased assembly cost, opening new application opportunities. As we see, MEMS technology not only makes the things smaller but often makes them better.

Drivers

From the heyday of MEMS research at the end of the 1960s, one main driver for MEMS development has been the automotive industry. It is really amazing to see how many MEMS sensor a modern car can use! From the first oil pressure sensors, car manufacturers quickly added manifold and tire pressure sensors, then crash sensors, one, then two and now up to five accelerometers. Recently the gyroscopes made their apparition for anti-skidding systems and vehicle navigation – the list seems without end. Miniaturized pressure sensors were also quick to find their ways in medical equipment for blood pressure testing. Since then biomedical applications have attracted a lot of attention from MEMS developers. The DNA chip and micro total analysis system (μTAS) are the latest successes in the list. Because you usually sell medical equipment to doctors and not to patients, the biomedical market has many features making it perfect for MEMS: a niche market with large added value.

Actually cheap and small MEMS sensors have many applications. Digital cameras have been starting using accelerometers to stabilize image, or to automatically find image orientation. Accelerometers are also being used in new contactless game controllers. These two latter products are just a small part of the MEMS-based systems that the computer industry is using to interface digital input-output with our human senses. The inkjet printer, DLP based projector, head-up display with scanner mirror are all MEMS based computer output interfaces. Additionally, computer mass storage uses an abundant amount of MEMS, for example, hard-disk drives nowadays consist of a micromachined GMR head and dual stage MEMS micro-actuator. Of course in that last field more innovations are in the labs, and most of them use MEMS as the central reading/ writing element.

The telecommunication industry has fueled the biggest MEMS R&D effort so far. Especially the wireless telecommunication business is using more and more MEMS components to deal with the demand for ever increasing functionality of portable devices on the one hand and their limited size and battery capacity on the other hand. MEMS are slowly sipping into cellphones replacing discrete elements one by one, RF switch, microphone, filters – until the dream of a 1 mm^3 cellphone becomes true (with vocal recognition for numbering of course!). The latest craze is in using accelerometers (again) inside cellphones to convert them into game controllers, the ubiquitous cellphone becoming even more versatile.

Finally, it is in spacecraft that MEMS are finding an ultimate challenge and already some MEMS sensors have been used in satellites. The development of micro (less than 100 kg) and nano (about 10 kg) satellites is bringing the mass and volume advantage of MEMS to good use and some projects are considering swarms of nanosatellites populated with micromachined systems.

In spite of the interest for numerous new (exotic) sensing applications, MEMS technology arguably has even more significance to system integration and miniaturization of existing microelectronic building blocks. An emerging class of MEMS takes on this challenge for the ubiquitous reference oscillator [7, 8, 9]. This element is used for a wide range of applications varying from keeping track of real-time, setting clock frequency for digital data transmission, frequency up- and down conversion in RF transceivers, and clocking of logic circuits. It involves a multi-billion dollar market in today's electronic industry.

1.2 MEMS oscillators

Oscillator technologies for mainstream electronic applications are either based on mechanical or electrical resonance [10]. Mechanical resonators are typically made from a piezo-electric material such as quartz onto which a pair of metal electrodes is placed to allow for energy transfer between the mechanical domain – the resonator – and the electrical domain: the feedback amplifier for sustaining the oscillation. The oscillation frequency is set by the physical dimensions of the resonator body and the position of electrodes on it.

One of the properties setting mechanical resonators apart from electrical resonators is a high quality factor (Q) which is imperative to make oscillators with low noise level work. A mechanical resonator material known of old for its pronouncedly high quality factor is the quartz crystal. Thanks to this property and a very high stability – for certain crystal cuts – of the resonance frequency to temperature change, quartz based oscillators have become known for coupling superior accuracy to minimal temperature drift and noise [11]. Quartz is the technology of choice where oscillator noise and stability are most demanding such as for wireless communication (e.g. GSM, Bluetooth), but also high-speed digital serial-interfaces (e.g. USB2.0, real-time clocks).

The Q-factor, stability, and temperature drift of ceramic resonators made from e.g. barium titanate or lead-zirconium titanate tends to be smaller than for quartz, but ceramic resonators are cheaper to produce [12]. Therefore, ceramic resonators are used for applications where frequency stability and noise is less of a concern, but where the oscillator performance nevertheless cannot be met with electrical oscillators. Ceramic resonators are mainly used in consumer applications such as remote controls, digital audio/video, and household appliances.

Although the electrical performance of mechanical oscillators cannot be met by electrical oscillators, mechanical oscillators have some important drawbacks that prevent their use in every application. Mechanical resonators are relatively bulky and cannot be embedded in the IC chip. Combining them with the chip package that provides more space, on the other hand, would increase the manufacturing complexity and cost too much. Therefore, mechanical resonators have to interface with other circuit components on board level and therefore form a bottleneck for the ultimate miniaturization of the electronic system.

On the other hand, oscillators based solely on electronic components such as resistor-capacitor (RC), inductor-capacitor (LC), or ring oscillators can be integrated on CMOS chips. However, their use is limited to applications, e.g. processor clocks, were accuracy and noise specification is relaxed. Their stability and near-carrier noise can be improved by locking them to mechanical oscillators using a phase-locked loop (PLL). However, this requires again a bulky off-chip component adding to the total size and cost of the system.

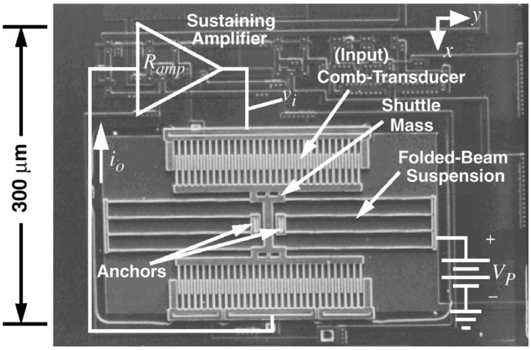

Figure 1.4: SEM picture of a fully integrated 16-kHz watch timekeeper oscillator that combines CMOS and MEMS in a single fully planar process [13].

The extraordinary small size, high level of integration and high volume manufacturing capability that is possible with MEMS, opens exceptional possibilities for creating miniature-scale precision oscillators at low cost. Such a miniature oscillator either can be integrated on the IC die or be combined as a separate die in a single low cost plastic package with the remaining electronics. Because of its high-Q mechanical resonance, it can be expected that a MEMS based oscillator has a superior noise performance and frequency stability compared to electrical oscillators.

The replacement of a quartz resonator with a MEMS resonator and integrating the MEMS resonator with the drive electronics in a single package or die will lead to a reduction in form factor, board complexity, and bill-of-materials of electronic circuits. Here, the device of Nguyen and Rowe [13] (Fig. 1.4) with its resonator structure and electronics in a single fully planar process shows how far integration can go. Simultaneously, the MEMS solution will have an improved electrical performance compared to LC, RC, or other types of oscillators based on electrical rather than mechanical resonance. These unique attributes reduce the size and cost of existing electronic systems, and might open up new application domains, e.g. wireless sensor nodes [14] or other products requiring extreme form factor such as SIM and smartcards.

1.2.1 MEMS resonator packaging

As MEMS oscillators need vacuum conditions in the sub-mbar range for proper and reliable operation of the resonator, the packaging process of these devices must provide direct caps to the resonators that seal them hermetically. The resonators are brought in evacuated cavities by sealing them in a vacuum environment. The end pressure inside the package then is expected to equal the pressure level of this sealing environment. Two process families can be distinguished for the batch fabrication of these microcavities [10].

The most mature method is based on the bonding of two wafers [15]. In this case, the wafer containing the MEMS resonator has a seal ring which fits to a facing ring on the capping wafer. A cavity is created around the resonator after bonding the two wafers together. For further processing the different resonators are singulated from the wafer. Although wafer-to-wafer bonding is a relatively mature technique that is also used for the packaging of e.g. accelerometers and gyroscopes, it has the disadvantage that a large amount of valuable wafer area is required for the sealing ring. This not only results into a large product, but also increases the manufacturing cost since fewer resonators per wafer can be processed. Furthermore, the height of the packaged resonator is set by the combined thickness of two wafers. Therefore, wafer bonding sealing can lead to a package size that is many times the size of the resonator residing inside the cavity.

A more advanced on-wafer sealing method leading to a much smaller package is based on surface micromachining. A schematic process flow for the fabrication of the resonator cap is shown in Fig. 1.5. Here sacrificial layer etching and coating techniques are used to create a microcavity around the resonator. The advantage of surface micromachining is that the size of the cavity is only slightly larger than the size of the resonator itself. As a result, die size remains small which will lead to a cost benefit, since a large amount of devices can be processed onto a single wafer. The height of the sealed resonator is now set by the thickness of a single wafer instead of the combined thickness of two wafers in case of wafer-to-wafer bonding.

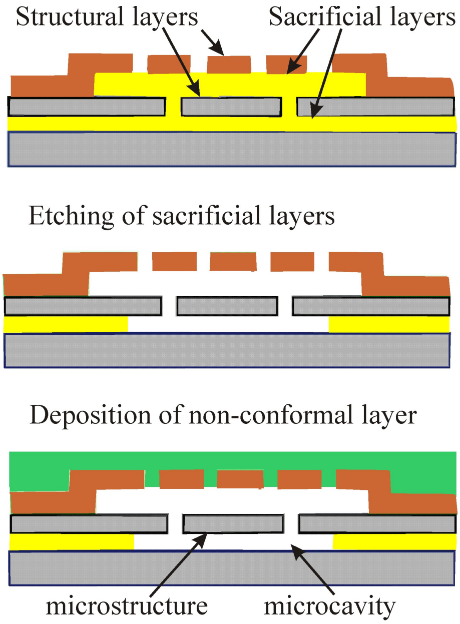

Figure 1.5: A conceptual process flow of creating a thin film package around a MEMS device.

The wafer containing the sealed resonators has the outer dimensions and bond pad layout as any ordinary CMOS wafer and can therefore be handled in standardized CMOS assembly lines for grinding, dicing, and plastic over molding of the MEMS die. As a result, the MEMS die can be thinned down to small fractions of a millimeter using standard silicon grinding processes without any special effort. This is considerable thinner than what presently can be achieved with ceramic or metal can packages used for quartz resonator and can be a key differentiating property when these resonators are integrated in thin objects such as SIM cards, smartcards or identification tags.

Given the huge market potential of these and related applications for timing, the semiconductor company NXP with a rich tradition in manufacturing specialistic microelectronics is developing a MEMS oscillator based on this packaging concept. Here, a dog-bone shaped structure machined in a thin silicon surface layer (Fig. 1.6a) is excited to resonate in the fundamental bulk mode. Accordingly, the plates of the structure will vibrate in the plane of the substrate (Fig. 1.6b). This type of resonance typically results in a maximum amplification of the driving input signal, which is key to stable oscillator function at the lowest power levels. In the fashion of the proces suggested in Fig. 1.5, a thin film seals the resonator hermetically from the atmosphere and maintains the minimum required vacuum level for the resonator. A first protoype has been successful [16], but still a lot of effort is needed to industrialize the defined design. One of the challenges concerns testing of the reliability for the projected life-time of the system.

1.2.2 Diagnostics for advanced life-time testing

As a loss of vacuum in the MEMS cavity would end the proper operation of the resonator, life-time testing of cavity vacuum levels is very important to conclude about the reliability of the device. For this job the method of standard leak detection is

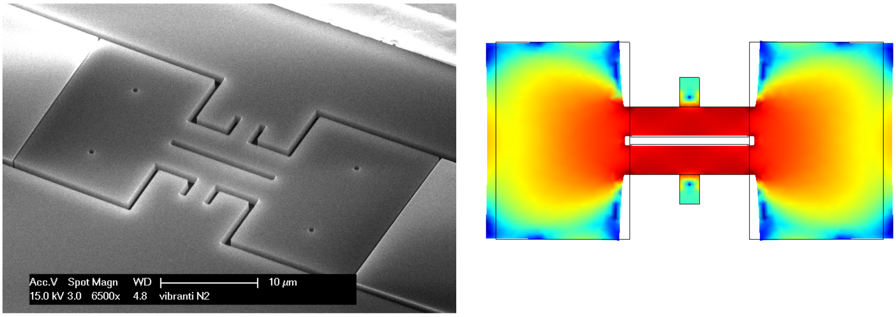

(a) SEM picture of processed structure.

(b) Result of eigenmode simulation showing the deformation during in-plane vibration.

Figure 1.6: NXP's dog-bone shaped resonator for high frequency timing purposes processed in silicon-on-insulator (SOI). This structure is intended to perform high frequency in-plane resonant oscillation.

rather insensitive and absolute pressure sensors may be integrated in the wafer-level packaging for in-situ testing of the cavity vacuum. Waelti et al. [17] and Mailly et al. [18] for example present some solutions with dedicated sensors in the package based on measurement of the thermal conductivity of the residual gas. At the millibar range vacuum pressures in typical cavities, this conductivity is directly proportional to the gas density which enables measurement of absolute pressure. These wafer-level Pirani-type pressure sensors exist in many geometrical and read-out implementations that can be tailored to a wide range of sensitivities either with or without linear response behavior. See for example Li et al. [19] for a state-of-the-art sensor design.

All these solutions however disregard the resonator structure itself as pressure sensor. After all, the trouble about vacuum packaging follows from the resonator's susceptibility to gas pressure in the first place. Given this principle sensitivity, caused by the momentum transfer between resonator structure and gas molecules, the realization of a pressure sensor with specified sensitivity and range is all a matter of design. In the ideal case, a read-out of the common characteristics in resonant operation (quality factor and resonance frequency) of the resonator sample could be sufficient to measure the absolute cavity pressure without any additional structures and signal conversion!

1.2.3 PhD on design

Motivated by the need of diagnostics for advanced life-time testing of thin-film packaged MEMS resonators, a project for the conceptual design (in Dutch 'proefontwerp') of such resonant pressure sensors was initiated at the NXP production and innovation center in Nijmegen. After a project with preliminary design results performed at this center as part of preceding education [20], work was continued at the laboratories of NXP Research in Eindhoven. Activities were an integral part of NXP's business case to develop MEMS oscillators on 1.5 μm SOI substrates [21]. The output of the PhD on design project includes several device prototypes, two invention disclosures [22, 23], a contributed talk at the Eurosensors XXII conference [24] and new diagnostic measurement methods. The focus of this thesis is on the presentation and evaluation of the actual designed/invented processes or devices.

By chance, NXP agrees with a wide dissemination of the results in the thesis. Also, the knowledge developed in the present project connects to a timely field of study in the open literature. For this reason, the chapters in the body of this thesis are written in the format of a journal paper, for future publication in scientific journals. This will bring our findings out into the open beyond the current network at TU/e and NXP. The text of chapter 2 has been published in "Sensors and Actuators A", Ref. [25]; chapter 3 was submitted lately to the same journal but was not accepted for publication due to a lack of comparison of our model results with other models in literature. A fully revised version, splitting up the model calculations and the experimental results in two separate papers, is foreseen in the future.

Chapter 4, which has been added at a very late stage of writing the thesis, still needs major work to qualify as a manuscript for a journal (e.g., adding references to literature). For the purpose of providing sufficient insight in the process of design, its current shape is acceptable. Because it deals with the role of gas species in our model thus and directly connects to chapter 3, this sets a certain order in time on its publication.

1.2.4 This thesis

Modeling and simulation of the forces that the gas exerts on the resonator structure plays a major role for this design task. If the approach should be used in industry, values of pressure sensitivities for every version designed need to be available without time-consuming measurements. Also specifying the spread in pressure sensitivity of resonators due to process spread in the design parameters calls for proper modeling. Absolute accuracy in this respect is not as important as efficiently gaining clear insights in the physical processes involved.

The narrow gaps of resonators cause a strong coupling of microstructure movement with the flow of residual gas and the emerging *squeeze-film* forces turn out to be the determining gas-structure interaction in typical resonators. Quantitative prediction of the gas flow and resulting forces involves in existing *squeeze-film* models generally a highly specialistic programming effort and this seriously complicates proper design activities. Therefore we developed a new, semi-analytical model that can live up to the standards of efficient designing. It is revealed and validated in chapters 2, 3 and 4 of this thesis.

Building on the knowledge and ideas from all our experiments, chapter 5 presents an analysis and evaluation of our design solution to sensitive cavity vacuum testing in MEMS resonators. It illustrates and supports the method and sensor design we claimed in the patent application of Ref. [26]. The result shows pressure sensing with the resonator is useful to life-time testing during fabrication and model-based design of MEMS resonant pressure sensors is a reality. Next, chapter 6 discusses with a comparison of published data on the squeeze-film damping for different resonator designs the value of our model to generic resonator design.

Finally, chapter 7 concludes and summarizes this thesis.

Bibliography

[1] J.S. Kilby, IEEE Trans. Electron Devices **23** (7) 1976.

[2] Shvets, Anthony, ”IBM is ready to ship the fastest microprocessor,” `CPU-World.com`, (September 5, 2010).

[3] K.E. Petersen, Proc. IEEE 70 (1982), 420-457.

[4] O.N. Tufte, G.D. Long, J. Appl. Phys. **33** (1962), 3322.

[5] K.E. Bean, IEEE Trans. Electron Devices **25** 1978, 1185-1193.

[6] J.C. Greenwood, Rev. Sci. Instrum. **17** (1984), 650-652.

[7] C.T. Nguyen, IEEE Trans. UFFC **33** 2007, 251-270.

[8] C.S. Lam, Proc. IEEE Ultrasonics Symposium (IUS) 2008, 694-704.

[9] W.-T. Hsu, Proc. 40th Ann. Precise Time and Time Interval (PTTI) Meeting 2008, 135-146.

[10] J.T.M. van Beek, R. Puers, ”A review of MEMS oscillators for frequency reference and timing applications,” 2010, to be published.

[11] M.E. Frerking, Proc. IEEE Int. Freq. Control. Symp. 1996, 33-46

[12] S. Fujishima, IEEE Trans. UFFC **47** 2000, 1-7.

[13] C. T.-C. Nguyen and R. T. Howe, IEEE J. Solid-State Circ. **34** (4) (1999) 440-455.

[14] C.C. Enz, J. Baborowski, J. Chabloz, M. Kucera, C. Muller, D. Ruffieux, N. Scolari, Proc. European Conference on Circuit Theory and Design (ECCTD) 2007, 320-331.

[15] R. Pelzer, H. Kirchberger, P. Kettner, Proc. Int'l Conf. Electronic Packaging Technology (ICEPT) 2005, 1-6.

[16] J.J.M. Bontemps et al., Digest Tech. Papers Transducers 2009 pp 1433-1436.

[17] M. Waelti, N. Schneeberger, O. Paul, H. Baltes, Int. J. Microcircuits and Electronic Packaging **22** (1) (1999) 49-56.

[18] F. Mailly, N. Dumas, N. Pous, L. Latorre, O. Garel, E. Martincic, F. Verjus, C. Pellet, E. Dufour-Gergam, P. Nouet, Sens. and Actuators A **156** (2009) 201-207.

[19] Q. Li, J.F.L. Goosen, J.T.M. van Beek, F. van Keulen, Sens. Actuators A **162** (2010) 267-271.

[20] M.A.G. Suijlen, ”Ontwerp MEMS druksensor: rapport ontwerpproject NXP Nijmegen”, Final report Stan Ackermans Institute TU/e, 2007.

[21] J.J.M. Bontemps, ”Design of a MEMS-based 52 MHz oscillator,” PhD thesis TU/e, 2009.

[22] M.A.G. Suijlen, J.J. Koning, H.C.W. Beijerinck, ”Monolithic spring damped pressure sensor,” ID81380938 NXP, 2009.

[23] M.A.G. Suijlen, J.J. Koning, H.C.W. Beijerinck, ”Molecular mass detection of a gas using a spring damped resonant pressure microsensor,” ID81410650 NXP, 2010.

[24] M.A.G. Suijlen, J.J. Koning, M.A.J. van Gils, H.C.W. Beijerinck, Proc. Eurosensors XXII, Dresden, 2008.

[25] M.A.G. Suijlen, J.J. Koning, M.A.J. van Gils, H.C.W. Beijerinck, Sens. Actuators A **156** (2009) 171-179.

[26] Matthijs Suijlen, Jan-Jacob Koning, Herman Coenraad Willem Beijerinck, ”MEMS pressure sensor,” patent application US2011/0107838 A1.

Chapter 2

Squeeze film damping in the free molecular flow regime with full thermal accommodation

Abstract

We introduce an analytical model for the gas damping of a MEMS resonator in the regime of free molecular flow. Driving force in this model is the change in density in the gap volume due to the amplitude of the oscillating microstructure, which is counteracted by the random walk diffusion in the gap that tries to restore the density to its equilibrium value. This results in a complex-valued force that contributes to both the damping as well as the spring constant, depending on the value of $\omega\tau$ with ω the resonance frequency and τ the random walk diffusion time. The diffusion time is calculated analytically using the model for random walk Brownian motion and numerically by a Monte Carlo simulation of the ballistic trajectories of the molecules following Maxwell-Boltzmann statistics and full thermal accommodation in gas-surface collisions. The model is verified by comparison to accurate data on the pressure dependency of the damping of three MEMS resonators, showing agreement within 10 %.

1 Introduction

In the study of the dynamic behavior of MEMS devices, damping forces resulting from surrounding air generally play a significant role. As the most commonly used technologies are capacitive sensing and electrostatic driving, for which narrow air gaps often result, the so-called squeeze film effect dominates the interaction of the surrounding air with the moving part of a MEMS device. This effect refers to the pumping action of a fluid between closing up parallel surfaces with a gap much smaller than their dimensions. It exceeds the drag force on the MEMS part that would be experienced in isolated motion considerably. Current descriptions of squeeze film air damping are derived considering a continuum fluid picture of the flow in the squeeze film [1, 2, 3]. In many MEMS, however, squeeze film flow cannot be regarded as continuum-like. Gases trapped in the MEMS cavity often are so rarefied that the molecular mean free path exceeds the gap dimensions by at least an order of magnitude and flow becomes 'free molecular'. In this regime, intermolecular collisions in the gap volume are increasingly rare. Thus the way to meaningfully describe the interaction of MEMS parts with the gas is to consider the sum of all individual wall collisions. Momentum is transferred between the gas molecules and the surface by ballistic trajectories and wall collisions. For a stationary device, kinetic gas theory shows that the net effect of the momentum transfer in all these collisions equals the pressure forces exerted on the surface.

For a non-stationary device such as a MEMS oscillator, simple kinetic gas theory again can be applied, showing an extra contribution to the force exerted on the surface which is proportional to the plate velocity $|\vec{V}|$ and counteracts the movement. This is mostly referred to as kinetic damping. It can be easily understood if we consider the simplified case of an elastic collision. Ballistic molecules hit the moving surface with a relative velocity that is larger (or smaller) by an amount $|\vec{V}|$, resulting in an extra contribution to the momentum transfer as compared to the stationary situation. Kinetic damping always occurs and is not unique for a MEMS device with a small gap volume.

The effect of kinetic damping is rather small and models based on this effect [4, 5, 6, 7, 8] underestimate experimental values of the gas damping observed in MEMS devices [9]. Several approaches have been used to resolve this discrepancy. Of these approaches, the model of Bao et al. [10] is most relevant for our purpose of establishing an analytical model, as it explicitly appeals to the molecular motion of the flow in the gap. It shows reasonable agreement with experimental observations of air damping on resonators with a beam-like geometry [11] with a large length-to-width ratio. However, to explain all the kinetic energy losses of the plate, Bao introduces an extra transfer of momentum beyond the normal molecule-surface interaction. For this mechanism, he chooses the phenomenon of large number of consecutive elastic collisions, adding $2m\,V_z$ to the molecule's momentum after each collision with the plate. Here, the z-direction coincides with the velocity vector $\vec{V}$ of the oscillating plate. Even if, once in a while, a single elastic collision would occur, it is extremely unlikely to suppose that a sequence of hundreds of these collisions would occur.

Considering the large body of data on the nature of collisions of molecules with surfaces (see for example references 25-27 of Martin et al. [12]), we have to conclude that practically all collisions happen to be inelastic. The relevant number is the accommodation coefficient that is always close to unity for all (industrial) surfaces in a moderate vacuum. This implies that, every time a molecule hits a wall, the molecule's state is lost and reset to a new random state distributed according to Maxwell-Boltzmann statistics. For example, even in highly sophisticated beam-surface collision experiments under conditions of ultra-high vacuum, it requires a major effort (baking at high temperature, sputtering, dips before entering the vacuum) to clean the (single crystal) surface before the phenomenon of elastic collisions is observed. Full thermal accommodation is the rule, elastic collisions are the exception.

2 Squeeze film damping

In this paper we consider the increase in density of the gas in the gap volume as the driving force for the squeeze film damping in the regime of free molecular flow. When the gap height decreases due to the plate movement, we see that the volume below the plate decreases accordingly. This results in a corresponding increase in number

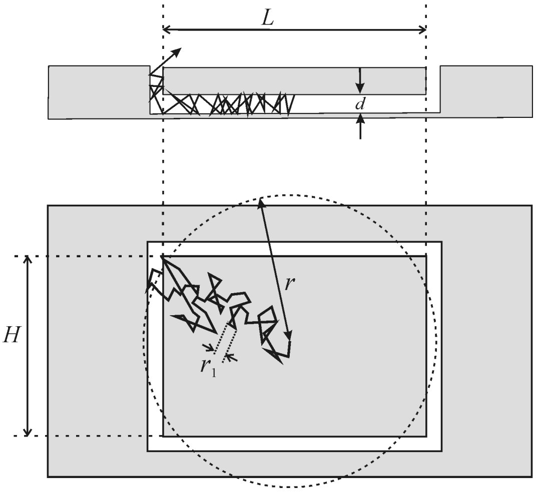

Figure 1: In-plane diffusion by single molecule random walk in a MEMS cavity

density. In an alternative picture, we can also state that the frequency of collisions with the plate increases correspondingly, due to the shorter gap crossing time of each molecule. These pictures are equivalent, as we expect from the molecular picture of Boyle's law. A different value of the number density results in a different pressure exerted on the plate. The net effect of this change in pressure (or number density) depends on its phase as compared to the phase of the oscillating plate.

The in-phase component just acts as an extra contribution to the spring constant of the suspension of the plate. The out-of-phase component of the change in pressure (or number density) acts as a damping force for the plate. This is independent of the model for the molecule-surface interaction – elastic or full accommodation. On the single molecule level, each collision has the same role of reversing the momentum of the molecule perpendicular to the surface, as is the case when it hits the wall of a vacuum chamber. No particular molecular kinetics need to be considered. Until now, this effect has not been considered for modeling the squeeze film interaction in the free molecular flow regime.

Because the gas will not move instantaneously, the phase shift is induced by the time constant τ of the molecular diffusion to equalize the pressures in- and outside the gap. For high oscillation frequencies $\omega \gg 1/\tau$, the diffusion cannot respond to the increasing density and we expect that the squeeze film will only influence the spring constant. For low oscillation frequencies $\omega \ll 1/\tau$, the density in the gap volume can respond and the 90° phase shift in the density variations with respect to the amplitude

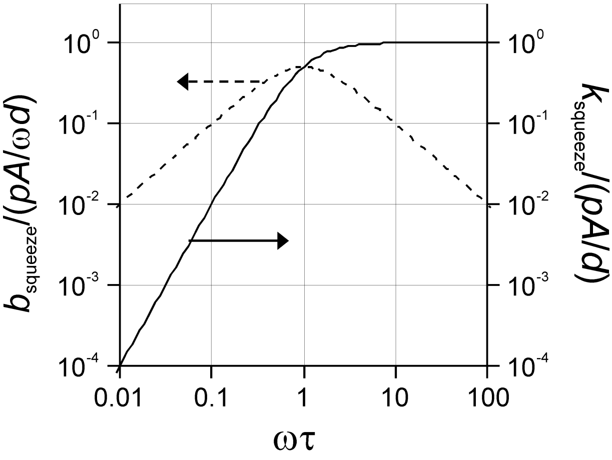

Figure 2: Frequency dependence of the elastic force constant and the damping constant due to the squeeze film interaction.

z will result in extra damping of the microstructure.

In section 3 we derive an analytical model for squeeze film damping based on this behavior. We also compare the results for the damping to the predictions of kinetic damping, showing that the first effect is much larger than the latter. Experiments on three MEMS oscillators are presented in section 4 showing a behavior that is in agreement with the model predictions. The pressure dependent damping coefficient is used to derive reliable values of the diffusion time τ.

In sections 5 and 6 we describe the diffusion of the molecules in the gap volume, applying full thermal accommodation in molecule-wall interactions. The molecules will perform a random walk in the cavity, bouncing up and down between microstructure and substrate and erratically zigzagging along its trajectory as projected in the plane of the device. This is illustrated in Fig. 1. Our analysis is substantiated both in the theoretical framework used to describe random walk in Brownian motion and in a fully numerical Monte Carlo simulation of the individual gas molecules.

With the validity of our model established in section 7 we put the good agreement of the damping on the microbeam resonator of Zook [11] with Bao's model in perspective.

3 Model

3.1 Squeeze force damping

The increase in density of the gas in the gap volume is the driving force for the squeeze film damping in the regime of free molecular flow. The density variation $\Delta n(t)$ in the gap volume is governed by the differential equation

$$\frac{\mathrm{d}}{\mathrm{d}t}\left(\frac{\Delta n}{n}\right) = -\frac{1}{\tau}\frac{\Delta n}{n} - \frac{\mathrm{d}}{\mathrm{d}t}\left(\frac{z}{d}\right), \tag{1}$$

with τ the random walk diffusion time, n the equilibrium value of the density, and z the coordinate pointing up from the plate (cf. Fig. 1) with $z = 0$ corresponding to its equilibrium position. The equation describes the rate of change in density, as counteracted by the random walk diffusion (first term) and driven by the displacement z of the plate (second term). Assuming a forced plate oscillation with displacement $z(t) = z_0\, e^{i\omega t}$ and a trial solution $\Delta n(t)/n = (\Delta n_0/n)\, e^{i\omega t}$ with complex amplitude, we find

$$\frac{\Delta n(t)}{n} = -\frac{z(t)}{d}\,\frac{i\omega\tau}{i\omega\tau + 1}. \tag{2}$$

In case of isothermal density variations $\Delta n(t)$, the force exerted on the plate is given by

$$F_{\text{squeeze}} = \Delta n(t)\, k_{\text{B}}\, T\, A = \Delta p(t)\, A, \tag{3}$$

with $\Delta p(t)$ the increase in pressure in the gap volume and A the frontal area of the moving plate. Combining Eqs. (2) and (3) the squeeze force F_{squeeze} of the gas in the cavity on the moving plate thus satisfies

$$F_{\text{squeeze}} = -\frac{p\,A}{d}\,\frac{i\omega\tau}{1 + i\omega\tau}\, z, \tag{4}$$

consisting of a real and imaginary contribution. The squeeze force F_{squeeze} has to be inserted into the differential equation of the damped harmonic oscillator describing the plate motion. The real part of the force F_{squeeze} is in counter-phase with the amplitude z and results in an extra contribution $-k_{\text{squeeze}} z$ to the elastic force on the oscillating mass m of the MEMS; the imaginary part of F_{squeeze} is out of phase with the amplitude z, i.e., in counter-phase with the velocity $\dot{z}$, and results in an additional damping $-b_{\text{squeeze}}\dot{z}$. The differential equation can now be written as

$$m\ddot{z} + b\dot{z} + kz = F_0\, e^{i\omega t} \tag{5}$$

with

$$b = b_{\text{mat}} + b_{\text{squeeze}} \tag{6}$$

$$k = k_{\text{mat}} + k_{\text{squeeze}}. \tag{7}$$

Here, b_{mat} and k_{mat} represent the inherent damping and stiffness of the mechanical structure. The contributions due to the complex valued squeeze force are given by

$$b_{\text{squeeze}} = \frac{p A \tau}{d} \frac{1}{1 + (\omega\tau)^2} \tag{8}$$

$$k_{\text{squeeze}} = \frac{p A}{d} \frac{(\omega\tau)^2}{1 + (\omega\tau)^2}. \tag{9}$$

In a plot of these parameters versus frequency ω (Fig. 2), one can clearly see the character of the squeeze film interaction: for low frequency oscillations, $\omega \ll 1/\tau$, it manifests itself as pure damping force and for rapid oscillations, $\omega \gg 1/\tau$, it becomes an elastic force without damping. These results show how we can optimize the design of MEMS resonators. E.g., for an application as a pressure sensor, we have to choose $\omega\tau = 1$ for maximum sensitivity. To avoid a shift in the operating frequency, we can choose $\omega\tau = 0.3$, with a slight trade-off in maximum sensitivity. Conversely, to use a frequency shift as pressure read-out instead of the change in quality factor, we can choose $\omega\tau > 3$ as range of operation.

Alternatively, similar results for the damping coefficient b_{squeeze} and spring constant k_{squeeze} are obtained when solving the density profile in the gap $n(x, t)$ in the time domain from the common diffusion equation. The diffusion coefficient D then functions as the inverse random-walk diffusion-time $1/\tau$ from Eq. (1). Instead of the mean free path λ of the molecules to estimate the diffusion coefficient one has to use the gap width d here, being by far the smallest of the two in the regime investigated.

3.2 Kinetic damping

The squeeze force damping has to be compared to the kinetic damping b_{kin} due to momentum transfer of the molecules impinging on the surface of the plate. This damping effect is always effective at conditions of free molecular flow, irrespective of the specific geometry of the plate and its surroundings. Both surfaces of the plate contribute. Christian [13] has shown that

$$b_{\text{kin}} = (16/\pi)(pA/\langle v\rangle), \tag{10}$$

with $\langle v\rangle$ the average velocity of the gas molecules and p the equilibrium value of the pressure. Neglecting the pressure variations in the gap is fully justified for inspecting the influence of kinetic damping, because this is a only a second order effect.

Comparing this result to squeeze film damping at $\omega\tau \ll 1$, where the ω-dependency disappears, we find

$$b_{\text{squeeze}}/b_{\text{kin}} = (\pi/16)\langle v\rangle/v_{\text{geom}} \, , \tag{11}$$

with $v_{\text{geom}} = d/\tau$ an effective velocity that depends on the geometry of the resonator plate. For MEMS resonators, typical values of the gap width d are in the 1 to 3 µm range. The diffusion time is on the order of 0.1 to 0.5 µs, as we will show in the following sections 4, 5 and 6. Thus $2\ \text{m/s} < v_{\text{geom}} < 30\ \text{m/s}$ which should be compared to typical molecular velocities, with $\langle v\rangle = 471\ \text{m/s}$ for N_2 at room temperature. We conclude that for typical MEMS resonators in the range $\omega\tau < 1$ squeeze damping dominates by far over kinetic damping. For $\omega\tau \gg 1$ the squeeze damping decreases proportional to $(\omega\tau)^{-2}$ and the kinetic damping is finally the only remaining effect.

4 Experiments

To test the model, we have investigated the pressure dependency of the damping coefficient of three different resonators. These devices were designed as switches with a low stiffness suspension and thus a low resonance frequency. By chance, they are well suited to test our model of squeeze film damping. The devices consist of a rectangular aluminum plate supported by cantilever beams above the substrate. The plate is provided with $18 \times 18\ \mu\text{m}^2$ sized etch holes in a 50 µm pitch, square grid. These etch holes have been used for the sacrificial etch to open the gap. The gap distance between plate and substrate is $d = 3\ \mu\text{m}$ for all devices. The substrate is coated with a thin metallic layer. The devices are labeled '8×8', '8×4' and '8×2', referring to their etch hole grid. The characteristic dimensions are given in Tab. 1. The frequency $\omega_{0,\text{mat}}$ and spring constant k_{mat} are derived from a finite element simulation of the device using "COMSOL Multiphysics". In this calculation the spring constant k_{mat} is defined by equating the total strain energy $U_{\text{strain}}(t)$ of the microstructure to $\frac{1}{2}k_{\text{mat}}\, z_{\text{max}}(t)^2$, with $z_{\text{max}}(t)$ the maximum value of the microstructure's deflection at time t. In Fig. 3 we show the actual layout of the devices and the shape of the lowest mode of vibration, calculated using COMSOL.

The devices are not packaged in a vacuum tight enclosure: they interact with the surrounding residual gas. At the edges, the open area between the support beams and the plate is sufficiently large for gas molecules to enter or leave the gap between plate and substrate. To measure the pressure dependency of the devices, we mount them in a vacuum chamber with a base pressure less than 1×10^{-5} mbar. With a leak valve we introduce N_2 gas to achieve the desired pressure in the 1 to 10 mbar range. The pressure is measured with an MKS Baratron 627B capacitance manometer with an accuracy of 0.12%.

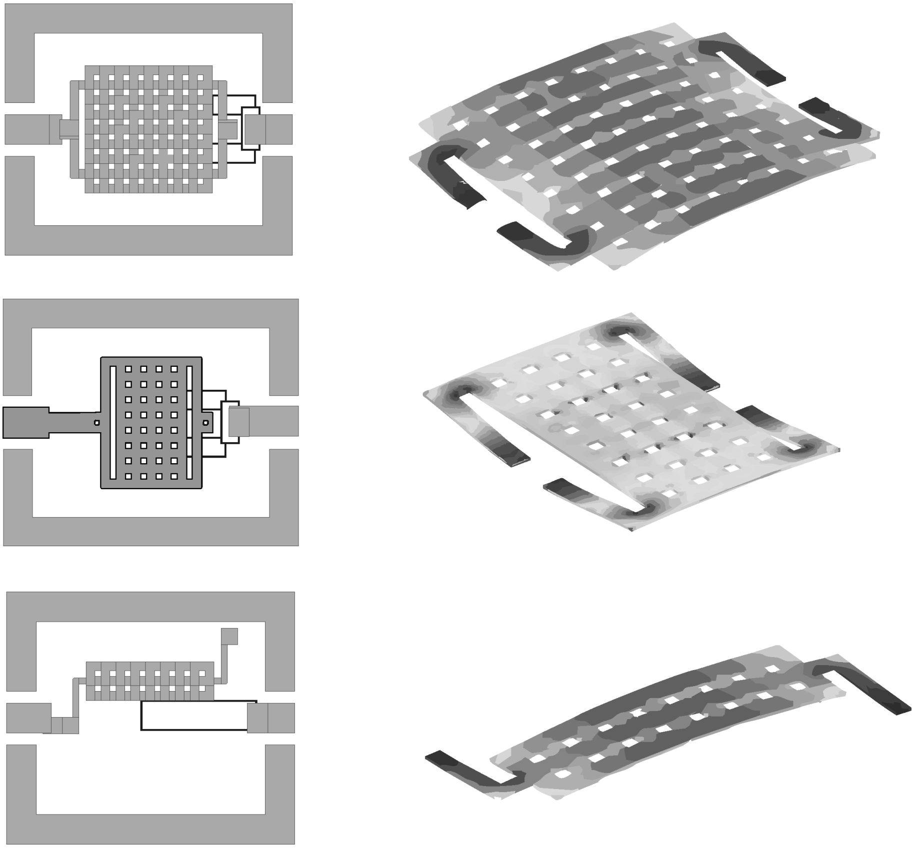

Figure 3: Design (left) and mode shape (right) of the MEMS resonators. Top to bottom: 8×8, 8×4 and 8×2 resonators.

Table 1: Characteristic dimensions of the three MEMS devices, together with the resonance frequency $\omega_{0,\mathrm{mat}}$, spring constant k_{mat} and mode shape factor γ as calculated from a finite element simulation using COMSOL. The calculation of the spring constant uses $U_{\mathrm{strain}}(t) = \frac{1}{2}k_{\mathrm{mat}}\, z_{\mathrm{max}}(t)^2$ with $z_{\mathrm{max}}(t)$ the maximum value of the microstructure's deflection.

Device	8×8	8×4	8×2
Plate area $A = L \times H$ (μm^2)	430×430	430×230	430×130
Unit cell $h \times h$ (μm^2)	50×50	50×50	50×50
Etch holes $l \times l$ (μm^2)	18×18	18×18	18×18
Left/bottom edge width (μm)	30	30	30
Spring constant k_{mat} (N/m)	81	75	33
Mode shape factor $\gamma = z_{\mathrm{max}}/\langle z\rangle$	1.53	1.25	1.37
Frequency $\omega_{0,\mathrm{mat}}/2\pi$ (kHz)	37	45	36

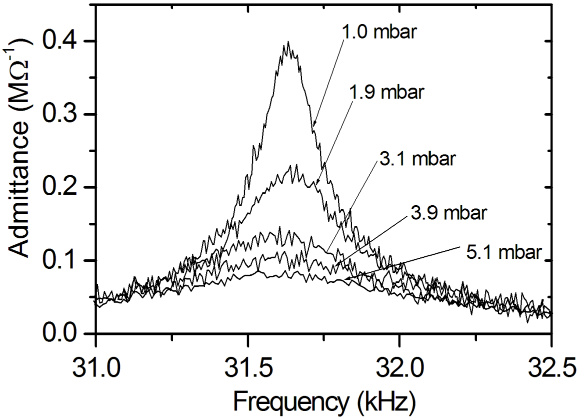

Figure 4: Typical experimental results of the resonances for the investigated MEMS resonators

The electrical readout of the amplitude of the oscillating plate is straightforward. The aluminium plate and a thin metal layer deposited on the substrate form a variable capacitor. Plate motion was detected via capacitance changes measured using an HP4294 impedance analyzer. At resonance, the plate amplitude rises and more mechanical energy is dissipated in the ambient gas. Since this dissipated energy must be supplied by the analyzer, a peak is seen in the magnitude of the admittance. We measure both the frequency response of the device to determine the quality factor as well as the ohmic dissipation on resonance. Both methods are in good agreement and result in a measure of the damping coefficient b. Only the '8×8' device results in 30% larger values of b with the latter method. However, the large dependency of the damping $b \propto d^{-4}$ on the gap width d suggests that the sacrificial etch for the '8×8' device perhaps is incomplete, with a 7.5% smaller value of d as result. As yet we have no definitive explanation for the observed discrepancy.

Typical experimental results are shown in Fig. 4. For five different values of the pressure in the vacuum chamber, ranging from 1.0 to 5.1 mbar, the resonance signal of the 8×8 device is shown as a function of the generator frequency. We clearly see the decrease of the quality factor with increasing pressure. We also observe that the shift of the resonance frequency is very small and nearly drowns in the errors of the measurement. We estimate an upper limit on the order of 20 Hz/mbar. We have to compare this result with the prediction of Eq. 9, with a maximum frequency shift for $\omega\tau \gg 1$ given by

$$\frac{1}{\omega}\frac{\mathrm{d}\omega}{\mathrm{d}p} = \frac{1}{2k}\frac{\mathrm{d}k_{\mathrm{squeeze}}}{\mathrm{d}p} = \frac{1}{2k}\frac{A}{d}\,. \tag{12}$$

For the 8×8 device we find a predicted maximum frequency shift of 10 kHz/mbar due to squeeze forces, more than two orders of magnitude larger than observed experimentally. This leads to us to the conclusion that our devices are in the regime where $\omega\tau < 0.1$.

By determining the quality factor Q of the resonance peak, we can calculate the damping coefficient of the resonator, using the relation

$$b = \gamma\, k/(\omega_0\, Q)\,. \tag{13}$$

Because the frequency shift due to the squeeze film force is negligible we use $k = k_{\mathrm{mat}}$ to calculate the damping coefficient b. The so-called mode shape factor $\gamma = z_{\mathrm{max}}/\langle z\rangle$ takes into account the different definition of the spring constant k_{mat} in the COMSOL simulation (related to the maximum value z_{max} of the plate deflection) and the definition in section 3 where effectively the position-averaged value of the amplitude is considered. This factor is derived from the actual shape of the oscillating plate as calculated in COMSOL. Numerical values are listed in Tab. 1.

In Fig. 5 we show the experimental results for the damping b as a function of the N_2 pressure in the test chamber at ambient temperature $T = 22$ °C. The observed

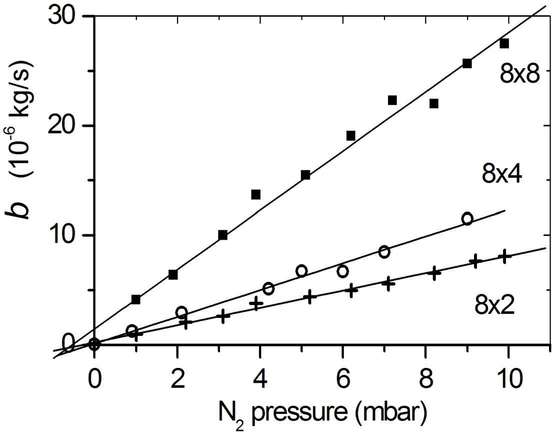

Figure 5: Pressure dependency of the measured damping coefficients for the three different MEMS resonators 8×8, 8×4 and 8×2.

Table 2: Experimental results for the damping of the MEMS devices. Using the nominal value of gap width d a value for diffusion time τ is fit from Eq. (14).

Device	Frequency $\omega_0/2\pi$ (kHz)	$\mathrm{d}b_{\text{squeeze}}/\mathrm{d}p$ (10^{-6} kg/s mbar)	Diffusion time τ (µs)	$\omega_0\tau$
8×8	31.6	2.71	0.438	0.088
8×4	38.7	1.22	0.373	0.091
8×2	31.2	0.79	0.425	0.083

damping constants turn out to be at least two orders of magnitude larger than the damping at zero pressure. Damping is thus squeeze-force dominated and the experimental values are not corrected by for the material damping b_{mat}. A least-squares straight-line fit is used to determine the pressure dependency of b_{squeeze}. For the 8×4 and the 8×2 devices there is no offset at $p = 0$, in contrast with the 8×8 device where we observe a small offset. We have no explanation for this effect. For all devices we have used the slope as the measure for $\mathrm{d}b_{\mathrm{squeeze}}/\mathrm{d}p$. Because we know that $\omega\tau \ll 1$, Eq. 8 simplifies to

$$b_{\mathrm{squeeze}} = p\,A\,\tau/d. \tag{14}$$

The experimental results are given in Tab. 2. We observe that the measured frequency is always $\sim$ 10 % less than the value calculated with COMSOL (Tab. 1). Using Eq. 14 we have also calculated the values for τ and $\omega\tau$, using the experimental value of ω for the latter. A counter intuitive result is that the random walk diffusion time τ is nearly independent of the area of the resonator plate of the device. Clearly, the etch holes in the plate play a very important role in equalizing the gas density in the gap volume. The values of $\omega\tau$ in the range of 0.08 to 0.09 are in agreement with our earlier analysis of the absence of a significant shift of resonance frequency with increasing pressure.

The next step is to investigate the dependency of τ on the plate area A, the gap width d and the properties of the gas molecules such as the average velocity $\langle v \rangle$. This confrontation of experiment and theory can help us to gain insight in the model. Comparing absolute values of parameters is an excellent test for theory. This test will help us to validate a model that can be reliably used to design MEMS resonators on first principles.

5 Diffusion time: analytical model

For the calculation of the diffusion time τ we consider the random walk of a molecule in a MEMS cavity as shown in Fig. 1. The model used has been derived for Brownian motion of small particles in a gas with Maxwell-Boltzmann statistics. The average value of the squared distance $\langle r^2 \rangle$ traveled by the molecule is then related to the square of the average unit step $\langle r_1 \rangle^2$ by

$$\langle r^2 \rangle = N \langle r_1 \rangle^2 , \tag{15}$$

with N the number of wall collisions. Here the distance r concerns the length of any straight line path, starting at any point within the plate area and ending at any point on the plate edge. For a rectangular plate, the average value of this squared distance equals

$$\langle r^2 \rangle = A/\pi \tag{16}$$

as derived from a simple geometrical calculation. The average value of the unit step size equals

$$\langle r_1 \rangle = \pi d/2, \tag{17}$$

which is obtained by averaging $r_1 = d \tan\theta$ over the flux impinging on the wall using Maxwell-Boltzmann statistics (appendix A). The same approach results in

$$\langle \tau_1 \rangle = 2d/\langle v \rangle\,, \tag{18}$$

with $\langle v \rangle = \sqrt{8k_\mathrm{B}T/(\pi m)}$ the average velocity of the gas molecules. Combining these results gives

$$N = (4/\pi^3)\,(A/d^2)\,, \tag{19}$$

$$\tau = N\langle \tau_1 \rangle = \frac{8}{\pi^3}\,\frac{A}{d\langle v \rangle}\,. \tag{20}$$

This result holds for a solid resonator plate *without* any etch holes. In our case, however, the resonator plates are perforated to facilitate the wet etch during processing (Tab. 1). These etch holes provide an extra escape probability for molecules in the gap volume, thus reducing the diffusion time τ drastically. The worst case we can imagine is that molecules only interact with a single unit cell before escaping through an etch hole. Inserting the unit cell dimensions of $A_\mathrm{cell} = h \times h = 50 \times 50\ \mu\mathrm{m}^2$ into Eq. 20 we find $\tau_\mathrm{cell} = 0.456\ \mu\mathrm{s}$. This is the correct order of magnitude as compared to the experimental results in Tab. 2. Also, this rather crude approach results in a diffusion time τ that does not depend on the size of the device, again as observed in our experiments.

Using this insight, we will now investigate if we can refine this rather crude model by looking into the escape probability through the etch holes in more detail. We consider a single unit cell surrounded by four etch holes. We draw an escape circle with radius $h\sqrt{2}$ that approximately coincides with the diagonal of the four etch holes. The unit cell escape probability Γ is defined as the fraction of the circumference that coincides with the etch holes, as given by

$$\Gamma = (4/\pi)\,(l/h), \tag{21}$$

with l the etch hole size and h the unit cell size. Understanding that a diffusing molecule will not escape until a certain number of unit cells s have been traversed, we write the effective value τ_{eff} of the diffusion time as a power series in complementary probability $(1 - \Gamma)$, resulting in

$$\tau_{\text{eff}} = \Gamma\tau_{\text{cell}} \left[1 + 2(1-\Gamma) + 3(1-\Gamma)^2 + \cdots + s(1-\Gamma)^{s-1}\right] . \qquad (22)$$

In the extreme case of an infinitely large device, this series yields $\tau_{\text{eff}} = \tau_{\text{cell}}/\Gamma$ with τ_{cell} the diffusion time corresponding to a single unit cell. The series is correctly normalized by

$$\Gamma_s = \Gamma + \Gamma(1-\Gamma) + \Gamma(1-\Gamma)^2 + \cdots + \Gamma(1-\Gamma)^s \qquad (23)$$

with $\Gamma_\infty = 1$. When Γ is large, a few terms of Eqs. (22) and (23) already suffice, as indicated by a partial escape probability $\Gamma_s \simeq 1$. Depending on the size of the device we find a range $\tau_{\text{cell}} < \tau_{\text{eff}} < \tau_{\text{cell}}/\Gamma$ for the effective value of the diffusion time. The lower boundary is for a device with the dimensions of a unit cell.

For our experiments, with $\Gamma = 0.46$, we find $\tau_{\text{cell}} < \tau_{\text{eff}} < 2.2\,\tau_{\text{cell}}$ corresponding to $0.456\ \mu\text{s} < \tau_{\text{eff}} < 1.00\ \mu\text{s}$. Comparison to the experimental results for τ in Tab. 2 shows that the trend of this refined model does not agree with experiment. We conclude that the analytical approach does result in insight in the role of etch holes, but does not result in a quantitative agreement with experiments. To resolve this matter we will switch to full Monte Carlo simulations, where the random walk of each molecule is followed until it escapes through an etch hole or crosses over the boundary of the plate.

6 Monte Carlo simulation of random walk

6.1 Method

Free molecular flow is ideally suited to investigate using a Monte Carlo simulation of individual trajectories of the molecules. In this simulation we can readily accommodate all the details of the plate geometry including etch holes. By following each trajectory i until it hits an etch hole in the plate or crosses the edges of the plate, we find the distribution function of the number N_i of wall collisions and the time τ_i it takes to escape. The average values $\langle N_i \rangle = N$ and $\langle \tau_i \rangle = \tau$ are then equal to the number of collisions N and the random walk diffusion time τ, as calculated in section 5 with an analytical approximation.

The numerical routine is rather simple. Two random numbers are used to determine the initial position on the plate. If this position coincides with an etch hole, we discard this initial state and repeat the routine. Boltzmann statistics determine the velocity vector of the departing molecule. Simple procedures are available for choosing random values of the cartesian velocity components v_x and v_y, because Boltzmann statistics are governed by a Normal distribution for all components, with variance $\sigma^2 = (\pi/8)\langle v\rangle^2$. The displacement vector $\vec{r}_1$ after crossing the gap is given by $(v_x, v_y)\,\Delta\tau$ with $\Delta\tau = (d/v_z)$. For v_z we have to choose random values from a flux-weighted distribution with a pre-exponential factor v_z, usually referred to as a Rayleigh distribution (appendix A). Again, a simple transformation allows us an easy pick of a random value.

All trajectories are initialized on the plate. After each collision we assign new, random values to the velocity vector (v_x, v_y, v_z) of the molecule and check if the trajectory has crossed the edges of the plate; every second collision, we also check if the point of impact coincides with an etch hole: if not, we continue the current trajectory. If so, we store the value of N_i and τ_i and initialize a new trajectory $(i+1)$. By desire, we can also store other properties of the trajectory to investigate details of the process such as average step size $\langle r_1\rangle = \langle \sqrt{\Delta x^2 + \Delta y^2}\rangle$ to compare to the predictions of our analytical model in section 5. The procedure is programmed in C++ and embedded in Mathematica for easy handling of the output. This procedure is repeated to improve statistical accuracy in these parameters. Typical calculation time for a sample size $n = 10^5$ trajectories with $N = 35$ collisions is 400 s. We have checked that the variance in τ follows the expected behavior according to $\sigma_\tau^2 = \tau^2/n$.

6.2 Solid plate

To obtain insight in the process of random walk in the gap, we have first investigated the case of a solid plate *without* etch holes. Objective is to test the accuracy of the Brownian motion model of section 5. Assuming a square plate geometry, with dimensions corresponding to the '8×8' device, we find $N_{MC} = 429$ which should be compared to $N = 2650$ from Eq. (19). To our surprise, we observe a major discrepancy between these two approaches. By varying the area A of the square plate we find the empirical relation

$$N_{MC} = 429 \left(\frac{A}{A_{8\times 8}}\right)^{0.84}, \qquad (24)$$

that shows even a different A-dependency than the linear relationship of Eq. (19). This deserves a close inspection before we proceed to simulation of the actual devices.

In Fig. 6 we have plotted twelve trajectories of molecules in the gap of a solid square plate with the dimensions of the '8×8' device. Most remarkable are the comparatively long jumps r_1 that regularly occur during the random walk. It is obvious

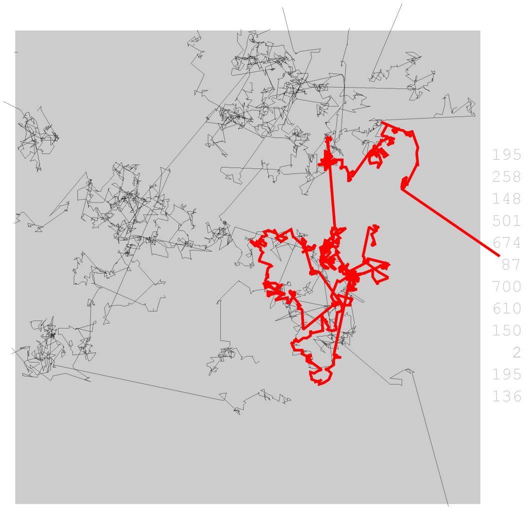

Figure 6: Simulated random walk of 12 particles in the ’8×8’-type resonator gap for a solid plate. The particle trajectories often contain ’long’ jumps contrary to the picture of fig. 1.

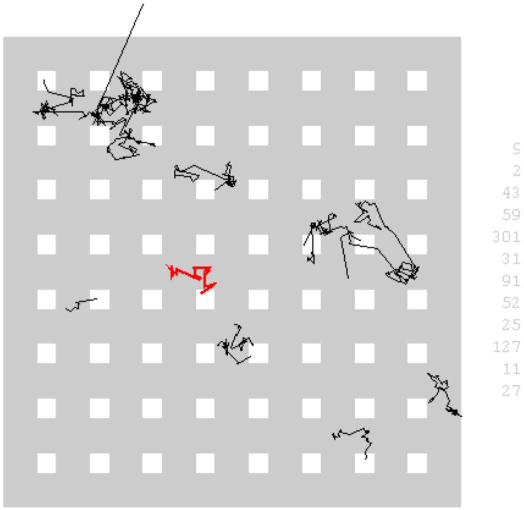

Figure 7: Simulated random walk of 12 molecules in the gap of the actual ’8×8’ resonator with etch holes, showing the large effect of etch holes on the trajectories.

Table 3: Monte Carlo results for the random walk diffusion time τ and the collision number N for the MEMS devices in Tab. 1. The number in parentheses indicates the error in the last digit. For comparison, the experimental results from Tab. 2 are listed in the column "measured".

Device	Collision number N	Diffusion time τ (µs) simulated	Diffusion time τ (µs) measured
8×8	34.1	0.436(2)	0.438
8×4	31.1	0.398(2)	0.373
8×2	28.8	0.368(2)	0.425

that these long jumps have a strong influence on the collision number N before escaping: this fully explains the discrepancies between the results of the Brownian motion model with the Monte Carlo results. This becomes even more clear when we investigate the normalized distribution function $P(r_1)\mathrm{d}r_1$ for the single step length r_1, as derived in appendix B and given by

$$P(r_1)\mathrm{d}r_1 = \frac{2d^2\, r_1}{(r_1^2 + d^2)^2}\,\mathrm{d}r_1. \tag{25}$$

For large values of r_1 the distribution function decays as $P(r_1)\mathrm{d}r_1 \sim (r_1/d)^{-3}$, i.e. a long-tail distribution that does predict an expectation value $\langle r_1 \rangle = \pi\, d/2$ but has a variance that diverges. This is the root cause that we cannot apply the available models for Brownian motion to our random walk process. In Brownian motion, momentum kicks and thus the single step length r_1 are governed by a Boltzmann distribution that decays as $\sim e^{-r_1^2}$, eliminating long jumps as observed here.

6.3 Plate with etch holes

We can now apply the Monte Carlo simulation method to calculate the random walk diffusion time τ of the actual devices as given in Tab. 1, including the etch holes. In Fig. 7 we show the trajectories of 12 molecules moving in the gap of the '8×8' device. The trajectories only extend over one to a few unit cells. Clearly, the etch holes provide the opportunity to escape for a majority of the molecules. This is reflected in the values for N and thus τ, as given in Tab. 3. For all devices we observe a very good agreement within 10% of the Monte Carlo predictions for τ with the experimental results in Tab. 2.

The calculated collision number N decreases when going from the '8×8' device to the '8×2' device. To distinguish the role of the decreasing plate area A and the changing plate geometry, with length-to-width ratios L/H ranging from 1:1 tot 4:1,

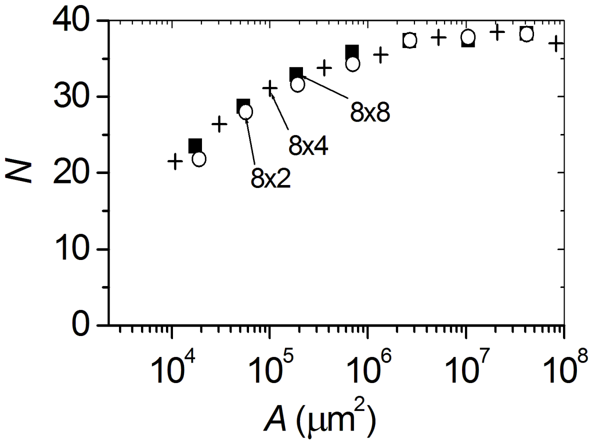

Figure 8: Monte Carlo simulation result of the number of random walk steps in the '8×8'-type resonator gap as a function of plate area. The '○', '+' and '■' symbols represent data points for a length-to-width ratio of 4:1, 2:1 and 1:1 respectively. The three labeled symbols indicate the number of random walk steps for the actual 8×8, 8×4 and 8×2 devices

we have simulated these cases separately. In Fig. 8 we have varied the area A while keeping L/H fixed. We observe that the influence of the area A on N is much larger than the length-to-width ratio. The pattern of etch holes is kept fixed at the design of the actual devices. As expected, with increasing area the collision number saturates to an asymptotic value $N_\infty = 38$ that only reflects the etch hole pattern.

This type of empirical dependency can easily be implemented in a design package for MEMS devices. In general, the process already prescribes the desired etch hole pattern for etching the sacrificial layer underneath the micro-structure. This wraps up the last input for designing tailor-made devices that operate on specification.

7 Discussion of Bao's model

Now that we established the validity of our model, we can put the good agreement of the damping on the microbeam resonator of Zook [11] with Bao's model in perspective. For a comparison of Bao's results to our model, we have rewritten the expression for the squeeze film quality factor given by Eq. 23 of his paper [10]. The result is

$$Q = \sqrt{2\pi}^3 \, \omega_0 \, \frac{M}{A} \, \frac{d}{S} \, \sqrt{\pi/8} \, \langle v \rangle \, \frac{1}{p}, \tag{26}$$

where plate mass is defined by $M = \rho A t$ and ρ, t and S (in the notation used by Bao) represent density of plate material, plate thickness and circumference of plate area A, respectively. Using

$$\beta = \frac{\mathrm{d}}{\mathrm{d}p} b = \frac{\mathrm{d}}{\mathrm{d}p}\left(\frac{M\,\omega_0}{Q}\right), \tag{27}$$

the expression for β_{Bao} takes the shape

$$\beta_{\mathrm{Bao}} = \frac{A}{d}\,\frac{S}{\pi^2\,\langle v\rangle} = \frac{A}{d}\,\frac{2\,(L+H)}{\pi^2\,\langle v\rangle}, \tag{28}$$

Our result reads

$$\beta_{\mathrm{Suijlen}} = \frac{A}{d}\,\frac{\tau}{1 + (\omega_0\,\tau)^2} \tag{29}$$

where the diffusion time τ is determined by random walk Monte Carlo simulations for a plate with area $A = L \times H$, with L and H the plate length and width, respectively. The diffusion time τ scales as

$$\tau \propto (d\,\langle v\rangle)^{-1} \tag{30}$$

as follows from the collision number $N \propto d^{-2}$ (Eq. (19)) and the gap crossing time $\langle\tau_1\rangle \propto d/\langle v\rangle$ (Eq. (18)). The dependence on the plate geometry in the Monte Carlo simulations can be approximated by

$$\tau \propto [\min(L, H)]^{1.6}. \tag{31}$$

The latter can be understood readily when realizing that the smallest dimension of the plate will determine the escape probability for the molecules in the gap volume. The 1.6 power dependence is due to the non-Gaussian distribution function for the single step displacement in Eq. (25).

By combining the results of Eqs. (28), (29), (30) and (31), we find

$$\frac{\beta_{\mathrm{Suijlen}}}{\beta_{\mathrm{Bao}}} \equiv \eta \propto \frac{[\min(L, H)]^{1.6}}{2(L+H)\,d}, \tag{32}$$

depending only on the geometry of the device.

In Tab. 4 we compare both models for the microbeam of Zook and three plate oscillators with dimensions corresponding to the devices in section 4, however, *without* the etch holes. We see a fair agreement between both models for Zook's device and rapidly increasing factors of disagreement for the larger devices. This is no surprise given the very different scaling rules for the dimensions of the devices as discussed above.

Table 4: Comparison of β values, calculated with the models of Bao (Eq. (28)) and Suijlen (Eq. (29)). Here the η values are defined by the ratio $\beta_{\text{Suijlen}}/\beta_{\text{Bao}}$ (Eq. (32)). The size of the test samples corresponds to the 8×2, 8×4 and 8×8 devices specified in section 4. However, the models have been applied to a plate *without* etch holes.

Test sample (no etch holes)	$L \times H$ (µm^2)	$\omega_0/(2\pi)$ (kHz)	d (µm)	β_{Suijlen} (10^{-6} kg/s mbar)	β_{Bao} (10^{-6} kg/s mbar)	η
8×2 plate	430×130	31.2	3.0	2.43	0.46	5.3
8×4 plate	430×230	38.7	3.0	6.47	0.95	6.8
8×8 plate	430×430	31.6	3.0	15.61	2.31	6.8
Zook beam	200×40	550	1.1	0.101	0.075	1.3

8 Concluding remarks

We have introduced an analytical model for squeeze film damping of an oscillating plate in the regime of free molecular flow. This model is based on the increase in density due to the amplitude of the plate movement. A phase shift due to the counteracting random walk diffusion in the gap which tries to equalize this increase, results in an extra damping that agrees well with accurate experimental results. The calculation of the random walk diffusion time is based on the well known properties of free molecular flow and the interaction of gas molecules with a surface at conditions representative for MEMS operation. Full thermal accommodation is the rule; specular reflection is the exception in all practical cases. Through the model we have gained insight which allows us to design tailor-made devices that will operate on specification.

A Molecular impingement rate

In kinetic theory molecular transport is solely determined by the velocities and collisions of the individual molecules. Because these velocities have random values as a consequence of the collisions, only the velocity-averaged value according to a certain probability distribution can be regarded. This probability distribution is known as the normalized velocity distribution P_{MB} of Maxwell-Boltzmann. In spherical coordinates it is formulated as

$$\begin{aligned}
P_{\mathrm{MB}}(v,\theta,\phi)\,\mathrm{d}v\mathrm{d}\theta\mathrm{d}\phi &= P_V(v)\mathrm{d}v\,P_\Theta(\theta)\mathrm{d}\theta\,P_\Phi(\phi)\mathrm{d}\phi,\\
P_V(v)\mathrm{d}v &= \frac{4\,v^2}{\sqrt{\pi}\,\alpha^3}\,e^{-(v/\alpha)^2}\,\mathrm{d}v,\\
P_\Theta(\theta)\mathrm{d}\theta &= \frac{1}{2}\,\sin\theta\,\mathrm{d}\theta,\\
P_\Phi(\phi)\mathrm{d}\phi &= \frac{1}{2\pi}\,\mathrm{d}\phi,
\end{aligned} \tag{33}$$

and gives the fraction of the gas molecules having speeds between v and $v + \mathrm{d}v$, traveling in a solid angle element between (θ, ϕ) and $(\theta + \mathrm{d}\theta, \phi + \mathrm{d}\phi)$. The three individual probability distributions for v, θ and ϕ are normalized in the domains $v \in [0, \infty)$, $\theta \in [0, \pi)$ and $\phi \in [0, 2\pi)$. The characteristic speed α is defined by

$$\alpha = \sqrt{2k_{\mathrm{B}}\,T/m} \tag{34}$$

with k_{B} Boltzmann's constant, T the temperature and m the molecular mass.

By means of this velocity distribution we can make good theoretical predictions for all kinds of transport properties in a gas starting from single molecule trajectories. For example, the molecular impingement rate Ψ_{total} $[\mathrm{m}^{-2}\,\mathrm{s}^{-1}]$ can be formulated as the expectation value of the velocity distribution for $n\,v_\perp$ with n the molecular number density and $v_\perp$ the velocity component perpendicular to the surface at which the molecules impinge. For a surface that lies aligned with the xy-plane so that $v_\perp = v\,\cos\theta$, the calculation of the impingement rate yields

$$\begin{aligned}
\Psi_{\mathrm{total}} &= \int_0^{2\pi}\int_0^{\frac{\pi}{2}}\int_0^{\infty} n\,v\,\cos\theta P_{\mathrm{MB}}(v,\theta,\phi)\,\mathrm{d}v\mathrm{d}\theta\mathrm{d}\phi\\
&= \int_0^{2\pi}\int_0^{\frac{\pi}{2}}\int_0^{\infty} \Psi(v,\theta,\phi)\,\mathrm{d}v\mathrm{d}\theta\mathrm{d}\phi\\
&= n\int_0^{2\pi}\frac{1}{2\pi}\,\mathrm{d}\phi\int_0^{\frac{\pi}{2}}\frac{1}{2}\,\sin\theta\,\cos\theta\,\mathrm{d}\theta\int_0^{\infty}\frac{4\,v^3}{\sqrt{\pi}\,\alpha^3}\,e^{-(v/\alpha)^2}\,\mathrm{d}v\\
&= \frac{1}{4}n\,\langle v\rangle,
\end{aligned} \tag{35}$$

a well-known expression which can be found in any basic textbook.

Also the pressure on the wall can be calculated as the expectation value of Eq. (33) for $(n\,v_\perp)\cdot(2m\,\Delta v_\perp)$. The first term describes the contributing incident flux and the second term the momentum transferred on collision with the wall. The known result reads $p = \frac{1}{3} n\, m\, \langle v^2\rangle$ likewise expressed as $p = n\, k_\mathrm{B}\, T$, being Boyle's law.

Important in this respect of molecules interacting with a wall is the flux-weighted speed distribution P_wall which is in terms of P_MB defined as:

$$P_\mathrm{wall} = \frac{n\, v_\perp}{\Psi_\mathrm{total}}\, P_\mathrm{MB} \tag{36}$$

Again supposing the wall surface to be aligned with the xy-plane and using the current (v, θ, ϕ)-coordinates, this distribution is written as

$$\begin{aligned}
P_\mathrm{wall}\, \mathrm{d}v\mathrm{d}\theta\mathrm{d}\phi &= P_V^\mathrm{wall}(v)\mathrm{d}v\, P_\Theta^\mathrm{wall}(\theta)\mathrm{d}\theta\, P_\Phi^\mathrm{wall}(\phi)\mathrm{d}\phi,\\
P_V^\mathrm{wall}(v)\mathrm{d}v &= 2\frac{v^3}{\alpha^4}\, e^{-(v/\alpha)^2}\, \mathrm{d}v,\\
P_\Theta^\mathrm{wall}(\theta)\mathrm{d}\theta &= 2\sin\theta\, \cos\theta\, \mathrm{d}\theta,\\
P_\Phi^\mathrm{wall}(\phi)\mathrm{d}\phi &= \frac{1}{2\pi}\, \mathrm{d}\phi,
\end{aligned} \tag{37}$$

The two individual probability distributions $P_V^\mathrm{wall}(v)\mathrm{d}v$ for v and $P_\Phi^\mathrm{wall}(\phi)\mathrm{d}\phi$ for ϕ are normalized here in the same domains as their equivalents in P_MB. However for $P_\Theta^\mathrm{wall}(\theta)\mathrm{d}\theta$ the domain is restricted to $\theta \in [0, \pi/2)$. A comparison of the individual probability distributions to their equivalents in P_MB leads to the next relations which can be helpful:

$$P_V^\mathrm{wall}(v) = \frac{\sqrt{\pi}}{2}\, \frac{v}{\alpha}\, P_V(v) \tag{38}$$

$$P_\Theta^\mathrm{wall}(\theta) = 4\cos\theta\, P_\Theta(\theta) \tag{39}$$

$$P_\Phi^\mathrm{wall}(\phi) = P_\Phi(\phi) \tag{40}$$

If the application features planar symmetry, calculations become simpler with cartesian coordinates v_x, v_y and v_z. In that case the flux-weighted speed distribution is formulated as

$$\begin{aligned}
P_\mathrm{wall}\, \mathrm{d}v_x\mathrm{d}v_y\mathrm{d}v_z &= P_{vx}^\mathrm{wall}(v_x)\mathrm{d}v_x\, P_{vy}^\mathrm{wall}(v_y)\mathrm{d}v_y\, P_{vz}^\mathrm{wall}(v_z)\mathrm{d}v_z,\\
P_{vx}^\mathrm{wall}(v_x)\mathrm{d}v_x &= (\alpha\, \sqrt{\pi})^{-1}\, e^{-(v_x/\alpha)^2}\, \mathrm{d}v_x,\\
P_{vy}^\mathrm{wall}(v_y)\mathrm{d}v_y &= (\alpha\, \sqrt{\pi})^{-1}\, e^{-(v_y/\alpha)^2}\, \mathrm{d}v_y,\\
P_{vz}^\mathrm{wall}(v_z)\mathrm{d}v_z &= 2\frac{v_z}{\alpha^2}\, e^{-(v_z/\alpha)^2}\, \mathrm{d}v_z.
\end{aligned} \tag{41}$$

Here the distributions for v_x and v_y represent identical *Normal distributions* with variance $\sigma^2 = \alpha^2/2 = (\pi/8)\langle v\rangle^2$ and the domains of v_x and v_y both span the whole real line $(-\infty, \infty)$. The distribution for v_z represents a *Rayleigh distribution* with parameter $\alpha/\sqrt{2}$ where the v_z-domain contains only the half real line $[0, \infty)$.

B Distribution of step length r_1

With the establishment of the flux-weighted velocity distribution of Eq. (37), the probability distribution $P(r_1)\mathrm{d}r_1$ of the random-walk step-length r_1 is easily derived using the relation

$$r_1 = d\,\tan\theta. \tag{42}$$

The random variable θ in this situation has the marginal distribution $P_\Theta^{\text{wall}}(\theta)\,\mathrm{d}\theta$. Recalling basic probability theory, the distribution $P_Y\,\mathrm{d}y$ of any other variable y, depending on θ according to an invertible and differentiable transformation $f(\theta)$, will satisfy

$$P_Y(y)\,\mathrm{d}y = P_\Theta^{\text{wall}}(f^{-1}(y))\,\frac{\mathrm{d}}{\mathrm{d}y}f^{-1}(y)\,\mathrm{d}y, \tag{43}$$

where f^{-1} represents the inverse transformation.

Identifying $\arctan(r_1/d)$ as the $f^{-1}(y)$ in our case from Eq. (42), the distribution function $P(r_1)\mathrm{d}r_1$ of step length r_1 is found to be

$$\begin{aligned} P(r_1)\,\mathrm{d}r_1 &= P_\Theta^{\text{wall}}(\arctan(r_1/d))\,\frac{\mathrm{d}}{\mathrm{d}r_1}\arctan(r_1/d)\,\mathrm{d}r_1 \\ &= 2\frac{r_1/d}{1+(r_1/d)^2}\,\frac{1/d}{1+(r_1/d)^2}\,\mathrm{d}r_1 \\ &= \frac{2d^2\,r_1}{(r_1^2+d^2)^2}\,\mathrm{d}r_1 \end{aligned} \tag{44}$$

References

[1] J.J. Blech, J. Lubr. Technol. **105** (1983) 615-20.

[2] T. Veijola, H. Kuisma, J. Lahdenpera, and T. Ryhanen, Sens. Actuators A **48** (1995) 239-48.

[3] M. Bao, H. Yang, Sens. Actuators A **136** (2007) 3-27.

[4] G. Li and H. Hughes, Proc. SPIE **4176** (2000) 30-46.

[5] W. Newell, Science **161** (1968) 1320-6.

[6] Y. Kawamura, K. Sato, T. Terasawa, and S. Tanaka, Proc. Transducers'87 (1987) 283-6.

[7] Z. Kadar, W. Kindt, A. Bossche, and J. Mollinger, Proc. Transducers'95 (1995) 29-32.

[8] B. Li, H. Wu, C. Zhu, and J. Liu, Sens. Actuators A **77** (1999) 191-4.

[9] H. Sumali, J. Micromech. Microeng. **17** (2007) 2231-2240.

[10] M. Bao, H. Yang, H. Yin, Y. Sun, J. Micromech. Microeng. **12** (2002) 341-346.

[11] J. Zook, D. Burns, H. Guckel, J. Sniegowski, R. Engelstad, Z. Feng, Sens. Actuators A **35** (1992) 51-59.

[12] M.J. Martin, B.H. Houston, J.W. Baldwin, M.K. Zalalutdinov, J. Microelectromech. Syst. **17** (2), 2008, 503-511.

[13] R.G. Christian, Vacuum **16** (4), 1966, 175-178.

Chapter 3

Model-based design of MEMS resonant pressure sensors

Abstract

Micro-mechanical resonators are known to require vacuum conditions for proper operation, involving free molecular flow of the residual gas in the squeeze-film box under the resonator. This flow is ideally suited to be described by investigating trajectories of the individual molecules using a Monte Carlo approach. We developed a simple analytical model for describing squeeze-film forces on MEMS resonators, with the average escape time τ of a molecule from the squeeze-film box as the only device-based free parameter. The value of τ is calculated using a Test Particle Monte Carlo Method (TPMC). Geometrical details of the MEMS resonator including etch holes and slits can be readily accommodated in TPMC routines, in contrast to the rather laborious implementation of these details in case of a continuum description. Using the model, three different MEMS resonators have been designed and fabricated for an application as pressure sensors. Each device can be read-out by monitoring either the increase in damping or the shift in resonant frequency. The experimentally observed behavior of the devices in both read-out modes is fully consistent with the model, showing agreement to within 10%.

1 Introduction

The advent of microfabrication technologies in the last couple of decades has led to an exciting and revolutionary field called micro-electro-mechanical systems (MEMS) technology. MEMS applications are found in all kinds of sensors and actuators contained by modern cars and everyday digital electronics. Their development requires extensive knowledge on the behavior of the mechanical element in the system. Except structural mechanical properties, influences from outside must be considered to describe the element's motion correctly. In particular the role of gas damping on the element is important. For a resonant sensor which needs high resolution, damping should be minimized to enhance quality factor. With regard to the outright narrow gaps between element and electrodes featuring typical designs, a single phenomenon appears to be dominant: *squeeze-film damping*.

In MEMS resonators the narrowly separated surfaces of movable elements can confine the gas almost completely in the gap while compressing the film in an oscillation cycle, even though the structure is open at the ends. This represents one extreme of the squeeze-film effect: the compression of a gas between approaching parallel surfaces with a gap much smaller than their dimensions. Since the gas cannot escape, the dominant force is one of compression and this adds to the structure's stiffness, raising its resonance frequency. Only at low frequencies, as the gas is pushed out of and drawn back into the gap, the gas-resonator interaction obtains a pure drag character.

Because the gases trapped in the cavities of MEMS often are so rarefied that the molecular mean free path exceeds the gap dimensions by at least an order of magnitude, the squeeze-film flow becomes 'free molecular'. Squeeze-film damping in this regime is an interesting problem that has been attracting a lot of attention in the last decade. Its modeling has long been retained to the field of continuum flow, using an effective viscosity μ_{eff} that takes into account the rarefaction effects [1, 2, 3]. Although this approach can predict both damping and frequency shift of the resonator due to film flow, its application to complex geometrical structures in real-life technology – including etch holes, springs and stacked structures – is impossible without a highly specialized and tedious programming effort.

Here, a molecular approach to directly model the transport of individual molecules shows a great advantage. Because the molecules do not interact with each other, molecular trajectories in the system consist of randomly oriented straight line passages between structural boundaries. The (numerical) simulation of these trajectories can be carried out in a direct manner and easily be applied to large trajectory numbers for an accurate picture of gas flow. Currently this so called **Test Particle Monte Carlo** (TPMC) method has been developed to a powerful means in solving molecular flow in complex vacuum systems [4].

Early applications of molecular transport [5, 6, 7, 8, 9], however, assumed free space kinetics for squeeze-film damping modeling, ignoring with it the constrained trajectories that the molecules in the narrow resonator gaps are performing. Consequently, these models effectively give account of the kinetic damping contribution only, underestimating the experimental values for squeeze film damping largely [10, 11].

More recent applications [11, 12, 13, 14, 15] do consider the confined space of the resonator gaps and approximate reasonably well the experimental values of quality factor due to squeeze-film damping. One important aspect, however, is being ignored: the compressibility of the squeeze-film. A clue for this aspect is given by the phenomenon in resonators that resonance frequency increases with increasing ambient pressure (Fig. 1). Andrews et al. [16] have performed measurements on a device with such a pronounced containment of the gas in the squeeze-film box that this phenomenon starts playing a role at pressures where the film flow is still free molecular.

For this reason we developed a simple analytical model for squeeze-film damping in the regime of free molecular flow, which is able to predict the damping force component degrading the resonator's quality factor as well as the spring force component that raises the resonance frequency. We apply this model to measurements on three different MEMS resonators to show good agreement in the effect of squeeze-film damping on quality factor and resonance frequency. The only free parameter is the device-based average escape time τ of gas molecules from the squeeze-film box. Based on the model, we have designed and fabricated three MEMS resonators that

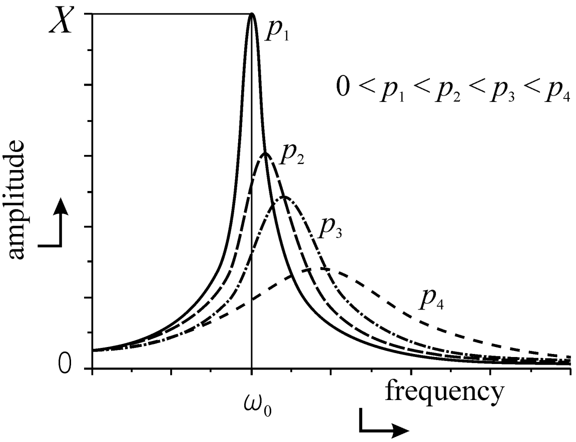

Figure 1: Resonance spectrum of a *squeeze-film* resonator at constant driving force F_0. With increasing pressure p the amplitude X at resonance decreases, the width of the resonance increases (both due to the increased damping), and the resonance frequency ω_0 shifts to higher frequencies.

can serve as pressure sensors. Pressure read-out can be done either by monitoring the increase in damping or the shift in operating frequency. The experimental results in both read-out modes are consistent with the model predictions, within an accuracy of typically 10%. This demonstrates the value of the model for designing new devices, avoiding trial and error loops to meet the specifications.

In section 2 we discuss the model in detail. The calculation of the escape time τ is discussed in section 3. Also we apply our model to predict the damping of one of the devices of Legtenberg et al. [17], which has also been used by Leung et al. [15] to validate their Monte Carlo approach for calculating the damping coefficient. In section 4 we present the devices that have been designed and fabricated, including the results obtained by simulation of the mechanical behavior with COMSOL Multiphysics. In section 5 the experimental results are shown, including a discussion of the analysis of the raw data on the resonance profiles. To represent the experimental results of all devices in a single diagram, we introduce a generalized two-dimensional plot in section 6 with scaled values of the pressure-dependency of both damping and frequency shift as major axes. Finally, in section 7, we present some concluding remarks on the lessons learned.

2 Squeeze-film damping in free molecular flow

The basics are rather simple: due to the oscillation of the resonator according to $z_0(x, y)\ \sin(\omega\, t)$, the number density n in the 'box' between resonator and the fixed substrate will vary proportional to $\sin(\omega\, t + \phi)$. The driving force for the variation of the density is the varying height of the gap

$$d(x, y; t) = d + z(x, y; t) = d + z_0(x, y)\ \sin(\omega\, t). \tag{1}$$

In a macroscopic picture, this change in height results in an increase in volume and thus a decrease in number density. In a microscopic picture, the change in height results in an increase in the round-trip time of the colliding molecules and thus in a decrease of the wall collision rate which indicates a decrease in number density. The phase difference ϕ in the response of the density n reflects the time lag in the free molecular flow equalizing the number density to its value n_0 outside the squeeze-film box. If we denote the response time for this process as τ, we can define two regimes in terms of the value of the non-dimensional characteristic parameter $\omega\,\tau$.

First, for $\omega\,\tau \gg 1$, the density will be nearly fully determined by the change in gap height and the influence of free molecular flow that equalizes the pressure is very small. As a result, the phase difference will be close to zero; $\phi \approx 0$. The increase in density is then nearly out of phase with the velocity of the resonator. The product of change in density and work done by the resonator on the gas then averages out to approximately zero over one period of oscillation. We then observe a small value of the damping; the major effect is on the effective force constant of the resonator which increases due to the 'air cushion'. This situation can be compared to a person trying to get the air out of an air mattress by jumping up and down on it. The bounce is perfect, but very little air escapes.

Second, for $\omega\,\tau \ll 1$, the change in number density will be rapidly equalized by the free molecular flow. For this reason, the effective variation of the density will be much less than predicted by the changes in volume or round-trip time between two collisions, whatever picture is preferred. The phase shift in the number density is given by $\phi \approx \pi/2$ and is in phase with the velocity of the resonator. Under these conditions, damping dominates and the increase in the effective force constant (or stiffness) of the resonator is rather small. Returning to our example of an air mattress, this situation corresponds to sitting down on it and letting the air flow out: no bounce, but a lot of air escapes!

2.1 Model assumptions

For industrial applications, we are interested in an efficient model that describes both damping and frequency shift for optimizing the design of MEMS devices. We do not aim at including all detail, but search for a trade-off between insight based on an analytical description, sufficient accuracy, flexibility in incorporating new geometries, and rapid numerical characterization in a design code. This implies that we will only include effects that are first-order in the amplitude of the oscillating plate; all higher-order terms will be discarded. This approach differs from most papers published in this field, where the emphasis is put on achieving ultimate accuracy by including all possible terms.

Because molecules in the squeeze-film box do not interact with each other, they move in and out of the box only via random crossings between facing boundaries of resonator and substrate. This transport occurs independent of local density differences inside the film. We characterize this transport by the ensemble-averaged escape time $\tau(x, y)$. For the correct process of averaging, Boltzmann statistics of the gas are taken into account. For all devices with a lateral dimension much larger than the gap height, the escape time $\tau(x, y)$ will hardly depend on the location (x, y) in the squeeze-film box. For devices with a large set of equally spaced etch holes, this will even be more pronounced. Therefore, we will use a spatially averaged value of the escape time, as given by

$$\tau = \iint_S \tau(x, y)\, \mathrm{d}x\mathrm{d}y \Big/ \iint_S \mathrm{d}x\mathrm{d}y\ , \tag{2}$$

with S referring to the lateral domain of the squeeze-film box in x- and y-coordinates. This assumption also implies that a density profile $n(x, y; t)$ will decay with a single time constant equal to the spatially averaged escape time τ, allowing us to use the spatially-averaged value $n(t)$ of the density:

$$n(t) = \iint_S n(x, y; t)\, \mathrm{d}x\mathrm{d}y \Big/ \iint_S \mathrm{d}x\mathrm{d}y\ . \tag{3}$$

The value of τ will depend on the geometrical details of the device, such as gap height, area, and etch holes in the plate. However, these assumptions imply that the mode shape $z(x, y; t)$ does not have any influence on the dynamics of the gas in the squeeze-film box. At a later stage, where we present the results for the calculation of τ, we will discuss the validity of these approximations.

For our model we choose the equilibrium values n_0 and T_0 of the surrounding gas outside the box as a reference for density and temperature, respectively. The increase $\Delta n(t) = n(t) - n_0$ in density of the gas in the squeeze-film box is the driving force for damping and the increase in the elastic force constant. We introduce the mode-averaged value $z_{c,0}$ of the amplitude

$$z_{0,c} = \iint_C z_0(x, y)\, \mathrm{d}x\mathrm{d}y \Big/ \iint_C \mathrm{d}x\mathrm{d}y\ , \tag{4}$$

– with C denoting the domain in x, y space of our deflected microstructure –, to describe this driving force.

2.2 Analytical solution

The time dependent contribution $\Delta n(t)$ to the density in the squeeze-film box is governed by the simple differential equation

$$\frac{\mathrm{d}}{\mathrm{d}t}\Delta n(t) = -n_0 \frac{\mathrm{d}}{\mathrm{d}t}\left(\frac{z_c(t)}{d}\right) - \frac{\Delta n(t)}{\tau} \,, \tag{5}$$

where the first term on the right is the driving force leading the system from equilibrium and the second term represents the relaxation of the system back to equilibrium by the kinetics of free molecular flow. Please note that z_c is defined as pointing upward, out of the squeeze-film box. These equations indeed neglect higher order terms in the displacement $z_c(t)$. In the driving force we use the equilibrium density n_0 as pre-factor because the time derivative contains the z_c-dependency. In the relaxation term the increase Δn is first order in z_c which allows us to use the time- and space-averaged value of the escape time τ.

Assuming a forced plate oscillation $z_c(t) = z_{0,c}\, e^{i\,\omega t}$ according to Eqs. (4) and (1) and a trial solution $\Delta n(t) = \Delta n_0\, e^{i\,\omega t}$ with a complex-valued amplitude Δn_0 we find

$$\Delta n(t) = -\frac{n_0}{d}\,\frac{i\,\omega\tau}{1 + i\omega\tau}\, z_c(t) \,. \tag{6}$$

Assuming that the fluctuations of number density n due to plate oscillation z_c are isothermal, the force of the squeeze-film on the resonator plate F_{squeeze} is readily derived from simple gas kinetics as given by the law of Boyle-Gay Lussac:

$$F_{\text{squeeze}}(t) = \Delta n(t)\, k_B\, T_0\, A, \tag{7}$$

The assumption of an isothermal temperature T_0 is fully justified, because the product of the modulation $\Delta n(t)$ in density and a possible non-isothermal contribution to the temperature would result in higher-order terms in z_c. Applying Eq. (6), the squeeze force reads:

$$F_{\text{squeeze}}(t) = -\frac{p_0\, A}{d}\,\frac{i\omega\tau}{1 + i\omega\tau}\, z_c(t) \,. \tag{8}$$

The effect of this complex-valued force on the oscillating plate can be understood by considering the classical model for the motion of a forced harmonic oscillator, given as a differential equation in the center-of-mass plate displacement $z_c(t)$,

$$m\ddot{z}_c + b\dot{z}_c + kz_c = F_0\, e^{i\omega t}, \tag{9}$$

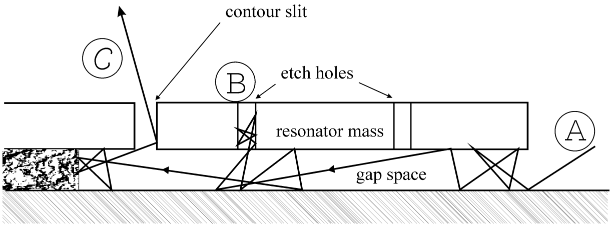

Figure 2: Conceptual picture of molecular random walk, showing a single trajectory in the gap geometry of the devices investigated, which starts at position **A**. We observe a reflection at etch hole **B** and a final escape through contour slit **C**.

with coefficients b and k of the *damping* and *elastic* force term, respectively.

Adding the squeeze force F_{squeeze} and substituting the forced plate oscillation $z_c(t) = z_{0,c}\, e^{i\omega t}$, Eq. (9) reads:

$$-\omega^2\, m z_{0,c} + i\,\omega\left(b + \frac{p_0\, A}{d}\, \frac{\tau}{1+(\omega\tau)^2}\right) z_{0,c} + \left(k + \frac{p_0\, A}{d}\, \frac{(\omega\tau)^2}{1+(\omega\tau)^2}\right) z_{0,c} = F_0 . \qquad (10)$$

Thus we find that the real part of the squeeze force contributes to the elastic force of the oscillator and the imaginary part to the damping force with coefficients k_{squeeze} and b_{squeeze}, respectively, as given by

$$\begin{aligned} k_{\text{squeeze}} &= \frac{p_0\, A}{d}\, \frac{(\omega\tau)^2}{1+(\omega\tau)^2}\,, \\ b_{\text{squeeze}} &= \frac{p_0\, A}{d}\, \frac{\tau}{1+(\omega\tau)^2}\,. \end{aligned} \qquad (11)$$

Here we can make two interesting observations. While the gas pressure p_0 in an ordinary resonant device will only affect the damping coefficient b – becoming manifest in the device's maximum amplitude – it will affect the effective spring constant k in a *squeeze-film* resonator as well. This effect becomes apparent by shifts in the resonance frequency and is due to the phase difference of $\Delta n(t)$ with $z_c(t)$ that occurs when a squeeze-film is present. Figure 1 illustrates this idea.

Secondly, the mix of elastic and damping contributions to the squeeze force at certain frequency depends on the time constant τ of the device. For time constants $\omega\tau \ll 1$ the damping component dominates over the elastic component, whereas for time constants $\omega\tau \gg 1$ the roles have turned around.

3 Determination of time constant τ

3.1 Model calculation

Because the molecules in the squeeze-film box do not interact with each other, they will perform independent random walks in the squeeze-film box (Fig. 2). Collisions will only take place with the gap boundaries, i.e. resonator plate, substrate surface and the adjacent sides. In this way straight-line, randomly oriented gap-crossings of the molecules link together to form random walk trajectories between a random starting point in the gap space and an escape at openings like gap boundary and plate perforations. For a large sample of molecules randomly initiated in the gap space, normalized distribution functions for all sorts of trajectory parameters can be derived showing the collective behavior of molecules in the squeeze-film flow.

In our TPMC approach, we use a routine that initializes the trajectories uniformly in the gap space, by choosing three random numbers $x_0 \in [0, L_b]$, $y_0 \in [0, H_b]$ and $z_0 \in [0, d]$ for the Cartesian coordinates of the initial position. Because we assume that the gas is in thermal equilibrium, Boltzmann statistics determine the initialized velocity vector of each molecule. Simple procedures are available for choosing random values of the Cartesian components v_x, v_y and v_z of this velocity, because Boltzmann statistics are governed by a *Normal* distribution for all components, with variance $\sigma^2 = (\pi/8)\langle v\rangle^2$ and $\langle v\rangle = \sqrt{8k_BT/(\pi m)}$ the average velocity of the molecule.

With regard to the closed edges of the device gap, the diffusing molecules are simulated along their trajectory in a box bounded by a surface plane coinciding with the bottom of the moving plate, by the substrate surface and the edges of the 1.0 µm-thick buried oxide layer. Because of etch holes and the contour slit of the moving plate, the molecule eventually escapes from this box, ending its tracking. The etch holes and contour slits resemble narrow tubes and trenches, giving incident molecules only a limited probability for escaping. This transmission probability can be determined analytically for different geometries and is known as the *Clausing factor* (App. A). A visualization of this phenomenon is shown in Fig. 2 in which we have schematically drawn the random walk of a single molecule bouncing up and down in the gap, attempting to escape. Although the molecule at a certain moment enters an etch hole, it does not escape in this case: it experiences a few bounces on the wall of the hole and is finally reflected back into the gap.

The displacement vector $\vec{s}_j$ for the jth wall-to-wall flight is found by projecting the initial position along the velocity vector on the appropriate box plane. The routine selects the boundary plane of the actual collision according to the direction of the given velocity and the distance from the center of the gap space (App. B). At the new position on the destination plane, the velocity vector is updated with random values

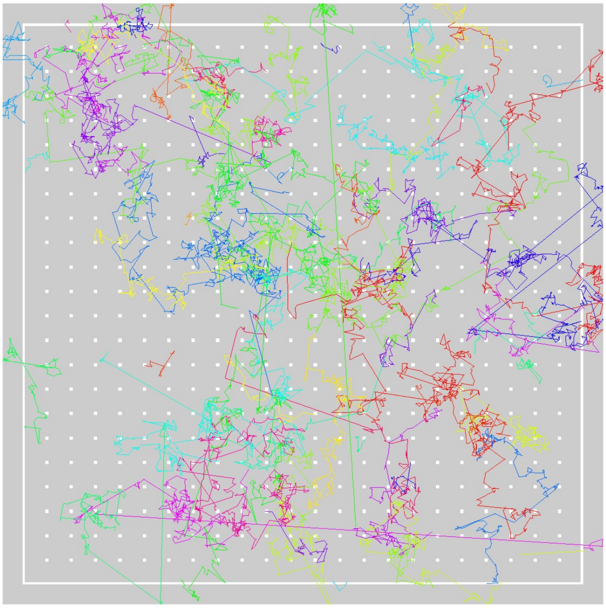

Figure 3: TPMC method for diffusion time calculation of the ’Switch’ device. Trajectories of 80 molecules are simulated to begin at random positions inside the box-shaped gap and terminate on escape through the resonator contour slit and etch holes, respectively. The solid square denotes the ’Switch’ resonator plate above the gap.

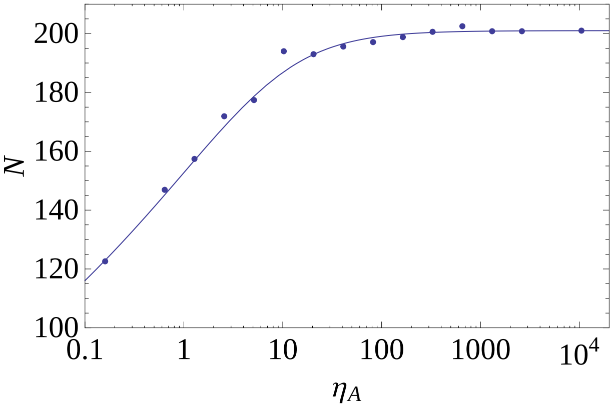

Figure 4: Monte Carlo simulations of the collision number N in a square-contoured gap with features according to that of the 'Switch' resonator (Tab. 3). The data points show the increase over scaled gap footprint η_A.

from a flux-weighted Maxwell distribution (see also appendix A of chapter 2). Again, a simple transformation allows for an easy pick of a random value.

After each collision we assign new, random values to the velocity vector (v_x, v_y, v_z) of the molecule and check if the point of impact coincides with an etch hole or slit:

- if not, we continue the current trajectory;
- if so, we either store the value of the collision number N_i and the accumulated escape time $\tau_{d,i}$ and initialize a new trajectory $(i + 1)$ or continue the current trajectory according to the result of a random draw accounting for the Clausing factor.

In figure 3 we have plotted the trajectories of eighty molecules for the 'Switch' device. We see that most particles leave the squeeze-box through the etch holes in the plate. Furthermore, we observe the characteristic behavior of local random walk interrupted by surprisingly long jumps, as determined by the asymptotic behavior $\sim 1/r_1$ of the distribution function for the displacement r_1 in a single crossing between top and bottom of the squeeze-box (or vice versa).

We do not consider molecules wandering off in the gap region outside the contours of the device plates: in our procedure, we use a gap that is simply framed by the rectangular shape of the plates. This simplification, to prevent the more tedious

Table 1: Results of the time constants τ_{fit}, τ_{sum} and $\tau_{1/e}$ for the three resonators investigated. Additionally the values of the parameters α and λ for the curve-fitted gamma functions through the Monte Carlo results for $P(\tau_d)$ are listed. The numbers between parentheses denote the fractional difference in value as compared to τ_{sum}.

Method		**Dog bone**	**Square plate**	**Switch**
Curve-fit	α (-)	1.195	1.091	1.452
	λ (μs^{-1})	1.515	0.358	2.045
	τ_{fit} (μs)	0.79 (-12%)	3.05 (-7%)	0.71 (+10%)
Summation	τ_{sum} (μs)	0.90	3.25	0.65
(1/e)-point	$\tau_{1/e}$ (μs)	0.75 (-16%)	2.95 (-10%)	0.67 (+3%)

collision-site detection around springs and anchors, is fully justified for our devices that are riddled with etch holes.

Simulations in a square-contoured gap with features of the resonators investigated (see 'Switch' Tab. 3) show that the collision number N hardly increases with the scaled value $\eta_A = L^2/L^2_{\text{Switch}}$ of the area of the device, with L a measure for the lateral extent. Numerical results are shown in Fig. 4. In the operational point $\eta_A = 1$, the dependency can be linearized to

$$\eta_A = 1 : \qquad \mathrm{d}N/N = 0.11\,\mathrm{d}\eta_A/\eta_A \tag{12}$$

A 20% increase in plate area results in only 2% extra collisions of a molecule to escape from the gap, with a correspondingly small increase of the escape time. This is well within the systematic error of our analytical model due to its simplifications.

The routine developed in this way, was written and run in *Mathematica*[1] to produce graphics and statistical output in a user-friendly manner. Besides escape time τ_d and collision number N, the procedure also stores other properties of the trajectory to investigate the diffusion process such as accumulated path length $S = \sum_j^N |\vec{s}_j|$ or average wall-to-wall flight time $\langle \tau_{\text{flight}} \rangle = \frac{1}{N} \sum_j^N \tau_{\text{flight},j}$ and is repeated to improve statistical accuracy in these parameters.

On our system (x86, Intel Xeon, 64 bit) the calculation for a sample of $n = 10^5$ trajectories in the resonator gap (typically $N = 150$ collisions) takes ten minutes, which is fast enough for implementation in a MEMS design code. We have checked that the variance in the sample mean $\tau = \langle \tau_d \rangle$ in different sample runs (each with $n = 10^5$ trajectories) follows the expected behavior according to $\sigma_\tau^2 \propto 1/n$.

---

[1] Version 7 by Wolfram Research Inc., UK

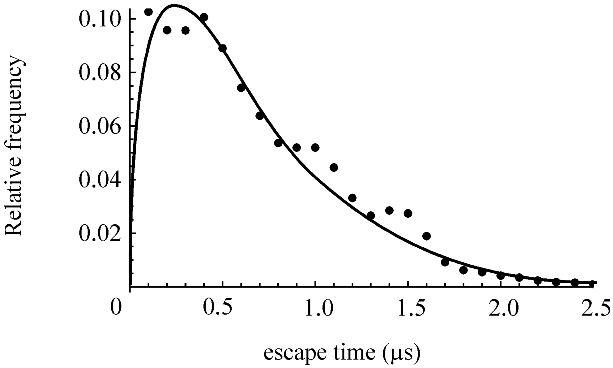

Figure 5: Normalized distribution function $P(\tau_d)$ for the escape time τ_d for the 'Switch' resonator investigated in this paper.

3.2 Escape-time distribution function

In figure 5 we show the Monte Carlo result for the normalized distribution function $P(\tau_d)$ for the escape time τ_d for the 'Switch' resonator investigated in this paper. The deviations from a smooth curve are significant and not the result of stochastic noise due to a finite sample size. The data points have been averaged by using a 0.1 μs time-bin. The solid line represents a least-squares curve-fit with the gamma density function $\Gamma(t; \alpha, \lambda)$.

The distribution function $P(\tau_d)$ is the input to determine the time constant τ as introduced in Eq. (5). Solving this equation without the external term due to the plate motion, we find a solution

$$\Delta n(t) = \Delta n(0) \exp(-t/\tau), \tag{13}$$

showing a simple exponential decay of the initial deviation $\Delta n(0)$ of the density inside the gap from its equilibrium value n_0 outside the gap. The remnant particle fraction $\zeta(t) = \Delta n(t)/\Delta n(0)$ directly derives from $P(\tau_d)$ if we start summing up the escape frequencies from $\tau_d = 0$ to $\tau_d = t$ and subtract the total from 1, as given by

$$\zeta(t) = 1 - \int_0^t P(\tau_d)\, \mathrm{d}\tau_d \, . \tag{14}$$

The shape of this particle fraction for the 'Switch' device resembles an exponential function with a single time constant that can be determined from either the $1/e$ decay point or the average value. Due to the deviations of $P(\tau_d)$ from the simple exponential, however, we have to carefully investigate the most appropriate method to derive the time constant τ in Eq. (5) from this distribution function. We now discuss three different recipes to determine the value of τ. The variance in the outcome of these different methods will provide us with an indication of the accuracy of the value of τ.

First, we apply a method that takes into account the shape of $P(\tau_d)$, by performing a least squares curve-fit of $P(\tau_d)$ with the gamma density function $\Gamma(t; \alpha, \lambda)$ with $\alpha > 0$ and $\lambda > 0$. The result of this curve-fit is given in Fig. 5. We observe a fairly good description of $P(\tau_d)$, apart from the extra wiggles that are specific for the device. The average value for the time constant based on this curve-fit is given by

$$\tau_{\text{fit}} = \alpha/\lambda. \tag{15}$$

We observe that for the 'Switch' device the Gamma function overestimates the distribution for large values of the escape time, which will result in too large values of τ_{fit}.

Next, we calculate τ by straight-forward averaging of the discrete results for $P(\tau_d)$, as given by

$$\tau_{\text{sum}} = \sum_{i=0}^{\infty} \tau_{d,i}\, P(\tau_{d,i}) \tag{16}$$

over all time bins with index i. This last method takes into account all details of the Monte Carlo results, which cancels the errors introduced by using a curve-fit.

Finally, to connect to the analytical solution of the homogeneous solution of Eq. (5), we determine τ by solving

$$\zeta(\tau_{1/e}) = 1/e\,, \tag{17}$$

which neglects details of the specific shape of the distribution function $P(\tau_d)$. This is a rather simple choice which (1) puts most emphasis on the high frequency end of the distribution function and (2) is sensitive to details of the distribution function such as the observed wiggles and is sensitive to the shot-noise involved.

The results for the time constant τ of these three recipes are compiled in Tab. 1, for all three devices investigated in this paper. We see that the different time constants have quite similar values. The differences between τ_{fit} and τ_{sum} correlate with an underestimation ('Dog-bone', 'Square plate') or an overestimation ('Switch') of the Monte Carlo data by the curve-fit, respectively. This same behavior is also reflected in the results for $\tau_{1/e}$: an underestimation of the tail for long escape times corresponds to a faster decay at short times, resulting in a smaller value of the time constant $\tau_{1/e}$ and vice versa. The calculation of the average value τ_{sum} directly from the Monte Carlo results of the distribution function $P(\tau_d)$ takes into account all details of the

Table 2: Experimental squeeze-film damping coefficient b_{squeeze} at $p = 1$ Torr of the ”310 µm -nocap” device as measured by Legtenberg et al. [17], in comparison to the calculated results of Leung et al. and the results of our fast-prototyping TPMC approach. The number between parentheses indicates the error in the last digit.

Property	Definition	Value
Material		Silicon
Density	ρ (10^3 kg/m^3)	2.33
Plate area	A_{plate} (µm^2)	310×100
Plate thickness	D (µm)	1.5
Gap width	d (µm)	1.18
Effective mass	m (µg)	0.11
Resonance frequency	$\omega_0/(2\pi)$ (kHz)	163
Quality factor	Q	71(4)
Expt. damping coeff.	$b_{\text{squeeze,expt}}$ (10^{-6} kg/s)	1.51(8)
Leung damping coeff.	$b_{\text{squeeze,Leung}}$ (10^{-6} kg/s)	1.31(7)
Model damping coeff.	b_{squeeze} (10^{-6} kg/s)	1.40(4)
Time constant	τ (µs)	1.89 (10)

specific device. For this reason it is our time constant of preference. In this paper we will use

$$\tau \equiv \tau_{\text{sum}} \tag{18}$$

when referring to a calculated result for the time constant.

3.3 Test of TPMC method

As a test of our TPMC routine we have calculated the squeeze-film damping coefficient b_{squeeze} of the ”310 µm -no cap” device of Legtenberg et al. [17] at $p = 1$ Torr. We compare this value to the experimental value derived from Legtenberg’s Q vs. p plot. Because we are in the pressure range far from the low pressure region featuring

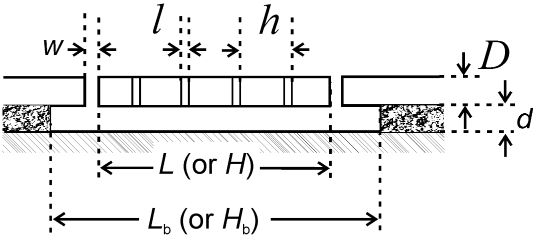

Figure 6: Cross section of SOI resonators investigated.

Q values constant with pressure, damping is gas dominated and we may use:

$$\begin{aligned} b_{\text{squeeze,expt}} &\simeq b_{\text{expt}} - b_{\text{kin}} \,, \\ &= \frac{m\,\omega_0}{Q} - \frac{16\,A_{\text{plate}}}{\pi\,\langle v\rangle} \cdot 1\ \text{Torr} \end{aligned} \tag{19}$$

with $m = \rho\,A_{\text{plate}}\,D$ as the effective resonator mass and b_{kin} as the kinetic damping contribution according to Christian [18]. Table 2 lists the device properties and modeling results. The error margin of the quality factor stems from extracting it from the plot. The error margin of the modeled squeeze damping coefficient follows from the range of possible time constants, formed by the values of τ_{fit}, τ_{sum} and $\tau_{1/e}$ as described in the previous section.

Finding good agreement of our model outcome with the experimental damping value, we assume our TPMC method to be valid.

4 Devices

We test our model on the basis of experimental data on three distinct uncapped resonators. The resonators are produced on a Silicon-On-Insulator (SOI) substrate using surface micro-machining. Contours of the structures are patterned onto the substrate and etched through the top silicon layer, cutting out the resonator features. To facilitate the wet etch of the 1.0 μm intermediate oxide layer, all plates and wide beams are perforated with $l \times l$ sized holes in a $h \times h$ spaced grid. Thus a free-standing structure results, with a gap distance to the substrate $d = 1.0$ μm (Fig. 6). The devices are labeled 'Dog bone', 'Square plate' and 'Switch' and operated in out-of-plane resonant modes subjected to squeeze-film damping in the gap between resonator and substrate. Characteristic dimensions are given in Tab. 3.

Mode shapes and resonance frequencies of the respective designs were deter-

Table 3: Characteristic parameters of the three MEMS devices. Resonance frequency $\omega_{0,\mathrm{mat}}$ and spring constant k_{mat} as calculated from a finite-element simulation using COMSOL. Value of τ according to TPMC calculation.

Property	**Definition**	**Dog bone**	**Square plate**	**Switch**
Gap frame	$L_b \times H_b$ (μm^2)	112×62	172×172	172×172
Gap width	d (μm)	1.0	1.0	1.0
Unit cell size	$h \times h$ (μm^2)	7.0×7.0	9.0×9.0	7.0×7.0
Etch hole size	$l \times l$ (μm^2)	0.8×0.8	0.5×0.5	0.8×0.8
Trench width	w (μm)	0.8	0.2	0.8
Plate area A	$L \times H$ (μm^2)	100×50	160×160	160×160
Plate thickness	D (μm)	1.5	1.5	1.5
Spring length	s (μm)	18	18	50
Spring width	t (μm)	16	4	10
Spring constant	k_{mat} (N/m)	54	71	43
Frequency	$\omega_{0,\mathrm{mat}}/2\pi$ (kHz)	228	137	187
Etch hole[a]	W_{hole} (-)	0.41	0.30	0.41
Trench[a]	W_{slit} (-)	0.55	0.29	0.55
Time constant	τ (μs)	0.90	3.25	0.65

---

[a] Clausing factor thereof (App. A)

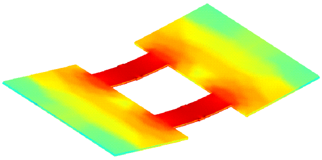

Dog bone

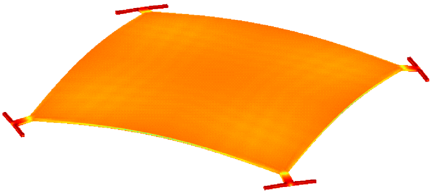

Square plate

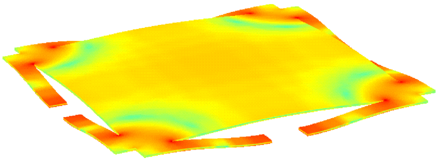

Switch

Figure 7: Mode shapes and strain energy volume distribution of the resonator structures investigated. The etch holes present in the real devices were omitted to facilitate meshing for the FEM simulations.

mined from finite-element (FEM) simulations using *COMSOL Multiphysics*[2]. Assuming quality factors in the usual range ($Q > 10$), these resonance frequencies will show a perfect match with the corresponding eigenfrequencies $\omega_{0,\mathrm{mat}}$. Thus, for each design, an eigenfrequency analysis was setup for simulation of the lowest bending mode resonance. For unproblematic meshing of the domains the etch holes in the various structures were omitted here. In the simulation output, data of several quantities is processed and can be plotted for each quantity individually on the domain of the structure. In this way plots of the mode shapes as well as strain energy distribution were produced for the devices investigated (Fig. 7). The eigenfrequencies $\omega_{0,\mathrm{mat}}$ found are listed in Tab. 3.

Furthermore, the effective stiffness k_{mat} of the structures in the simulated mode shapes was determined. For this, the strain energy distribution was integrated over the microstructure volume to give the total amount of elastic energy U stored at the simulated deflection. Because the microstructure is actuated by a uniform force distribution, the effective stiffness k_{mat} satisfies

$$U = \frac{1}{2} k_{\mathrm{mat}}\, z_{cm}^2, \tag{20}$$

with z_{cm} the domain averaged deflection of the microstructure.

The value of z_{cm} is found from a volume integration of the local out-of-plane displacement $z(\mathbf{r})$ on the microstructure domain C, as given by

$$z_{cm} = \int_C z(\mathbf{r}) \mathrm{d}^3\mathbf{r} \Big/ \int_C \mathrm{d}^3\mathbf{r}. \tag{21}$$

As a last input to the sample property list in Tab. 3 we add the calculated diffusion time τ of the respective device gaps as discussed in Sec. 3.

5 Experimental results

To determine pressure sensitivities $|\mathrm{d}b/\mathrm{d}p|$ and $|\mathrm{d}k/\mathrm{d}p|$ for damping and stiffness of the devices, respectively, we measured the quality factors Q and resonance frequencies ω_0 for a range of vacuum pressures. Therefore we mounted the devices in a vacuum chamber with a base pressure less than 1×10^{-5} mbar. With a leak valve we introduced nitrogen gas to achieve the desired pressure in the 1×10^{-3} to 1.0 mbar range. The pressure was measured with an MKS Baratron 627B capacitance manometer with an accuracy of 0.1 %.

---

[2] Version 3.4 by COMSOL AB, Sweden

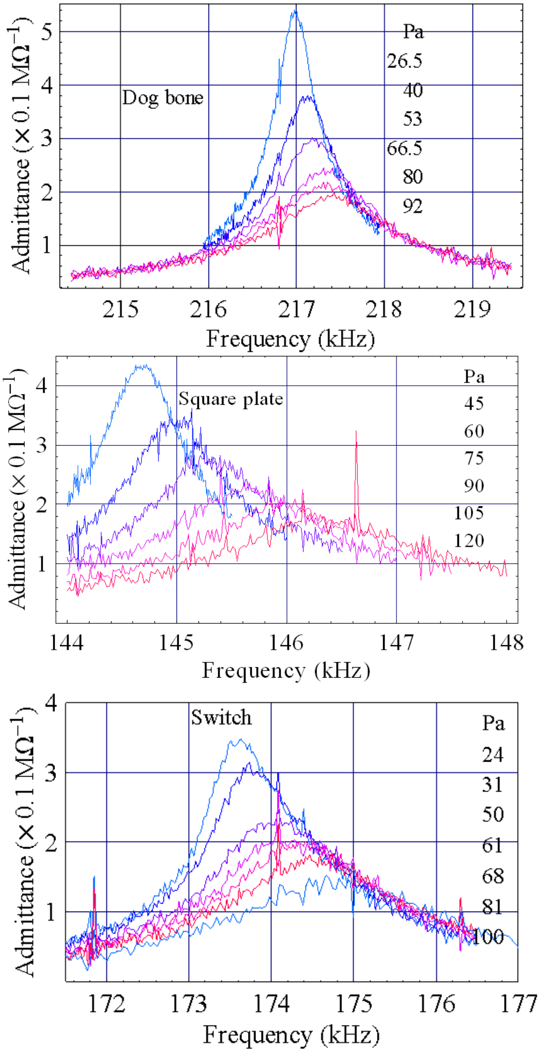

Figure 8: Electrical transmission signals of the capacitively measured resonator devices for a range of N_2-pressures at room temperature.

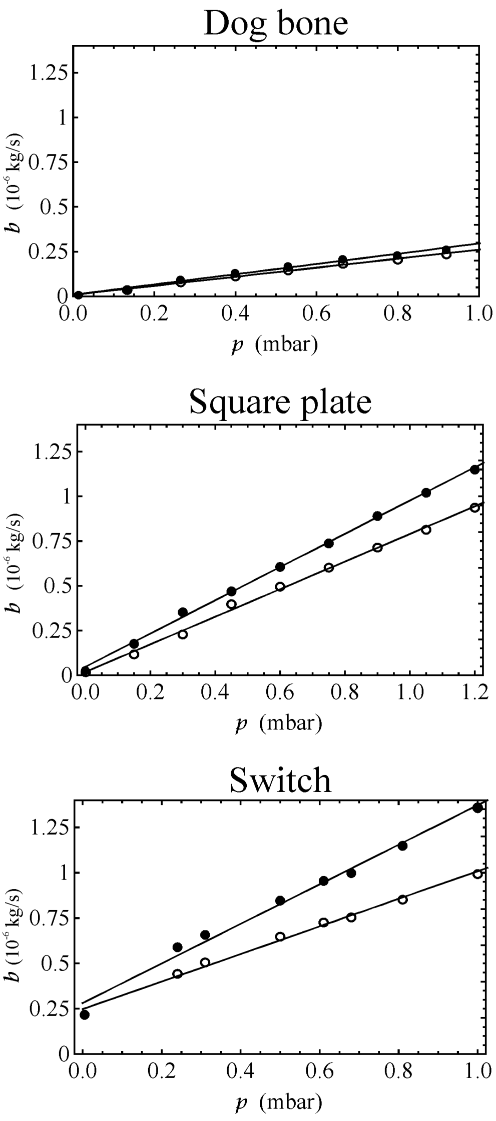

Figure 9: Experimental results of damping coefficients b vs. N_2-pressure for the investigated resonators. The open symbols represent Q-based values and the filled symbols R-based values respectively.

The electrical readout of the amplitude of the oscillating plate is straightforward. The microstructure in the top silicon substrate layer and the substrate form a variable capacitor. Microstructure motion was detected via capacitance changes measured using an HP4194A impedance analyzer. At resonance, the plate amplitude rises and more mechanical energy is dissipated in the ambient gas. Since this dissipated energy must be supplied by the analyzer, a peak is seen in the magnitude of the admittance $|Y|$. This admittance magnitude directly links to the mechanical behavior of the microstructure as a result of electrostatic coupling.

We measured the frequency response of the device to determine the quality factor Q as well as the ohmic dissipation R on resonance. The experimental results are shown in Fig. 8. For different values of the pressure in the vacuum chamber, ranging from 0.13 to 1.20 mbar, the electrical transmission signals of the respective devices are shown as a function of the generator frequency ω. We clearly see the decrease of the quality factor with increasing pressure and observe also a significant shift of the resonance frequency as expected from theory (Fig. 1). The signal of the 'Switch' however, does not entirely fit to the behavior of the ideal harmonic oscillator as appears from asymmetry in the narrow resonance curves at high values of the quality factor Q.

Quality factors Q are determined with a least-squares curve fit to a Lorentzian peak function H at resonance frequency ω_0:

$$H(\omega) = H_0 \bigg/ \sqrt{4\left(\frac{\omega}{\omega_0} - 1\right)^2 + \frac{1}{Q^2}} \tag{22}$$

Here, H_0, ω_0 and Q are mutually independent fit parameters.

In Fig. 9 we show the experimental results for the damping b as a function of the N_2-pressure in the test chamber at ambient temperature $T = 22$ °C. Here, clear linear pressure dependencies turn up, as our theory predicts. We calculate the damping coefficients b, using the relation $b = k_{\text{mat}}/(\omega_0\, Q)$ with k_{mat} the simulated stiffness of the microstructure in the excited resonance mode which is listed in Tab. 3. We refer to these values as 'Q-based'.

For the 'Switch' we observe a finite offset at $p = 0$ of the straight-line curve-fit of the experimental b-values. In our opinion, this is due to the observed asymmetry in the underlying resonance profiles. A consequence of this phenomenon is the underrating of the quality factor Q – and thus an overrating of the damping – when curve fitting the experimental resonance profiles with the ideal response as given in Eq. (22). This effect is much less pronounced for the low-Q resonance curves at the highest pressures used in our experiments. For a correct analysis we have to limit ourselves to this pressure range and force the straight-line curve-fit of the b-values through the origin ($p = 0, b = 0$). In Tab. 4 we present both methods of analysis, i.e.,

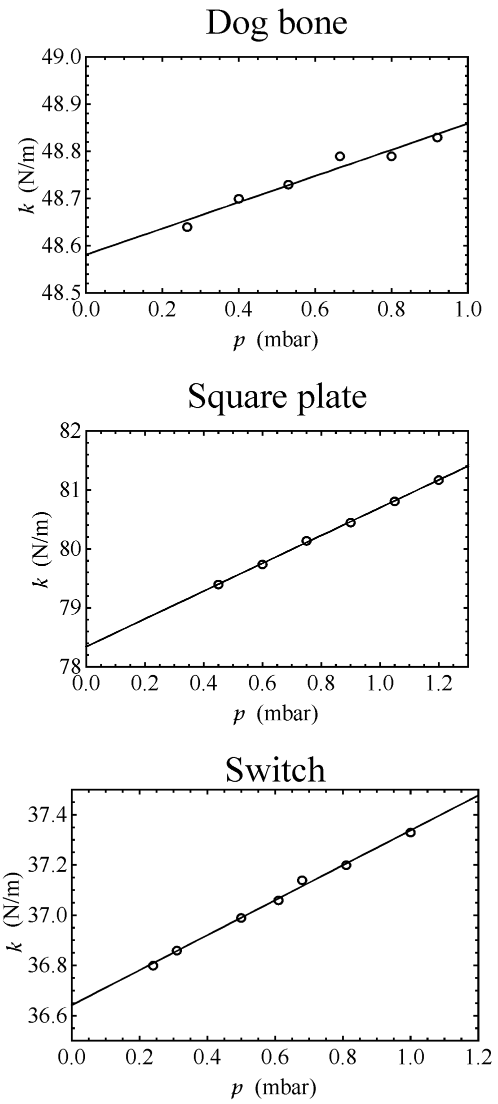

Figure 10: Experimental results of resonator stiffness k vs. N_2-pressure, as calculated from the observed resonance frequencies ω_0 of the investigated resonators.

with and without an allowed offset.

In Fig. 9 we also show the damping coefficient b of the resonator from its motional resistance $R = 1/Y(\omega_0)$, where $Y(\omega_0)$ is the admittance at resonance. We refer to these values as 'R-based'. Using the physical model for a resonator of two parallel capacitor plates, the relationship between R and b can be derived as:

$$b = \epsilon_0^2 \, V_{\mathrm{DC}}^2 \, (A/d^2)^2 \, R \equiv \eta^2 \, R, \tag{23}$$

defining the electrostatic coupling constant η as

$$\eta \equiv \frac{\mathrm{d}}{\mathrm{d}z} C_{\mathrm{plate}} \, V_{\mathrm{DC}} = \epsilon_0 \, V_{\mathrm{DC}} \, (A/d^2). \tag{24}$$

Here η is determined by the gradient of plate capacitance C_{plate}. Except for the dielectric constant ϵ_0 of the vacuum in the resonator gap, this constant only depends on the bias voltage V_{DC}, the plate surface area A and the gap width d between plate and substrate. With Eq. (24) we can understand why R-based data lead to larger damping coefficients than Q-based data for 'Switch' and 'Square plate' and to smaller coefficients in case of the 'Dog bone' device. Because only part of the surface area A of the 'Switch' and 'Square plate' membranes (see mode shapes Fig. 7) undergo deflection, the assumed situation of planar parallel plates just overrates η for these two devices. At the same time this assumption underrates η for the 'Dog bone' device, because the plate surfaces accounted for are tilted with respect to the substrate as shown by the mode shape. For that matter Puers et al. [19] show that the (gradient of) plate capacitance for tilted plates exceeds that of parallel plates.

In Fig. 10 we show the experimental results for the stiffness k as a function of the N_2-pressure. Again, we discover a prominent linear dependence on pressure as marked by a straight-line fit. The stiffness k is calculated from the observed resonance frequencies ω_0 using the relation $k = m\,\omega_0^2$, where the effective mass $m = k_{\mathrm{mat}}/\omega_{0,\mathrm{mat}}^2$ results from the finite-element simulation as listed in Tab. 3.

Because the model-based pressure dependence of b_{squeeze} and k_{squeeze} is linear, see Eq. (11), we only need the slopes of straight-line fits to the measured data of b and k to find the device characteristic pressure sensitivities β and κ:

$$\begin{aligned} \frac{\mathrm{d}}{\mathrm{d}p} b_{\mathrm{squeeze}} &\equiv \beta \\ \frac{\mathrm{d}}{\mathrm{d}p} k_{\mathrm{squeeze}} &\equiv \kappa. \end{aligned} \tag{25}$$

Comparison with the model-based sensitivities will thus show the accuracy of our model. Because the margin of relative error on the individual damping constants and

Table 4: Summary of the experimental results in figures 9 and 10. Next to the experimental frequency values (expt) the COMSOL simulated values are listed. The number between parentheses indicates the error in the last digit.

Device	**Frequency** $\omega_0/2\pi$ (kHz)		β (10^{-6} kg/s mbar)		κ (N/m mbar)
	expt	sim	Q-based	R-based	
Dog bone	218.4	228	0.20(1)	0.16(1)	0.29(3)
Square plate	144.6	137	0.89(4)	0.95(4)	2.21(4)
Switch	174.1	187	0.76(3)	1.09(5)	0.70(2)
Switch[a]			1.12(20)	1.49(24)	

---

[a] If curve-fit of $b(p)$-data is forced through the origin

frequency shifts is less than one percent, the error in β and κ is completely determined by the residuals of the linear regression curve fit. A summary of the results for the different devices is given in Tab. 4. The discrepancy in measured ('expt') and simulated ('sim') frequencies is on the order of 5%. We can attribute this to the omission of the etch holes in our FEM simulation and the difference between nominal plate thickness used for simulation and the actual thickness on the measured device wafer, as caused by the process spread in the production.

6 Analysis

From the values of the observables β and κ we can determine the operation point $\omega_0\tau_{\text{expt}}$ of each measured resonator. Manipulating the model expressions of Eq. (11) we can easily find an explicit solution for $\omega_0\tau_{\text{expt}}$ using only one of these observables. Considering β, we obtain the simple equation:

$$\beta\,(\omega_0\tau_{\text{expt}})^2 - \frac{A}{\omega_0\,d}\,(\omega_0\tau_{\text{expt}}) + \beta = 0 \tag{26}$$

$$\omega_0\tau_{\text{expt}} = \frac{A}{2\omega_0\,d\beta} \pm \sqrt{\left(\frac{A}{2\omega_0\,d\beta}\right)^2 - 1} \tag{27}$$

As the solution of $\omega_0\tau_{\text{expt}}$ has two roots in Eq. (27), the value of κ decides which root is the true solution. For $\kappa > A/(2d)$, the plus sign applies and the largest root of $\omega_0\tau_{\text{expt}}$ gives the correct solution. Otherwise, the smallest root applies.

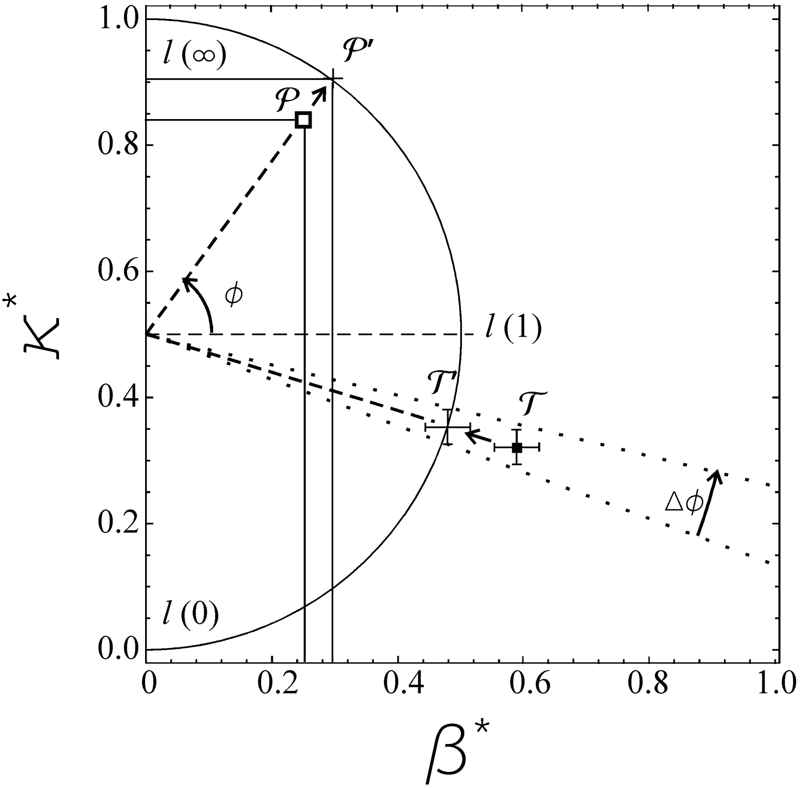

Figure 11: Illustration of the construction method of the operation point $\omega_0\tau$ for two resonators with experimental values of β^* and κ^* represented by $\mathcal{P}$ and $\mathcal{T}$.

Although this solution method works fine for β and κ values that perfectly match the squeeze model, problems emerge when experimental errors in the observables have to be dealt with. In the worst case, the discriminant of the parabola in $\omega_0\tau$ (left-hand side of Eq. (26)) turns negative which implies that no relevant solution for $\omega_0\tau_{\text{expt}}$ can be given.

For this reason we developed a method that relies on a geometrical construction from the observed (β, κ) pair. By doing so, $\omega_0\tau_{\text{expt}}$ values result from orthogonal projection of the observations onto the locus (β, κ; t) of our model. We clarify this statement in the next section.

6.1 Method

The locus of our model is parametrized by the curve $l(t)$:

$$l(t) \equiv \begin{pmatrix} \beta^* \\ \kappa^* \end{pmatrix} = \frac{t}{1+t^2} \begin{pmatrix} 1 \\ t \end{pmatrix}, \tag{28}$$

in which t runs through values of $\omega_0 \tau \in [0; \infty]$. The orthogonal coordinates β^* and κ^* of the curve represent the normalized sensitivities of damping and stiffness to pressure p:

$$\begin{aligned} \beta^* &= \frac{\omega_0\, d}{A} \beta \\ \kappa^* &= \frac{d}{A} \kappa \end{aligned} \tag{29}$$

Figure 11 shows the parametric curve and the construction of it. We see that $l(t)$ defines a *semi-circle* in the $\beta^* \kappa^*$-plane, centered at $(0, \frac{1}{2})$, with radius $\frac{1}{2}$. At the origin $(0, 0)$, the value of $\omega_0 \tau$ is zero; halfway up the curve, in $(\frac{1}{2}, \frac{1}{2})$, we find $\omega_0 \tau = 1$ and at the end, in $(0, 1)$, the value of $\omega_0 \tau$ goes to infinity.

Operation point $\omega_0 \tau$ of observation $\mathcal{P}$ with associated projection $\mathcal{P}'$ is found using the angle ϕ:

$$\tan \phi = \frac{\kappa^* - \frac{1}{2}}{\beta^*}. \tag{30}$$

By using the relation

$$\kappa^* / \beta^* = \omega_0 \tau, \tag{31}$$

as follows from Eqs. (11) and (29), the operation point in terms of ϕ reads

$$\omega_0 \tau = \frac{1 + \sin \phi}{\cos \phi}. \tag{32}$$

The error $\Delta(\omega_0 \tau)$ in the operation point due to an error $\Delta\phi$ in the polar angle is determined by the derivative of latter equation:

$$\Delta(\omega_0 \tau) = \left(\frac{1 + \sin \phi}{\cos^2 \phi} \right) \Delta\phi. \tag{33}$$

The error $\Delta\phi$ arises from a projection of the error bars in β^* and κ^* components of an observation. The largest of these two projections determines $\Delta\phi$. In Fig. 11 this process is illustrated for the device with experimental result $\mathcal{T}$. The error in polar angle is indicated by the radial lines enveloping the error bars of the observation at its projected position $\mathcal{T}'$. Parametrizing the locus in terms of the angle ϕ:

$$\begin{pmatrix} \beta^* \\ \kappa^* \end{pmatrix} = \frac{1}{2} \begin{pmatrix} \cos\phi \\ 1 + \sin\phi \end{pmatrix}, \tag{34}$$

the error $\Delta\phi$ yields two distinct expressions (depending on ϕ, $\Delta\beta^*$ and $\Delta\kappa^*$); we use whichever gives the greatest value:

$$\Delta\phi = \max\left[\frac{2\,\Delta\beta^*}{|\sin\phi|}, \frac{2\,\Delta\kappa^*}{\cos\phi}\right] \tag{35}$$

6.2 Experimental results

Processing the data in this way at the same time brings to light the consistency of the pressure sensitivities $|\mathrm{d}b/\mathrm{d}p|$ and $|\mathrm{d}k/\mathrm{d}p|$ for damping and stiffness of the devices. Here we see that our model predictions for β^* and κ^*, as direct representatives of these pressure sensitivities, agree almost within the measurement accuracy with the observations. For a correct analysis of the 'Switch' device that exhibited abnormal offset (see Sec. 5) we derived β^*_{expt} from a curve-fit of $b(p)$-data forced through the origin. Thus we also find good agreement ($\pm 10\%$) for the experimental values of $\omega_0\tau$. This is independent of the measurement method for the damping. Table 5 summarizes the data obtained accordingly. Figure 12 shows the result of this analysis for our three devices graphically. The left graph clearly illustrates the difference in operation point, not only between distinct resonators but also between the two measurement methods for the damping constant (Q-based or R-based). The magnified views clarify the error bars of β^* and κ^* and how the model prediction (the cross mark right on the semi-circle curve) relates to the experimental value. In the lower of these views we also indicate the corrected data points for the 'Switch' resonator. The extrapolation at equal value of polar angle ϕ starting out from the model prediction (upper cross mark) in this view shows the model-to-experiment agreement for $\omega_0\tau$ of the 'Switch' as well.

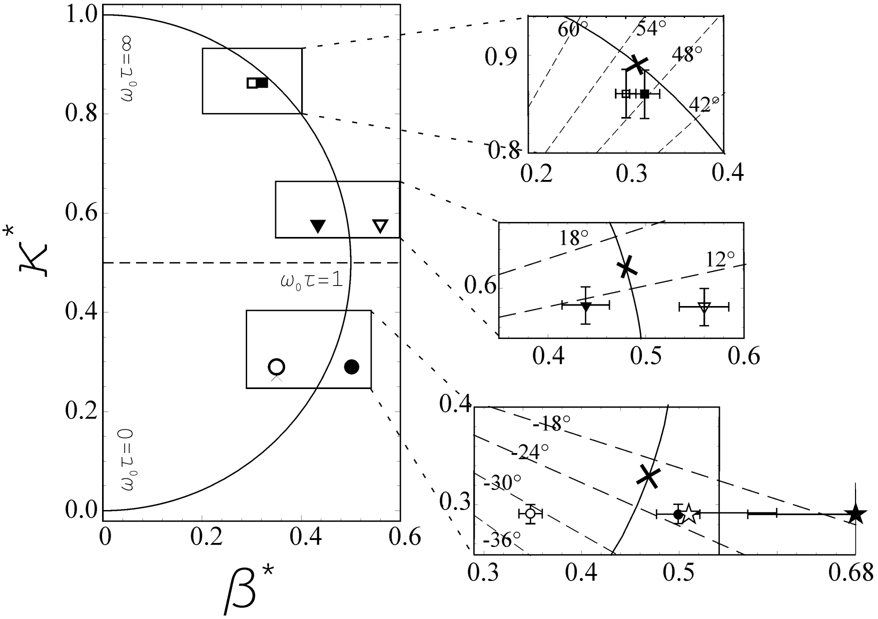

Figure 12: Result of (β^*, κ^*)-analysis for the devices investigated. The ▼, ■, ● symbols denote the observations of 'Dog bone', 'Square plate' and 'Switch' device, respectively. Open symbols represent Q-based, filled symbols R-based observations. The cross marks right on the curve display the (β^*, κ^*) model prediction of each device (associated to 'Square plate', 'Dog bone' and 'Switch' resonator from top to bottom). The ★ symbol denote corrected observations of the 'Switch' device.

Table 5: Summary of the results of data analysis using the method of Sec. 6. For close comparison the simulated values of $\omega_0\tau, \beta^*$ and κ^* were added. The subscript 'expt' applies to the experimental value of ω_0 used as well as to the value of τ in the $\omega_0\tau$-product. Numbers in parentheses indicate the error in the last digit.

		Experimental					Model		
Device	**Method**	β^*_{expt}	κ^*_{expt}	ϕ_{expt} (°)	$\Delta\phi$ (°)	$\omega_0\tau_{\text{expt}}$	$\omega_0\tau$	β^*	κ^*
Dog bone	*Q*-based	0.56(2)	0.58(2)	8.3	1.0	1.16(2)	1.3(1)	0.49(1)	0.62(5)
	R-based	0.43(1)	0.58(2)	11	1.0	1.21(2)	1.3(1)	0.49(1)	0.62(5)
Square plate	*Q*-based	0.30(1)	0.86(3)	51	2.3	2.8(2)	2.8(3)	0.32(2)	0.89(2)
	R-based	0.32(1)	0.86(3)	49	2.2	2.7(2)	2.8(3)	0.32(2)	0.89(2)
Switch	*Q*-based	0.35(1)	0.29(1)	-31	1.5	0.57(2)	0.75(8)	0.47(1)	0.33(5)
	R-based	0.50(2)	0.29(1)	-23	3.4	0.67(4)	0.75(8)	0.47(1)	0.33(5)
Switch[a]	*Q*-based	0.51(9)	0.29(1)	-22	14	0.7(2)	0.75(8)	0.47(1)	0.33(5)
	R-based	0.7(1)	0.29(1)	-17	22	0.7(3)	0.75(8)	0.47(1)	0.33(5)

---

[a] If curve-fit of $b(p)$-data is forced through the origin

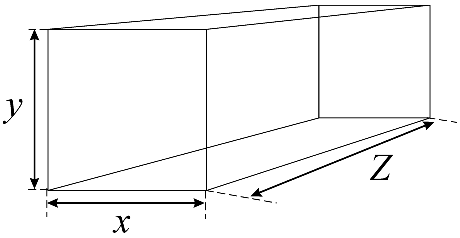

Figure 13: Geometrical representation of etch hole/trench with length Z and opening $x \times y$.

7 Concluding remarks

We developed a simple model for squeeze-film forces in MEMS resonators in the free molecular flow regime. It is based on the response of the gas molecules in the gap volume on the oscillatory behavior of the MEMS plate, as captured in a single time constant τ according to Eq. (5).

Our model facilitates model-based design of MEMS resonant pressure sensors and capitalizes on the convenient way free molecular flow can be solved numerically with Monte Carlo simulations. Based on the model, we have designed and fabricated three MEMS resonators that can serve as pressure sensors. Pressure read-out can be done either by monitoring the increase in damping or the shift in operating frequency. The experimental results in both read-out modes are consistent with the model predictions, within an accuracy of typically 10%. This demonstrates the value of the model for designing new devices, avoiding trial and error loops to meet the desired specifications.

A Clausing factor of etch holes and trenches

For the calculation of molecular flow through geometrically well-defined parts of vacuum systems, analytical expressions of flow rates exist long since the early twentieth century. For tubes and orifices Knudsen [20] and Smoluchowski [21] published the first expressions for molecular flow rate. Although exact for very large and very small length-to-diameter (Z/x) ratios (Fig. 13), these expressions are in considerable error if applied to ducts of realistic proportions. For this reason Clausing [22] solved the problem for isolated ducts of any length, considering kinetic instead of macroscopic quantities. He showed that the molecular flow rate K can be expressed in the form:

$$K = W\, S\, \Psi \tag{36}$$

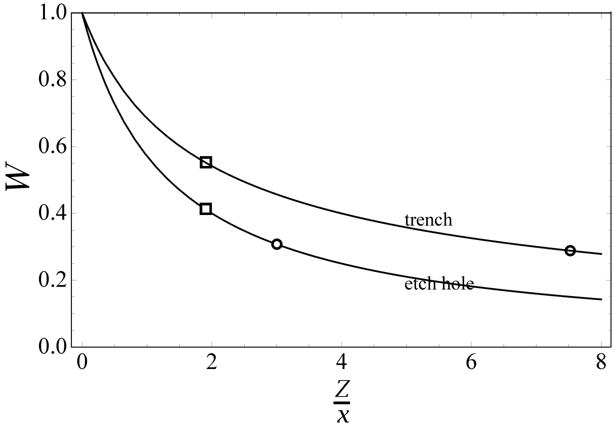

Figure 14: Clausing factor W for the etch holes and trenches of our devices as a function of normalized length Z/x. The □ symbols refer to etch holes ($y/x = 1$) and trenches ($y/x = \infty$) of 'Dog bone' and 'Switch' device, the ○ symbols refer to the 'Square plate' device. See Tab. 3 for particular values.

Here, S is the area of the tube entrance, $\Psi = n\langle v\rangle/4$ the current density of incident molecules and W the transmission probability, i.e. the probability that an incident molecule exits the tube without returning to the tube entrance. It solely depends on tube geometry and approaches to unity if the length-to-diameter ratio (Z/x) becomes zero. Clausing formulated an integral equation in terms of the transmission probability W for which he gave an approximate solution. His values for W have been used ever since and are often called *Clausing factors*. These analytical values will do perfectly as practical estimate but for improved accuracy full Monte Carlo simulations are necessary. The work of Beijerinck et al. [23] gives an example of such approach.

Clausing derives the probability W_{hole} of an etch hole, represented by a tube of length Z with rectangular opening $S = x \times y$, to be:

$$W_{\text{hole}} = \left[\frac{3}{8}\left(\frac{Z}{x} + \frac{Z}{y}\right) + 1\right]^{-1} \tag{37}$$

In the limit of $y/x = \infty$ the opening becomes a slit of width x. The Clausing factor W_{slit} of this slit applies to etch trenches in our devices. See Eq. (46) of Clausing [22] for the elaborate, closed-form expression. Figure 14 shows numerical values of the Clausing factor for the etch holes and trenches of our devices as a function of length-to-diameter ratio Z/x. Here, symbols mark the specific values: the open ones refer to the trenches and closed ones to the etch holes of the devices.

B Calculating wall collision sites

To find wall collision sites in the gap space, we must trace the intersections of the molecule's line of flight with the boundary planes of a box (Fig. 15). If we parametrize this line of flight by the vector representation $\vec{g}(t)$ as a function of time t:

$$\vec{g}(t) = \vec{r}_1 + \vec{v} \cdot t \,, \tag{38}$$

the intersection with a plane determined by normal vector $\vec{n}$ and support $\vec{p}$ is found by requiring:

$$\vec{n} \cdot (\vec{g}(t) - \vec{p}) = 0 \,. \tag{39}$$

Using the function specification of $\vec{g}(t)$ we solve a value of time from this equation. This time value, t_p, denotes the time that the molecule needs to reach the intersection from its starting position $\vec{r}_1$. The regarded intersection $\vec{r}_p$ is now evaluated as:

$$\vec{r}_p = \vec{g}(t_p) \,. \tag{40}$$

Along its trajectory in the box, the molecule passes a whole series of such intersections. Because the calculation of a plane-with-line intersection is direct, we omit the a-priori selection of the collision plane and determine for each new line of flight all intersections with the boundary planes of the box. Of the six intersections $\vec{r}_p[\vec{n}, \vec{p}]_i$ possible the true solution $\vec{r}_{\text{coll}}$ is found by requiring the solution coordinates to be inside the box-shaped enclosure (Fig. 15):

$$\vec{r}_{\text{coll}} = \left\{ \vec{r}_p[\vec{n}, \vec{p}]_i : i = 1, 2, \ldots, 6 \;\middle|\; \begin{array}{l} 0 < x < L_b \\ 0 < y < H_b \\ 0 < z < d \end{array} \right\} \tag{41}$$

Two solutions satisfy this criterion of which the right one remains after rejecting the departure point $\vec{r}_1$.

References

[1] T. Veijola, H. Kuisma, J. Lahdenpera, and T. Ryhanen, Sens. Actuators A **48** (1995) 239-48.

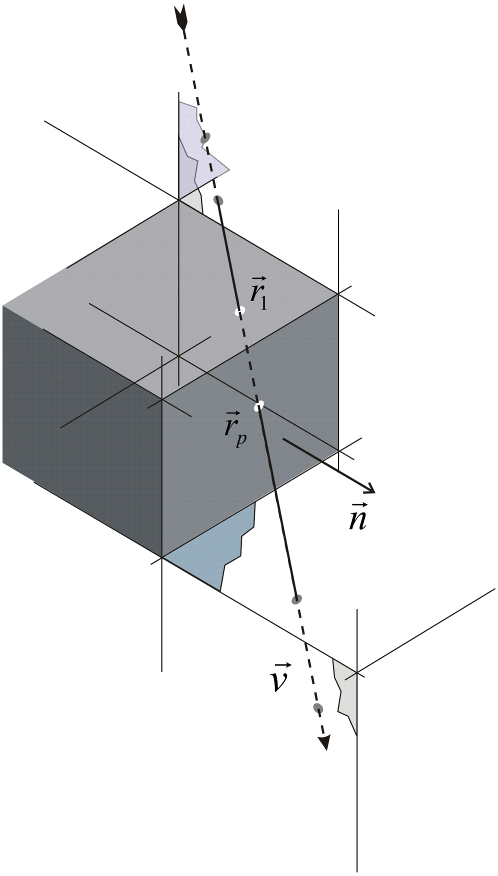

Figure 15: Intersections of a molecule's flight line $\vec{g}(t)$ with the boundary planes of the gap space (shaded box) in our devices. Starting the particle in $\vec{r}_1$ in a direction parallel to $\vec{v}$ during a random walk, we must determine the new position $\vec{r}_p$ on the gap wall.

[2] W. Li, Nanotechnology 10 (1999) 440-446.

[3] A.H. Nayfeh, M.I. Younis, J. Micromech. Microeng. 14 (2004) 170-181.

[4] G.L. Saksaganskii, ”Molecular flow in complex vacuum systems”, Gordon and Breach Science Publishers, 1988.

[5] G. Li and H. Hughes, Proc. SPIE 4176 (2000) 30-46.

[6] W. Newell, Science 161 (1968) 1320-6.

[7] Y. Kawamura, K. Sato, T. Terasawa, and S. Tanaka, Proc. Transducers’87 (1987) 283-286.

[8] Z. Kadar, W. Kindt, A. Bossche, and J. Mollinger, Proc. Transducers’95 (1995) 29-32.

[9] B. Li, H. Wu, C. Zhu, and J. Liu, Sens. Actuators A **77** (1999) 191-194.

[10] H. Sumali, J. Micromech. Microeng. 17 (2007) 2231-2240.

[11] G. Hong, W. Ye, Phys. Fluid. 22 (2010) 012001

[12] M. Bao, H. Yang, H. Yin, Y. Sun, J. Micromech. Microeng. **12** (2002) 341-346.

[13] S. Hutcherson, W. Ye, J Micromech Microeng 14 (2004) 1726-1733

[14] P. Li and Y. Fang, J. Micromech. Microeng. 20 (2010) 035005

[15] R. Leung, H. Cheung, G. Hong, W. Ye, Microfluid. Nanofluid. (2010)

[16] M. K. Andrews, G. C. Turner, P. D. Harris and I. M. Harris, Sens. Actuators A **36** (1993) 219-226

[17] R. Legtenberg and H.A.C. Tilmans, Sens. Actuators A **45** (1994) 57-66.

[18] R.G. Christian, Vacuum **16** (4) (1966) 175-178.

[19] R. Puers, D. Lapadatu, Sens. Actuators A **56** (1996) 203-210.

[20] M. Knudsen, Ann. Physik **28** (1909) 75.

[21] M. von Smoluchowski, Ann. Physik **33** (1910) 1559.

[22] P. Clausing, J. Vac. Sci. Technol. **8** (5), 1971, 636-646.

[23] H. C. W. Beijerinck, M. P. J. M. Stevens, N. F. Verster, Physica 83C (1976) 209-219.

Chapter 4

Residual gas dependency of squeeze-film dynamics of MEMS devices[1]

---

[1] This chapter only serves the purpose of presenting insight in parameters of the design process and as yet lacks a comprehensive reference frame to other information in literature

Abstract

Hermetic packaging is a key issue for many micro-electro-mechanical devices (MEMS). For example, MEMS oscillators require low pressures in the 1 to 100 Pa pressure range for a proper operation without unacceptable damping and/or shifts in operating frequency. A simple gas kinetic analysis reveals that both these effects depend on the composition of the residual gas. We present data for He ($M = 4$), N_2 ($M = 28$) and C_2F_6 ($M = 138$), showing a perfect scaling of the experimentally derived value with the square-root $\sqrt{M}$ of the mass number. The results obtained provide insight in the changes of quality factor Q and resonance frequency ω_0 involving changes of residual gas composition due to leakage into or out-gassing of the microcavity.

1 Introduction

In the previous chapter we compared measurements of the quality factor and resonance frequency of different MEMS resonators to values expected from squeeze-film damping. It was shown that the pressure dependence of the damping b_{squeeze} and stiffness k_{squeeze} force coefficient due to the squeeze film could be very simply related to the random walk escape time of the residual gas molecules. The model built on this discovery is useful to designing resonant pressure sensors and assessing the cavity vacuum of MEMS devices in sample release tests as we will demonstrate in the next chapter.

As the composition of the residual gas is rather hard to determine, either from experiment or from a theoretical prediction of the dynamics of leakage and out-gassing of sealed MEMS cavities, it is essential to study the effect of different gases on the characteristics of the MEMS device. Currently the works of Andrews [1] and Li [2] are the only references in open literature with similar interest. Because the work of Andrews mainly concerns *viscous* flow induced squeeze forces and Li only regards structures subject to molecular *drag* forces, analysis of the matter for *squeeze* force dominated structures with molecular flow fills up a gap in the field. Thus, we extended our experiments for this type of structures to test our model for gases with molecular mass numbers differing from air or nitrogen. The results obtained provide insight in the changes of quality factor Q and resonance frequency ω_0 involving changes of residual gas composition due to leakage into or out-gassing of the microcavity.

Previously we characterized the operation regime of resonators by the product $\omega_0\tau$ of their specific resonance frequency ω_0 and squeeze film escape time τ. Large values $\omega_0\tau \gg 1$ imply a nearly complete containment of the gas film and thus cause the squeeze film to have its main effect on frequency shift. On the other hand, low values $\omega_0\tau \ll 1$ involve a nearly free effusion of the gas molecules and thus cause mainly damping of the resonance amplitude. This behavior is apparent by the parametric representation of the ($b_{\text{squeeze}}(\omega_0\tau)$, $k_{\text{squeeze}}(\omega_0\tau)$) curve in a two-dimensional plot with scaled values of the squeeze force on the major axes (chapter 3). This escape time τ obviously depends on the average distance traveled by the molecules before escape from the film and the average speed of the molecules. Because of this speed dependence the escape time will vary with gas species (molecular mass) and temperature. A scaling law for escape time τ with molecular mass number M, that we verify with the experiment presented in this article, results from considering the random walk characteristics discussed in chapter 2 of this thesis (Sec. 2).

Section 3 describes the experiment and the devices used. Section 4 presents the results and analysis of experimental data. In conclusion we compare the experimental values of τ for the different gases to theory in section 5 and formulate the lessons learned in section 6.

2 Scaling law for average escape time τ

Squeeze-film forces have strong effects on resonance amplitude as well as on resonance frequency shifts of typical micromechanical resonators. We showed these effects result from the combination of an elastic force with coefficient k_{squeeze} and a dissipative force with coefficient b_{squeeze}:

$$\begin{aligned} k_{\text{squeeze}} &= \frac{p_0 A}{d} \frac{(\omega\tau)^2}{1+(\omega\tau)^2} \,, \\ b_{\text{squeeze}} &= \frac{p_0 A}{d} \frac{\tau}{1+(\omega\tau)^2} \,. \end{aligned} \tag{1}$$

The mix of elastic and damping contributions to the squeeze force at certain frequency ω depends on the escape time τ of the gas molecules.

The random walks that averaged over large numbers yield the diffusion behavior of the gas in the squeeze film consist of mutually independent randomly directed straight line passages between the facing walls of the gap. Accordingly the random walk time τ_i of molecule i equals the average passage time τ_p times the number of collisions N_i occurring between departure in and escape from the gap:

$$\tau_i = N_i \tau_p = N_i \left\langle \frac{d}{v_z} \right\rangle \,, \tag{2}$$

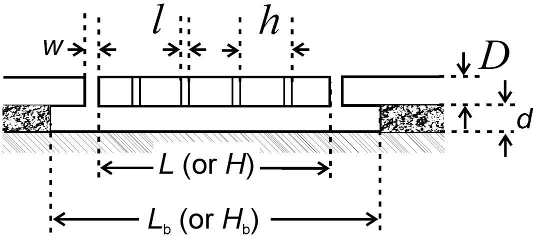

Figure 1: Cross section of SOI resonators investigated.

where d denotes the gap width and v_z the transverse velocity component of the molecule leaving either side of the gap (assuming the z-direction is perpendicular to the gap plane). Using that v_z is randomly distributed according to a *Rayleigh distribution* with parameter $\sqrt{\pi/8}\langle v\rangle$ (Appendix A of chapter 2), we find τ_i is inversely proportional to the average velocity $\langle v\rangle$:

$$\begin{aligned}\tau_p &= \int_0^\infty 2\frac{d}{v_z}\,\frac{v_z}{(\pi/4)\langle v\rangle^2}\,e^{-4v_z^2/(\pi\langle v\rangle^2)}\,\mathrm{d}v_z = \frac{2d}{\langle v\rangle}\\ \tau_i &= 2N_i\,\frac{d}{\langle v\rangle}\end{aligned} \tag{3}$$

According to the well known formula for the average speed of molecules in a gas

$$\langle v\rangle = \sqrt{8k_B\,T/(\pi\,M)}\,, \tag{4}$$

this result establishes the scaling law for average escape time τ with molecular mass number M:

$$\tau \propto \sqrt{M} \tag{5}$$

For two alternative gases with very different molecular mass number M than the usual nitrogen molecule – representative for dry air –, we repeated the experiment of chapter 3 to determine the pressure gradients of the damping b_{squeeze} and stiffness k_{squeeze} force coefficients due to the squeeze films of two different resonators. Given the facilities of our lab, we chose to use helium gas ($M = 4$) as the light weight and hexafluoroethane gas ($M = 138$) as the heavy weight alternative to nitrogen ($M = 28$). Hexafluoroethane (C_2F_6) is a very inert gas commonly used as an etchant in semiconductor manufacturing. Using the construction method of chapter 3

Table 1: Characteristic parameters of the two MEMS devices. Resonance frequency $\omega_{0,\mathrm{mat}}$ and spring constant k_{mat} as calculated from a finite-element simulation using COMSOL.

Property	**Definition**	**Dog bone**	**Square plate**
Gap frame	$L_b \times H_b$ (μm^2)	112×62	172×172
Gap width	d (μm)	1.0	1.0
Unit cell size	$h \times h$ (μm^2)	7.0×7.0	9.0×9.0
Etch hole size	$l \times l$ (μm^2)	0.8×0.8	0.5×0.5
Trench width	w (μm)	0.8	0.2
Plate area A	$L \times H$ (μm^2)	100×50	160×160
Plate thickness	D (μm)	1.5	1.5
Spring length	s (μm)	18	18
Spring width	t (μm)	16	4
Spring constant	k_{mat} (N/m)	54	71
Frequency	$\omega_{0,\mathrm{mat}}/2\pi$ (kHz)	228	137

we derived the species dependent values $[\omega_0\tau]_{\mathrm{expt}}$ per device. In accordance with the previously derived scaling law, we find the average escape time τ to be proportional with the square root of molecular mass M. The found mass dependence of the diffusion time establishes a mechanism to identify gas species in resonant pressure sensors and supports the assumption of full accommodation of molecule-wall collisions in the resonator gaps as discussed in chapter 2.

3 Experiment

Two different resonator samples are produced on a Silicon-On-Insulator (SOI) substrate using surface micro-machining. Contours of the structures are patterned onto the substrate and etched through the top silicon layer, cutting out the resonator features. To facilitate the wet etch of the 1.0 μm intermediate oxide layer, all plates and wide beams are perforated with $l \times l$ sized holes in a $h \times h$ spaced grid. Thus a free-standing structure results, with a gap distance to the substrate $d = 1.0$ μm (Fig. 1). The devices are labeled ’Dog bone’ and ’Square plate’ referring to their geometrical layout and operated in out-of-plane resonant modes subjected to squeeze-film damping in the gap between resonator and substrate (Fig. 2). Characteristic dimensions and properties are given in Tab. 1.

For different values of the residual gas pressure, ranging from 0.1 to 1.2 mbar, the electrical transmission signals of the respective devices were measured as a function of the generator frequency ω. Therefore we mounted the devices in a vacuum chamber with a base pressure less than 1×10^{-5} mbar. Through a needle valve we vented the chamber with either one of the gases to achieve the desired pressure. The pressure was measured with an MKS Baratron 627B capacitance manometer with an accuracy of 0.1%.

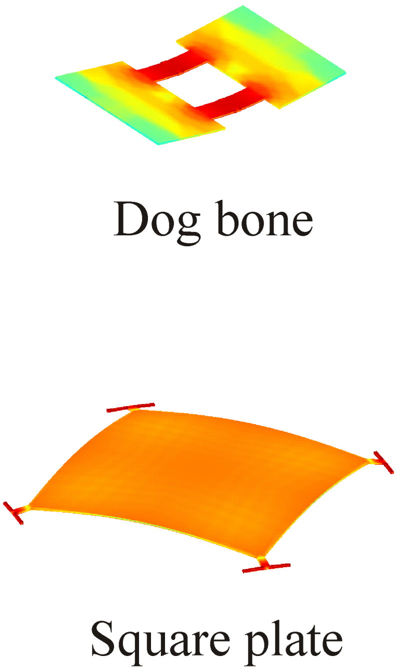

Figure 2: Mode shapes and strain energy volume distribution of the resonator structures investigated.

The electrical readout of the amplitude of the oscillating plate is straightforward. The microstructure in the top silicon substrate layer and the substrate form a variable capacitor. Microstructure motion was detected via capacitance changes measured using an HP4194A impedance analyzer. At resonance, the plate amplitude rises and more mechanical energy is dissipated in the ambient gas. Since this dissipated energy must be supplied by the analyzer, a peak is seen in the magnitude of the admittance $|Y|$. This admittance magnitude directly links to the mechanical behavior of the microstructure as a result of electrostatic coupling.

4 Experimental results

The measured frequency response of the admittance $|Y|$ is plotted in Fig. 3. We clearly see the decrease of the quality factor with increasing pressure accompanied by a significant shift of the resonance frequency as predicted by theory. We determined quality factors Q and resonance frequencies ω_0 with a least-squares curve fit to a Lorentzian peak function H:

$$H(\omega) = H_0 \Bigg/ \sqrt{4\left(\frac{\omega}{\omega_0} - 1\right)^2 + \frac{1}{Q^2}} \qquad (6)$$

Here, H_0, ω_0 and Q are mutually independent curve-fitting parameters. We clearly see the decrease of the quality factor with increasing pressure and observe also a significant shift of the resonance frequency as expected from theory.

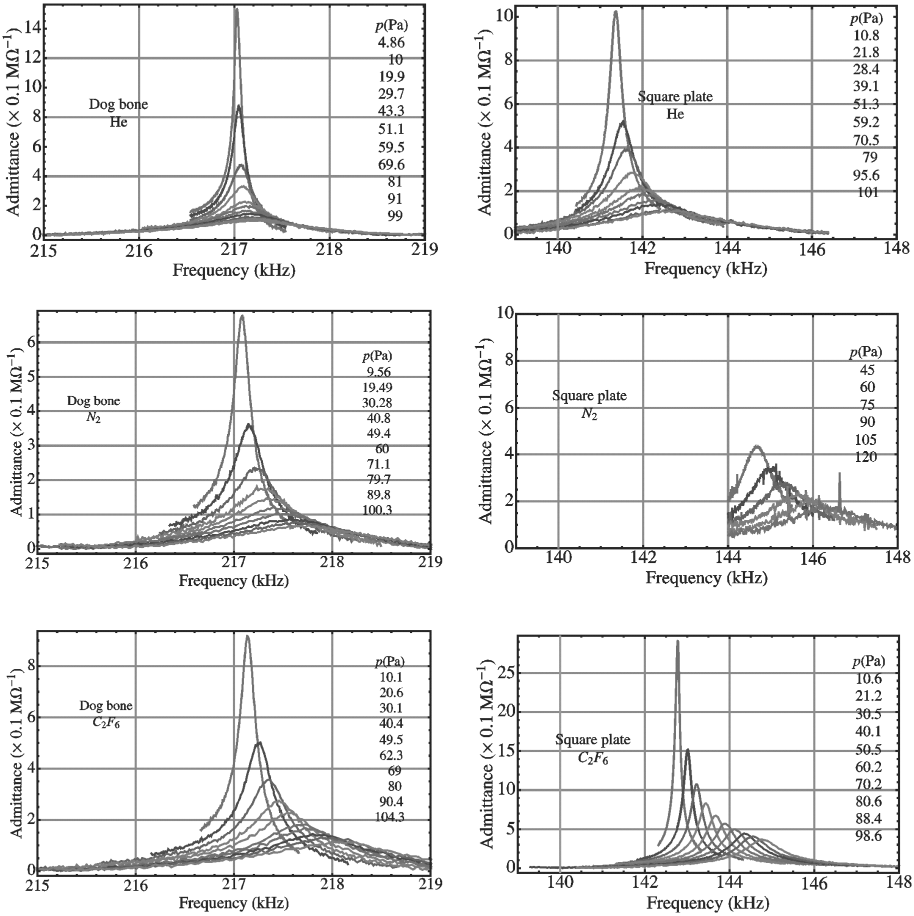

Figure 3: Electrical transmission signals of the capacitively measured resonator devices for the different gases (helium He, nitrogen N_2 and hexafluoroethane C_2F_6) in this experiment. In the legend the gas pressures corresponding to the successively shrinking peaks are listed. Please note the low pressure observations of the 'Square plate' are left out because of an accidental bias voltage setting that obscures the pressure dependence of the resonances.

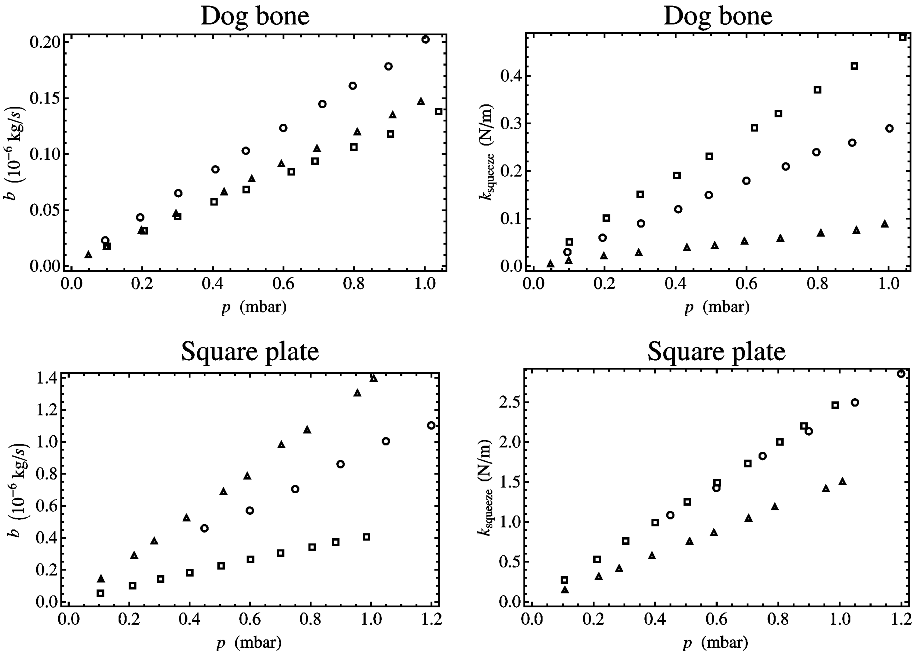

Figure 4: Experimental results of damping and elastic coefficients, b, k_{squeeze} as a function of gas pressure for the investigated resonators. The symbols refer to the different gases as follows: △ helium, ○ nitrogen, □ hexafluoroethane.

In Fig. 4 we show the experimental results for the damping b as a function of the gas pressure in the test chamber at ambient temperature $T = 22$ °C. Here, clear linear pressure dependencies turn up according to prediction. We calculate the damping coefficients b, using the relation $b = k_{\mathrm{mat}}/(\omega_{0,\mathrm{mat}}\, Q)$ with k_{mat} the simulated stiffness of the microstructure in the excited resonance mode which is listed in Tab. 1.

Also we show the experimental results for the stiffness contribution k_{squeeze} due to ambient pressure. Again, we discover prominent linear dependences on pressure via straight-line fits of the data. The stiffness contribution $k_{\mathrm{squeeze}}(p)$ is calculated from the observed resonance frequencies $\omega_0(p)$ using the relation

$$k_{\mathrm{squeeze}}(p) = m_{\mathrm{eff}} \left([\omega_0(p)]^2 - \lim_{p \to 0} [\omega_0(p)]^2 \right) , \tag{7}$$

where the effective mass $m_{\mathrm{eff}} = k_{\mathrm{mat}}/\omega_{0,\,\mathrm{mat}}^2$ results from the finite-element simulation as listed in Tab. 1. The experimental value for the undisturbed resonance frequency $\lim_{p \to 0} \omega_0(p)$ is given in Tab. 2. The observed discrepancy with the simulated value of ω_0 of about 5% is attributed to the omission of the etch holes in our FEM simulation. Also, the difference between the nominal plate thickness $D = 1.5$ μm used for the simulation and the thickness on the wafer of the actual device – due to the process spread in the production – contributes to this error.

The slope of straight-line curve-fits to the experimental data of b and k_{squeeze} gives the pressure sensitivity, denoted by

$$\begin{aligned} \frac{\mathrm{d}}{\mathrm{d}p} b &\equiv \beta \\ \frac{\mathrm{d}}{\mathrm{d}p} k_{\mathrm{squeeze}} &\equiv \kappa . \end{aligned} \tag{8}$$

In reality the pressure sensitivity β results from squeeze film forces as well as drag forces by kinetic damping. This type of damping merely scales with the frontal area-to-molecular speed ratio $\sim A/\langle v \rangle$ which is in typical gaps largely exceeded by the $\sim A/(\omega_0\, d)$ scaling of squeeze film damping. For the regarded devices in this study the kinetic damping amounts to less than 3% of the squeeze film contribution. Considering the assumed approximations made in our model of several percent we can rightly neglect the kinetic damping contribution to β in our analysis. The values of the experimental observations β_{expt} and κ_{expt} are given in Tab. 2, together with model predictions based on our model. We observe a good agreement, which shows that the scaling behavior of the model with residual gas species is rather satisfactory.

For each experimental observation $(\beta_{\mathrm{expt}}, \kappa_{\mathrm{expt}})$ defined by device and gas type we determine the value of $[\omega_0 \tau]_{\mathrm{expt}}$ by employing our projection method of chapter 3.

Table 2: Summary of experimental results for the pressure dependency β for damping and κ for the elastic constant. The scaled values are compared to the predictions of the model of Eq.(1), using Monte Carlo values of τ (reported as $\omega_0\tau$ product) as input. The scaled values are used to calculate an experimental value for ϕ and $[\omega_0\tau]_{\mathrm{expt}}$. Within experimental error we observe a good agreement with the results of the model. Numbers in parentheses indicate the error in the last digit.

	Dog bone			**Square plate**		
Parameter	He	N_2	C_2F_6	He	N_2	C_2F_6
$\omega_{0,\mathrm{expt}}/2\pi$ (kHz)	217.0	217.1	217.1	141.4	144.6	142.8
β_{expt} (10^{-6} kg/s mbar^{-1})	0.14(1)	0.20(1)	0.13(1)	1.39(6)	0.89(4)	0.40(2)
κ_{expt} (N/m mbar^{-1})	0.087(5)	0.30(2)	0.47(2)	1.45(8)	2.21(4)	2.37(5)
β^*_{expt}	0.41(2)	0.54(3)	0.33(1)	0.47(2)	0.30(2)	0.13(1)
β^*	0.39	0.48	0.31	0.50	0.32	0.15
κ^*_{expt}	0.17(1)	0.61(3)	0.95(5)	0.57(3)	0.86(2)	0.92(2)
κ^*	0.19	0.62	0.89	0.55	0.89	0.98
ϕ_{expt} (°)	-38(2)	12(2)	54(5)	8(2)	51(2)	72(4)
ϕ (°)	-38	14	51	5	51	73
$[\omega_0\tau]_{\mathrm{expt}}$	0.48(2)	1.23(4)	3.0(4)	1.15(3)	2.8(1)	6.5 ± 1.1
$\omega_0\tau$	0.48	1.3	2.9	1.1	2.8	6.3

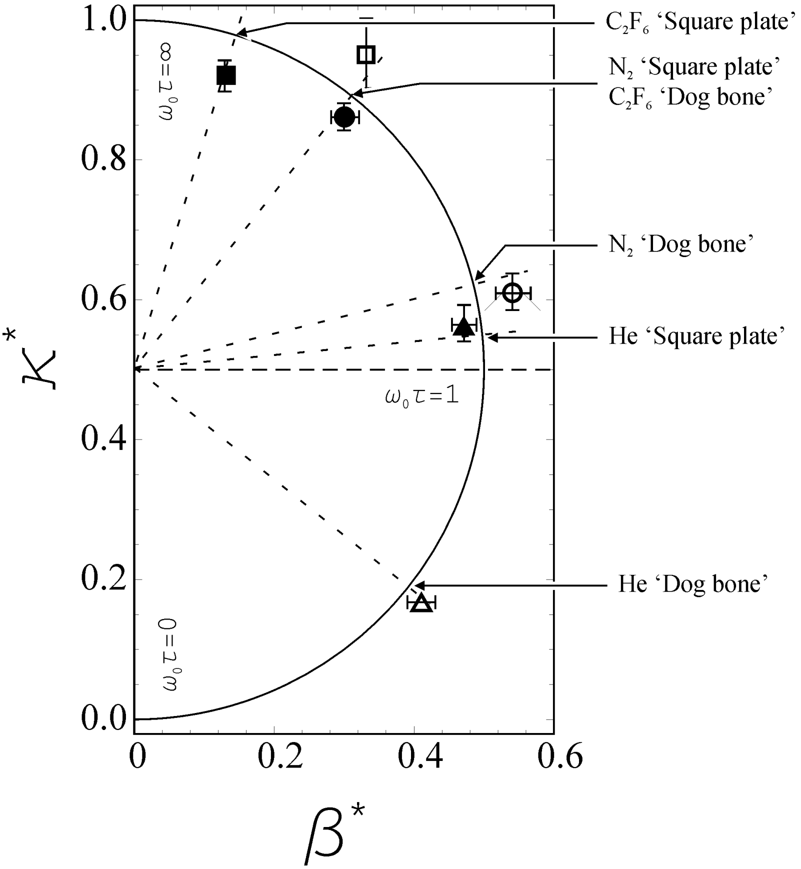

Figure 5: Result of (β^*, κ^*)-analysis for the devices investigated. The symbols refer to the different gases as follows: △ helium, ○ nitrogen, □ hexafluoroethane. Open symbols denote the 'Dog bone' and filled symbols the 'Square plate' device, respectively. The intersections of the three dashed rays with the curve indicate the (β^*, κ^*) model prediction of each observation.

The appropriate projection is found using the locus (β, κ; t) of our model. Figure 5 shows the parametric curve $l(t)$ and the construction of it for our experiment when $t = [\omega_0\tau]$.

$$l(t) \equiv \begin{pmatrix}\beta^* \\ \kappa^*\end{pmatrix} = \frac{t}{1+t^2}\begin{pmatrix}1 \\ t\end{pmatrix}, \tag{9}$$

in which t runs through values of $\omega_0\tau \in [0; \infty]$. The orthogonal coordinates β^* and κ^* of the curve represent the normalized sensitivities of damping and stiffness to pressure p:

$$\begin{aligned}\beta^* &= \frac{\omega_0\, d}{A}\beta \\ \kappa^* &= \frac{d}{A}\kappa\end{aligned} \tag{10}$$

We see that $l(t)$ defines a *semi-circle* in the (β^*, κ^*)-plane, centered at (0, $\frac{1}{2}$), with radius $\frac{1}{2}$. At the origin (0, 0), the value of $\omega_0\tau$ is zero; halfway up the curve, in ($\frac{1}{2}$, $\frac{1}{2}$), we find $\omega_0\tau = 1$ and at the end, in (0, 1), the value of $\omega_0\tau$ goes to infinity.

Following the analysis introduced in chapter 3, we can derive that the error $\Delta(\omega_0\tau)$ in the operation point $\omega_0\tau$ due to error bars $\Delta\beta^*$ and $\Delta\kappa^*$ is determined by:

$$\Delta(\omega_0\tau) = \left(\frac{1+\sin\phi}{\cos^2\phi}\right)\Delta\phi, \tag{11}$$

with the polar angle ϕ defined by

$$\phi = \arctan\left(\frac{\kappa^* - \frac{1}{2}}{\beta^*}\right), \tag{12}$$

and the error $\Delta\phi$ defined as

$$\Delta\phi = \max\left[\frac{2\,\Delta\beta^*}{|\sin\phi|}, \frac{2\,\Delta\kappa^*}{\cos\phi}\right]. \tag{13}$$

In Tab. 2 we summarize the experimental results for β^*_{expt} and κ^*_{expt}, together with the resulting value for the polar angle ϕ_{expt} and the characteristic parameter $[\omega_0\tau]_{\text{expt}}$. Figure 5 shows the result of the analysis of our three devices graphically. The graph clearly illustrates the difference in operation point, not only between distinct resonators but also between the three different gases.

Table 3: Experimental and simulated ratios of $\omega_0\tau$ values according to Eq. (15) for the two devices investigated. Numbers in parentheses indicate the error in the last digit.

$\frac{[\omega_0\tau]_{\texttt{<gas>}}}{[\omega_0\tau]_{N_2}}$	`<gas>`		
	He	N_2	C_2F_6
Dog bone	0.39(2)	1.00	2.4(3)
Square plate	0.41(2)	1.00	2.3(4)
$\sqrt{M_{\texttt{<gas>}}/M_{N_2}}$	0.378	1.00	2.220
Simulated	0.378	1.00	2.220

5 Experimental $\omega_0\tau$ value

We now have to face the challenge of extracting a reliable value of $\omega_0\tau$ from the experimental data. A comparison of this value to the Monte Carlo value helps us to investigate the scaling of the results with the residual gas composition. Taking nitrogen as reference and changing the τ variable back to $\omega_0\tau$, we have

$$\tau_{He} : \tau_{N_2} : \tau_{C_2F_6} = \sqrt{M_{He}} : \sqrt{M_{N_2}} : \sqrt{M_{C_2F_6}} \,, \tag{14}$$

$$\frac{[\omega_0\tau]_{He}}{[\omega_0\tau]_{N_2}} : 1 : \frac{[\omega_0\tau]_{C_2F_6}}{[\omega_0\tau]_{N_2}} = \sqrt{\frac{M_{He}}{M_{N_2}}} : 1 : \sqrt{\frac{M_{C_2F_6}}{M_{N_2}}} \,. \tag{15}$$

Calculation brings the results stated in Tab. 3. The error values are obtained by a standard error propagation calculation from Tab. 2. We can see that the experimental values for the characteristic parameter $\omega_0\tau$ are actually consistent with the scaling law of Sec. 2. We observe a perfect scaling according to Eq. (15). Moreover the results for our Monte Carlo simulated escape time values match equally well to this pattern.

6 Concluding remarks

We extended the squeeze-film damping experiments on MEMS resonators of chapter 3 to different gases. The random walk diffusion time of the residual gas molecules introduced in this chapter determines the pressure dependence of resonance frequency and quality factor. The speed dependence of the diffusion time establishes a mechanism to identify gas species in resonant pressure sensors. In accordance with elementary kinetic theory, we find the average molecular speed $\langle v \rangle$ to be inversely proportional with the square root of molecular mass M, which supports the assumption of full accommodation of molecule-wall collisions in the resonator gaps.

References

[1] M.K. Andrews. P.D. Harris, Sens. Actuators A **49** (1995) 103-108.

[2] Q. Li, J.F.L. Goosen, F. van Keulen, J.T.M. van Beek, IEEE Sensors 2009, 1040-1043.

[3] M.A.G. Suijlen, J.J. Koning, M.A.J. van Gils, H.C.W. Beijerinck, Sens. Actuators A **156** (2009) 171-179. (chapter 2 of thesis)

Chapter 5

Dual-mode device for in-situ testing of MEMS packaging quality

Abstract

A method is presented to rapidly characterize the hermeticity of a vacuum cavity for a 56 MHz MEMS in-plane mode 'dog-bone' resonator. The method relies on operating the device in a 2.5 MHz out-of-plane resonance mode. By monitoring the Q-factor and resonance frequency shift of this out-of-plane mode, the pressure change inside the cavity can be measured with a sensitivity that is 100 to 1000 times higher than when using the in-plane mode. This high sensitivity pressure sensing is vital for estimating the life-time of vacuum packaged resonators within a limited test-time.

Our squeeze-film damping model and the classical predictions for kinetic damping and drag forces based on gas kinetic theory describe the experimental results well, i.e. within the experimental error of 15% for Q and 3% for $\Delta\omega_0$. For this purpose the model has been extended to include the effect of coupled squeeze-film boxes, which can be expressed in terms of an effective gap height and an effective escape time.

1 Introduction

Hermetic packaging is a key issue for many micro-electronical and micro-electromechanical systems (MEMS). By sealing microsystems from harmful environmental influences, mainly moisture, the reliability and lifetime can be significantly increased. Some MEMS need a specific gas atmosphere or pressure within the package for proper function and satisfactory performance. Therefore life-time testing of cavity pressure levels is very important to conclude about the reliability of the device.

For this job, the method of standard leak detection is rather insensitive and cannot be used with the extremely small size of wafer-level packages typical for state-of-the-art MEMS [1, 2]. Instead miniaturized absolute pressure sensors may be integrated for *in-situ* testing of the cavity vacuum. Waelti et al. [1] and Mailly et al. [3] for example present some solutions with dedicated sensors in the package based on measurement of the thermal conductivity of the residual gas. At the millibar range vacuum pressures in typical cavities, this conductivity is directly proportional to the gas density which enables measurement of absolute pressure. These wafer-level Pirani-type pressure sensors exist in many geometrical and read-out implementations. Corresponding measurement sensitivities and ranges of linearity can be adapted with great freedom. See for example Li et al. [4] for a state-of-the-art sensor design.

For MEMS applications relying on the resonant motion of a micromechanical element such as MEMS filters, gyroscopes or oscillators, cavity pressure testing however could be done without dedicated sensing structures. Anyway the momentum transfer of gas molecules gives the resonator Q-factor and frequency ω_0 a principal sensitivity to pressure. A suitable design is all what is needed to obtain usable sensitivity in the

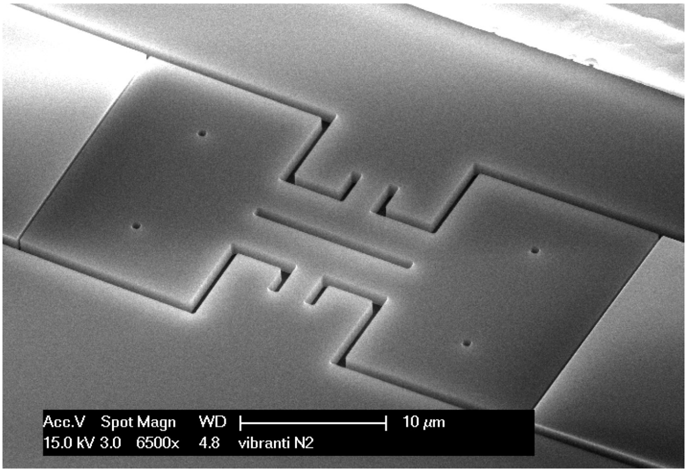

Figure 1: SEM picture of dog-bone shaped resonator for high frequency timing purposes processed in silicon-on-insulator (SOI). This structure is intended to perform high frequency in-plane resonant oscillation.

measurement range. In the ideal case, a read-out of the common characteristics in resonant operation (quality factor and resonance frequency) of the resonator sample should be sufficient to measure the absolute cavity pressure without any additional structures and signal conversion! In search of a diagnostic for life-time testing of a surface-micromachined capped bulk mode resonator (Fig. 1) developed for a 56 MHz MEMS oscillator [5], we discovered from measurements that the device operated in the low-stiffness out-of-plane mode exhibits such high pressure sensitivity that the suggested in-situ testing is a real option.

Van der Wel et al. [6] already proved the practical use of this idea to perform hermeticity testing in an RF MEMS capacitive switch. They used the calibration result of Q-factor vs. pressure to measure hermeticity loss of the devices during a number of standard reliability tests. Although effective for a single device design, this approach can become problematic if devices must be tested concerning a number of versions with different feature sizes. The spread of designs in industrial manufacturing due to inherent process spreads is particularly related to this aspect. Explicit pressure calibration will take time and values of pressure sensitivities for every version designed need to be available without measurements. The solution is to calculate sensitivities and for this activity modeling and simulation of the interaction between gas and resonator structure play a major role.

The narrow gaps of resonators cause a strong coupling of microstructure movement with the flow of residual gas and the emerging *squeeze-film* forces turn out to be the determining gas-structure interaction in typical resonators. Quantitative prediction of the gas flow and resulting forces involves generally a highly specialistic programming effort in existing *squeeze-film* models and this seriously complicates proper design activities. Therefore we developed a new, semi-analytical model that can live up to the standards of efficient designing.

By comparing the pressure sensitivities in standard and alternative resonance mode of the referred 56 MHz resonator obtained from measurement and calculation, this article explains the multifunctional use of the microstructure for in-situ testing of MEMS packaging quality. Key is the calculation according to our squeeze-film damping model and Christian's model [7] for kinetic damping that provides great insight to all damping contributions of our device and the result of which excellently agrees to the experimental observation. Clear directions can now be given on the design of microstructures in general that should also perform pressure testing by their motion.

In the next section we explain the device construction and specify its main properties. Section 3 treats the sensitivity of the device to ambient pressure with regard to quality factor and frequency. Sections 4 and 5 demonstrate the methodical damping calculation using the two expressions that describe squeeze film forces and the two expressions that determine kinetic damping. Section 6 describes the experiment to measure the pressure dependence of the in-plane mode used for the high frequency oscillator function. Section 7 treats measuring the out-of-plane mode for pressure sensing and concludes about the agreement between experiment and our predictions. Finally, in Sec. 8, we present some concluding remarks on the lessons learned.

2 Dog-bone resonator

The device is a dog-bone shaped resonator for high frequency timing purposes and is processed on a silicon-on-insulator (SOI) wafer. The resonator is reactive-ion etched into a 1.5 µm thick, *n*-type, SOI layer down to the buried oxide layer. Next, the resonator is released by isotropic etching of the buried oxide layer with HF vapor. Using a nitride layer the device is at the end provided with a thin-film encapsulation as shown in Fig. 2. The dimensions of the 'dog-bone' resonator device are listed in Tab. 1.

2.1 In-plane mode

By means of in-plane electrodes opposite to the lumped mass heads, the resonator is operated in its fundamental extensional eigenmode at $\omega_0/(2\pi) = 56$ MHz. With

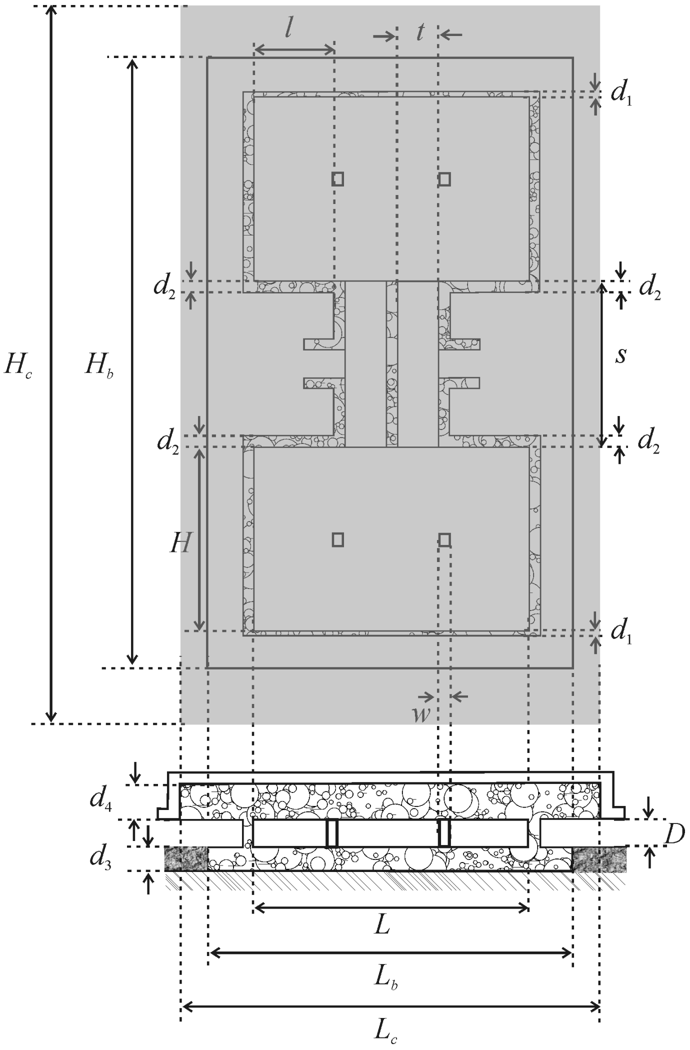

Figure 2: Top and cross sectional view of the resonator structure considered in this study. In a schematic way we have indicated the etch box with dimensions $H_b \times L_b \times d_b$ and the capping volume with dimensions $H_c \times L_c \times d_c$ with $d_b = d_3$ and $d_c = d_4$. Please note that the dimensions (L_b, H_b) of the box and (L_c, H_c) of the cap are not to scale as compared to the dimensions (L, H) of the plate.

Table 1: Main properties of the dog-bone resonator. The stiffness and the resonance frequency of the two eigen-modes was calculated by a FEM simulation in COMSOL. The value of the quality factor is determined from experiments, with the number between parentheses indicating the error in the last digit.

Source	**Property**	**Definition**	**Value**	
Design	Plate length	L (µm)	20	
	Plate width	H (µm)	13.4	
	Plate thickness	D (µm)	1.5	
	Spring length	s (µm)	12	
	Spring width	t (µm)	3.0	
	Box frame	$L_b \times H_b$ (µm^2)	34×52	
	Cap frame	$L_c \times H_c$ (µm^2)	60×100	
	Etch holes	$w \times w$ (µm^2)	0.6×0.6	
			In-plane	**Out-of-plane**
COMSOL	Stiffness	k_{mat} (N/m)	$204 \cdot 10^3$	530
	Frequency	$\omega_0/2\pi$ (MHz)	56.0	2.51
Experimental	Quality factor	Q_{mat} (10^3)	32.8(3)	17.4(9)

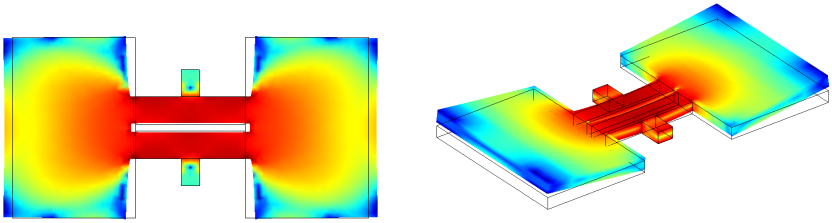

Figure 3: Display of (exaggerated) deformation and strain energy distribution of both in-plane (top) and out-of-plane mode (bottom) of the resonator investigated.

finite-element (FEM) simulations using *COMSOL Multiphysics*[1], we determined the effective stiffness k_{mat} of the structure in the fundamental in-plane eigenmode. For this, the mode shape with corresponding strain energy distribution was simulated (Fig. 3). Because the microstructure is actuated by a uniform force distribution, the effective stiffness k_{mat} satisfies

$$U = \frac{1}{2} k_{\mathrm{mat}}\, x_{cm}^2, \tag{1}$$

with x_{cm} the domain averaged in-plane extension of the microstructure and U the total amount of elastic energy stored in the simulated shape. The value of U is found by integrating the strain energy distribution over the microstructure volume. All the strain energy is stored in the narrow springs that connect the plates to the support structure in the middle. The value of x_{cm} is found from a volume integration of the local in-plane displacement $x(\mathbf{r})$ over the microstructure domain C, as given by

$$x_{cm} = \int_C x(\mathbf{r}) d^3\mathbf{r} \bigg/ \int_C d^3\mathbf{r}. \tag{2}$$

The resulting value of the stiffness k_{mat} is given in Table 1, together with resonance frequency ω_0 as follows directly from the COMSOL simulation. For an easy comparison of the performance of the two modes, we also give the experimental value of the quality factor Q_{mat} for the in-plane mode in this table.

2.2 Out-of-plane mode

For the out-of-plane mode of operation we have chosen the 'butterfly' mode of the device, which follows second to the fundamental 'see-saw' mode as shown by COMSOL FEM simulations. The amount of elastic energy U is again calculated by integrating the strain energy distribution over the microstructure volume. The effective value of the stiffness is calculated by applying Eqs. (1) and (2), however, with two modifications. First, we have to interchange the in-plane x-coordinate for the out-of-plane z-coordinate. Second, we have to change the integration volume in (2). In this mode, the out-of-plane displacement of the butterfly wings by far exceeds the displacement of the springs, which just act as a flexible connection to the support. For the description of the interaction with the gas in the squeeze-film box under the wings, a correct value for the average displacement of the wings is most important: the springs hardly contribute to damping or frequency shifts of the device. The integration volume C of the whole microstructure is replaced by the volume C_p of the wings in both numerator and denominator. The resulting value of the stiffness k_{mat} is

---

[1] Version 3.4 by COMSOL AB, Sweden

given in Tab. 1. Again, we also give the experimental value of the quality factor Q_{mat} for the out-of-plane mode in this table.

We observe that the resonance frequency approximately scales as $\omega_{0,\mathrm{in}}/\omega_{0,\mathrm{out}} \approx \sqrt{k^{\mathrm{in}}_{\mathrm{mat}}/k^{\mathrm{out}}_{\mathrm{mat}}}$ as expected, with a slight difference – 22.3 versus 19.6 – due to the different role of the anchor in the two modes. The super/subscript 'in' and 'out' refer to the in-plane and out-of-plane mode respectively. The quality factor for both modes is on the same order of magnitude, which allows for measurements of damping and frequency shift with comparable accuracy and an easy comparison of the experimental results.

3 Sensitivity to ambient pressure

The in-plane and out-of-plane modes of the 'dog-bone' resonator have a totally different dependency on the pressure of the ambient gas. The sensitivity of the operational characteristics can easily be assessed using our model for squeeze-film forces. The dependency on pressure of the damping coefficient b_{squeeze} and the elastic constant k_{squeeze} is given by

$$\frac{\mathrm{d}k_{\mathrm{squeeze}}}{\mathrm{d}p} = \kappa_{\mathrm{squeeze}} = \frac{A}{d}\,\frac{(\omega_0\tau)^2}{1+(\omega_0\tau)^2}\,, \tag{3}$$

$$\frac{\mathrm{d}b_{\mathrm{squeeze}}}{\mathrm{d}p} = \beta_{\mathrm{squeeze}} = \frac{A}{d}\,\frac{\tau}{1+(\omega_0\tau)^2}\,. \tag{4}$$

Here, p is the ambient pressure and A and d are the area and the height of the gap acting as a squeeze-film box, respectively. The parameter τ is the average value of the escape time of gas molecules from the squeeze-film box. The value of τ depends on the geometry of the device including etch holes, the specific design of the trenches and the dimensions of the gap frame. Using a Monte Carlo simulation, the value of τ can be calculated with simple and flexible routines.

In Tab. 2 we give the relevant parameters for both modes, to assess their pressure sensitivity. For both modes, the value of $A_i/d_i \approx 2\cdot 10^2$ µm is on the same order of magnitude. Because in both cases also $\omega_0\tau_i \geq 1$ this implies that the elastic constant k_{squeeze} and the pressure sensitivity $\kappa_{\mathrm{squeeze}}$ are approximately equal for both modes of operation. This observation – incorrectly – suggests that measuring frequency shifts of the out-of-plane mode does not have an advantage for early detection of an increasing pressure in the capped device, as relevant for detecting leaks and predicting a mean time before failure of the MEMS resonator. The relative frequency shift

Table 2: Dimensions of the dog-bone resonator as relevant for the calculation of the damping of the two modes according to Eqs. (3), (4) and (16). The escape times τ_i with $i = 1, 2, 3, 4, b, c$ were calculated with a Monte Carlo simulation as described in chapter 3. The effective values d_{eff} and τ_{eff} are defined in Eqs. (10) and (12) for the box-cap and plate-box (cap) coupled systems, respectively.

Parameter	**Definition**	**In-plane mode**	**Out-of-plane mode**
Electrode			
Trench area (electrode)	$A_1 = D \times L$ (µm^2)	30	
Trench width (electrode)	d_1 (µm)	0.25	
Escape time electrode	τ_1 (ns)	7.98	
	$\omega_0 \tau_1$	2.81	
Anchor			
Trench area (anchor)	$A_2 = D \times l^a$ (µm^2)	8.7	
Trench width (anchor)	d_2 (µm)	0.80	
Escape time anchor	τ_2 (ns)	7.90	
	$\omega_0 \tau_2$	2.78	
Box			
Box height	$d_b = d_3$ (µm)		1.0
Box area	$A_b = L_b \times H_b$ (µm^2)		1768
Escape time box	τ_b (ns)		361
	$\omega_0 \tau_b$		5.69
Cap			
Cap height	$d_c = d_4$ (µm)		1.5
Cap area	$A_c = L_c \times H_c$ (µm^2)		6000
Escape time cap	τ_c (ns)		469
	$\omega_0 \tau_c$		7.40
Box-cap coupling (slow)			
Effective gap height	$d_{b \leftrightarrow c}$ (µm)		0.6
Effective escape time	$\tau_{b \leftrightarrow c}$ (ns)		204
	$\omega_0 \tau_{b \leftrightarrow c}$		3.22
Plate-box and plate-cap coupling (fast)			
Plate area	$A_3 = A_4 = L \times H$ (µm^2)		268
Escape time plate (box)	τ_3 (ns)		59
	$\omega_0 \tau_3$		0.927
Escape time plate (cap)	τ_4 (ns)		40
	$\omega_0 \tau_4$		0.628

---

[a] $l = L/2 - t - 3\,d_2/2$

$\Delta\omega_0/\omega_0$ scales as (see also Eq.(21))

$$\frac{\Delta\omega_0}{\omega_0} = \frac{\Delta k}{2k_{\mathrm{mat}}}, \tag{5}$$

which is a factor $(k_{\mathrm{mat}}^{\mathrm{out}}/k_{\mathrm{mat}}^{\mathrm{in}})^{-1} = 385$ larger for the out-of-plane mode. For the absolute value of the frequency shift, which scales as $\Delta\omega_0 \sim k_{\mathrm{mat}}^{-1/2}$, this again results in a much larger value for the out-of-plane mode by a factor $(k_{\mathrm{mat}}^{\mathrm{out}}/k_{\mathrm{mat}}^{\mathrm{in}})^{-1/2} = 19.6$. This is excellent news for the experimental accessibility of the frequency of the out-of-plane mode as a diagnostic parameter for pressure increases due to leaks in the capping.

Looking at the damping coefficient b_{squeeze} and its pressure sensitivity β_{squeeze}, the situation is very different. Here, the resulting value is proportional to the time constant τ_i. The ratio $\tau_{\mathrm{out}}/\tau_{\mathrm{in}} \approx 10$ to 20, resulting in an appreciable gain in sensitivity to an increase in pressure for the out-of-plane mode. Here, again, the large difference in k_{mat} values for the two modes plays a beneficial role. An approximate scaling of the characteristic pressure p_β where the quality factor starts to decrease is given by (see also Eq. (25))

$$p_\beta \sim k_{\mathrm{mat}}^{1/2}/\beta_{\mathrm{squeeze}}, \tag{6}$$

which again gives the out-of-plane mode a large advantage over the in-plane mode for early diagnostic applications by a factor $p_\beta^{\mathrm{out}}/p_\beta^{\mathrm{in}} = 1/200$ to 1/400. By using the out-of-plane mode as diagnostic, effects normally visible after ten years become visible in a month's period!

4 Model for coupled squeeze-film boxes

We now have to investigate how the simple formulas of our squeeze film damping model (Eqs. (3), (4)) for a single gap have to be modified to predict in detail the behavior of the two modes. In both cases we have coupled systems of two gaps. Especially for the out-of-plane mode the coupling is rather interesting: the gas in the squeeze-film box below the device, flows directly into the volume between device and cap which effectively also acts as a squeeze-film box with a different gap height. We also have to include the effect of kinetic damping in our discussion. Due to the rather unusual squeeze-film box of the electrode gap in the out-of-plane mode, the contribution of kinetic damping can be comparable to the contribution of squeeze film damping.

4.1 In-plane mode

For the in-plane mode the two trenches that cause the squeeze-film damping act as independent sources of damping and an increase in elastic constant. The flow of gas into and out of the two trenches are uncoupled in first order, because the volumes V_b and V_c – through which they communicate – are both much larger than the trench volumes $V_1 = A_1\, d_1$ and $V_2 = A_2\, d_2$. The contributions of both trenches just add up to

$$\begin{aligned} \kappa^{\text{in}}_{\text{squeeze}} &= 2\, \kappa_{\text{squeeze}}(A_1, d_1, \tau_1) + 4\, \kappa_{\text{squeeze}}(A_2, d_2, \omega_0\tau_2) \\ \beta^{\text{in}}_{\text{squeeze}} &= 2\beta_{\text{squeeze}}(A_1, d_1, \tau_1) + 4\beta_{\text{squeeze}}(A_2, d_2, \omega_0\tau_2)\ . \end{aligned} \tag{7}$$

For the contribution of kinetic damping we find

$$\beta^{\text{in}}_{\text{kin}} = \beta_{\text{kin}}(A_1) + 2\beta_{\text{kin}}(A_2) \tag{8}$$

where we have taken into account the two-sided effect of β_{kin} in Eq.(16).

4.2 Out-of-plane mode

In response to a squeeze action of the resonator, the number densities n_b and n_c of the etch box and the capping volume (Fig. 2), respectively, will swing from their equilibrium value n_0. Numerous molecules will escape and reenter either volume, establishing a net flow of molecules between the etch box and the capping volume that restores the initial equilibrium. This flow will consist of contributions from both volumes, proportional to the corresponding differences ('$n_b - n_0$' or '$n_c - n_0$') in density.

In appendix A we show that in the case of two coupled squeeze-film boxes the results of Eqs. (3) and (4) are valid when we use effective values for the gap height and the time constant, respectively, resulting in

$$\begin{aligned} \kappa_{\text{squeeze}} &= \frac{A}{d_{\text{eff}}}\, \frac{(\omega_0\tau_{\text{eff}})^2}{1 + (\omega_0\tau_{\text{eff}})^2}\ , \\ \beta_{\text{squeeze}} &= \frac{A}{d_{\text{eff}}}\, \frac{\tau_{\text{eff}}}{1 + (\omega_0\tau_{\text{eff}})^2}. \end{aligned} \tag{9}$$

For the coupled systems of the etch box and the cap, the effective values are given by

$$\begin{aligned} \frac{1}{d_{\text{eff}}} &= \frac{1}{d_{b\leftrightarrow c}} = \left(\frac{A_3}{A_b}\right)\frac{1}{d_3} + \left(\frac{A_4}{A_c}\right)\frac{1}{d_4}, \\ \tau_{\text{eff}} &= \tau_{b\leftrightarrow c} = (1/\tau_b + 1/\tau_c)^{-1} \end{aligned} \tag{10}$$

Recognizing that the molecules in both gaps perform random walks to equilibrate density variations, we determine the constituting time constants τ_b and τ_c as random walk escape times with Monte Carlo simulations as described in chapter 3. For reliable results we considered the true design of the gaps with geometrical details like trenches and etch holes, laid out according to the drawing of Fig. 2. The results for $d_{b\leftrightarrow c}$ and $\tau_{b\leftrightarrow c}$ are given in Tab. 2, together with the operational parameter $\omega_0\tau_{b\leftrightarrow c}$. Due to the two-wing butterfly mode we then find

$$\begin{aligned}\kappa^{\text{out}}_{\text{squeeze},b\leftrightarrow c} &= 2\,\kappa_{\text{squeeze}}(A_3, d_{b\leftrightarrow c}, \omega_0\tau_{b\leftrightarrow c}),\\ \beta^{\text{out}}_{\text{squeeze},b\leftrightarrow c} &= 2\beta_{\text{squeeze}}(A_3, d_{b\leftrightarrow c}, \omega_0\tau_{b\leftrightarrow c}),\end{aligned} \tag{11}$$

On a much shorter time scale, the same holds for the interaction of the $V_p = A_3\,d_3$ squeeze-film box volume directly under the plate with the volume $V_b = A_b\,d_3$ and $V_c = A_c\,d_4$ of the etch box and the cap, respectively. This case has also been treated in App. A. The effective values of the gap height and the escape time are given by

$$\begin{aligned}\frac{1}{d_{3\leftrightarrow b}} &= \frac{1}{d_3}\left(1 - \frac{A_3}{A_b}\right),\\ \frac{1}{d_{4\leftrightarrow c}} &= \frac{1}{d_4}\left(1 - \frac{A_4}{A_c}\right),\end{aligned} \tag{12}$$

$$\begin{aligned}\frac{1}{\tau_{3\leftrightarrow b}} &= \frac{1}{\tau_3} + \frac{1}{\tau_{b\to 3}},\\ \frac{1}{\tau_{4\leftrightarrow c}} &= \frac{1}{\tau_4} + \frac{1}{\tau_{c\to 4}}.\end{aligned} \tag{13}$$

The subscripts 'b' and 'c' refer to the etch box and the capping volume, respectively. In our device, we have $A_b \gg A_3$ and $A_c \gg A_3 (= A_4)$. This implies that the escape time from the squeeze film box under the plate is much shorter than the time to return to this volume from either the etch box or the capping volume, respectively. Because the shortest time determines the lion's share of the effective escape time, we can readily use the approximation $\tau_{3\leftrightarrow b} = \tau_3$ and $\tau_{4\leftrightarrow c} = \tau_4$.

The contribution from these coupled plate-to-box and plate-to-cap systems to damping and stiffness are

$$\begin{aligned}\kappa^{\text{out}}_{\text{squeeze},p\leftrightarrow b} &= 2\,\kappa_{\text{squeeze}}(A_3, d_3, \omega_0\tau_3),\\ \kappa^{\text{out}}_{\text{squeeze},p\leftrightarrow c} &= 2\,\kappa_{\text{squeeze}}(A_4, d_4, \omega_0\tau_4),\end{aligned} \tag{14}$$

$$\begin{aligned}\beta^{\text{out}}_{\text{squeeze},p\leftrightarrow b} &= 2\beta_{\text{squeeze}}(A_3, d_3, \omega_0\tau_3),\\ \beta^{\text{out}}_{\text{squeeze},p\leftrightarrow c} &= 2\beta_{\text{squeeze}}(A_4, d_4, \omega_0\tau_4).\end{aligned} \tag{15}$$

5 Kinetic damping

In addition, we also have a contribution from kinetic damping, which is always present and does not depend on the specific nature of the squeeze-film box. Its value only depends on the size of the surface area and its orientation with respect to the direction of the velocity vector of the plate. We can distinguish a perpendicular and a parallel contribution. The latter is mostly referred to as drag. In general, its contribution per unit area is mostly smaller than the perpendicular component. Both front and rear surfaces of the resonator contribute.

5.1 Perpendicular

From kinetic gas theory an extra contribution to the force exerted on the surface can be derived which is proportional to the plate velocity $|\vec{V}|$ and counteracts the movement. The contribution of kinetic damping to β is found with Christian's formula [7]:

$$\frac{\mathrm{d}b_{\mathrm{kin}}}{\mathrm{d}p} = \beta_{\mathrm{kin}} = \frac{16}{\pi}\frac{A}{\langle v\rangle}, \tag{16}$$

with $\langle v\rangle = \sqrt{8k_B T/(\pi M)}$ the average velocity of a gas molecule, M the molecular mass and k_B Boltzmann's constant. Please note that for deriving Eq. (16) the effect of collisions on both the front *and* the back side of the resonator has been taken into account. This is important to remember when we apply this formula to calculate kinetic damping in the in-plane mode. The ratio of squeeze damping to kinetic damping for a simple, uncoupled squeeze-film box is equal to

$$\frac{\beta_{\mathrm{squeeze}}}{\beta_{\mathrm{kin}}} = \frac{\pi}{16}\frac{\langle v\rangle}{v_{\mathrm{geom}}}, \tag{17}$$

with $v_{\mathrm{geom}} = d/\tau$ an effective velocity that depends on the geometry of the resonator. In general, for MEMS devices with $\sqrt{A} \gg d$, we find that $\beta_{\mathrm{squeeze}} \gg \beta_{\mathrm{kin}}$. For the 'dog-bone' resonator operated in the in-plane mode, the gap area is rather small and kinetic damping will play a dominant role.

5.2 Parallel

In general, kinetic damping contributes only to a damping in the direction perpendicular to the surface considered. The drag forces along the surface are much smaller, due to an increasingly smooth surface structure with increasing angle of incidence. In the in-plane mode, however, with the large value of the ratio $A_{\|}/A_{\perp} = 2A_3/(A_1 + 2A_2) =$

10.8 (top and bottom of plate), these drag forces can still result in a significant contribution to the damping.

If we assume that all collisions are inelastic for the in-plane component, we can easily derive the expression

$$\beta_{\text{drag}} = \frac{8}{\pi} \frac{A}{\langle v \rangle}. \tag{18}$$

For consistency with Eq. 16, collisions with both the top and bottom of the oscillating device have been taken into account. We observe that the effect of drag is a factor two smaller than the effect of kinetic damping. In contrast to kinetic damping, all elastic collisions do not contribute to β_{drag}. Grazing collisions with a trajectory at an angle θ to the normal on the surface for e.g. $\theta > 60°$, do not penetrate the surface potential very deeply. For this reason these molecules will only interact with a very smooth surface, with a large probability of a collision that is elastic in the parallel component without transfer of momentum.

In practical units this is expressed in terms of the parallel accommodation coefficient $\sigma_{\|}$, which is unity for full accommodation of the velocity component parallel to the surface and equal to zero for no accommodation of the parallel component. Typical values range from $0.2 < \sigma_{\|} < 0.5$ for polyatomic molecules in rarefied conditions ($\text{Kn} > 1$) at room temperature [8].

6 Functional resonator-mode experiments

To measure the quality factor Q and resonance frequency ω_0 of the device for pressures p in the mbar range we mounted a leaking sample (with a damaged cap) in a vacuum chamber with a base pressure less than 1×10^{-5} mbar. Through a needle valve we vented the chamber with pure nitrogen gas to achieve the desired pressure in the 0.1 to 1.0×10^{3} mbar range. The pressure was measured with an MKS Baratron 627B capacitance manometer with an accuracy of 0.1%. For different values of the pressure in the vacuum chamber, we measured the frequency response of two-port calibrated S-parameters using a HP8753D network analyzer. Bias voltage is applied to the resonator actuation gap through a bias-T on one of the analyzer ports. For extracting the motional admittance $Y_m(\omega)$, the S-parameters are converted into Y-parameters and corrected for the parasitics on the capacitively detected signal, yielding

$$Y_m(\omega) = -\Big(Y_{21}(\omega) - Y_{21}(\omega)\big|_0\Big), \tag{19}$$

where $Y_{21}(\omega)|_0$ denotes the zero bias spectrum.

Experimental values for the quality factor $Q(p)$ and the frequency shift $\Delta\omega_0(p) = \omega_0(p) - \lim_{p\to 0} \omega_0(p)$ are determined by a least-squares curve fit to a Lorentzian peak

Table 3: Experimental results for the pressure dependency of damping and stiffness of the in-plane modes of the ’dog-bone’, in comparison to calculated values based on our model (squeeze-film) and Christian (kinetic). The listed κ values are understood to have units 10^{-2} N/m mbar^{-1} and the β values to have units 10^{-10} kg/s mbar^{-1}. The number between parentheses indicates the error in the last digit.

Parameter	Experimental	Model
Q_{mat} ($\times 10^3$)	32.8(3)	
$\omega_0/2\pi$ (MHz)	55.753	56.0
p_β (mbar)	94(3)	
χ (ppm/mbar)	0.062(1)	
$\kappa^{\mathrm{in}}_{\mathrm{squeeze}}$		2.52
κ_{expt}	2.52(3)	
$\beta^{\mathrm{in}}_{\mathrm{squeeze}}$		0.25
$\beta^{\mathrm{in}}_{\mathrm{kin}}$		0.54
$\beta^{\mathrm{in}}_{\mathrm{drag}}$		0.58 to 1.45
$\beta^{\mathrm{in}}_{\mathrm{total}}$		1.8(4)
β_{expt}	1.89(8)	

function H at resonance frequency ω_0:

$$H(\omega) = H_0 \bigg/ \sqrt{4\left(\frac{\omega}{\omega_0} - 1\right)^2 + \frac{1}{Q^2}} \tag{20}$$

Here, H_0, ω_0 and Q are mutually independent curve-fitting parameters.

6.1 Stiffness

In Fig. 4 we show the experimental results for the relative frequency shift $\Delta\omega_0/\omega_0$ as a function of the N_2-pressure. This result is explained by the increased stiffness at higher pressures of the gas in the electrode gaps attributed to squeeze film damping. The increase of stiffness, Δk, is proportional to pressure p and causes a relative frequency shift $\Delta\omega_0/\omega_0$ given by:

$$\frac{\Delta\omega_0}{\omega_0} = \frac{\Delta k}{2k} = \chi\, p \tag{21}$$

$$\chi = \frac{\kappa_{\mathrm{expt}}}{2k_{\mathrm{mat}}}\,, \tag{22}$$

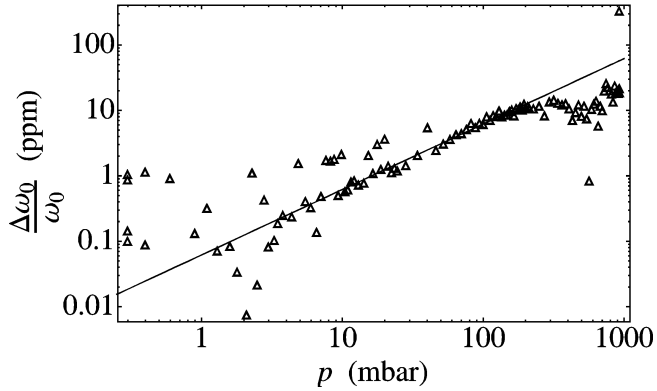

Figure 4: In-plane 56 MHz mode: experimental results for the shift $\Delta\omega_0/\omega_0$ of the resonance frequency as function of the ambient pressure p. Please note that a relative shift in frequency of 0.1 ppm corresponds to $\Delta\omega/2\pi = 6$ Hz, which explains the noise in the data at low pressure.

as based on the relation $\omega_0 = \sqrt{k/m}$. Here we linearized the expression for $\omega_0(k+\Delta k)$ because we can take $\Delta k \ll k$. By a linear fit through the measured data of Fig. 4 we determined the value of χ. The experimental result for κ_{expt} as calculated with Eq. (22) is given in Tab. 3. The theoretical result for $\kappa^{\text{in}}_{\text{squeeze}}$ (Eq. (7)) is also given in this table. We see an excellent agreement between experiment and model.

6.2 Damping

In Fig. 5 we show the experimental result for the quality factor Q as a function of the N_2-pressure in the test chamber at ambient temperature $T = 22$ °C. To analyze these data we use the fact that the damping coefficient b is made up from a structural contribution b_{mat} depending on the structural quality factor Q_{mat} and a gas-dependent contribution b_{gas} proportional to vacuum pressure p:

$$b = b_{\text{mat}} + b_{\text{gas}} = \frac{k_{\text{mat}}}{\omega_0\, Q_{\text{mat}}} + \beta_{\text{expt}}\, p\ , \tag{23}$$

where β represents the pressure sensitivity of the resonator damping in the in-plane mode. By applying the definition $b = k/(\omega_0\, Q)$, the total quality factor Q reads:

$$Q \equiv \frac{k}{\omega_0\, b} = \frac{k}{\omega_0\left(\frac{k}{\omega_0\, Q_{\text{mat}}} + \beta_{\text{expt}}\, p\right)}\,. \tag{24}$$

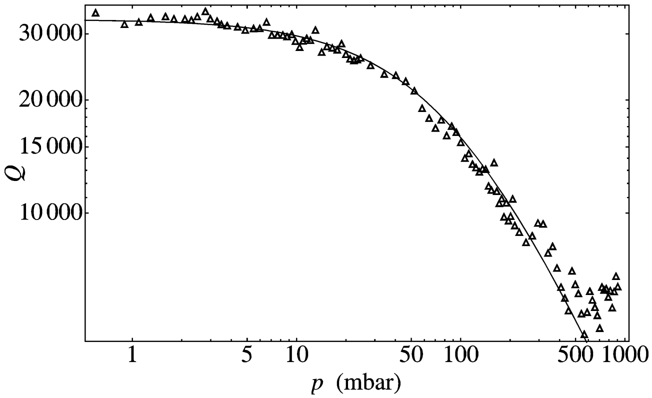

Figure 5: In-plane 56 MHz mode: experimental results for the quality factor Q as function of the ambient pressure p.

The pressure dependence of the quality factor therefore satisfies:

$$Q = Q_{\mathrm{mat}}/[1 + (p/p_{\beta})]. \tag{25}$$

$$p_{\beta} = \frac{k_{\mathrm{mat}}}{\omega_0\, Q_{\mathrm{mat}}} \frac{1}{\beta_{\mathrm{expt}}} . \tag{26}$$

By performing a least-squares curve fit of Eq. (25) on the measured data, we can extract the values of Q_{mat} and p_{β}. Together with the experimental value β_{expt} of the device's pressure sensitivity to the damping, the results are presented in Tab. 3. Also listing the calculated contributions $\beta^{\mathrm{in}}_{\mathrm{squeeze}}$, $\beta^{\mathrm{in}}_{\mathrm{kin}}$ and β_{drag} from our theoretical expressions, this table shows a direct comparison of the total value $\beta^{\mathrm{in}}_{\mathrm{total}}$ of the model with the experimental result β_{expt}.

For the in-plane mode we observe that the in-gap kinetic damping is a factor two larger than the contribution of squeeze-film damping. Given the large ration of $A_{\|}/A_{\perp}$ in this mode, this implies that drag will play a very large role in damping. By substituting $A = 2A_3$ in Eq. (18) we find $\beta_{\mathrm{drag}} = 2.89 \times 10^{-10}$ kg/s mbar^{-1} for $\sigma_{\|} = 1.0$; for values in the range 0.2 to 0.5 we then find $0.58 < \beta_{\mathrm{drag}}/(10^{-10}$ kg/s mbar$^{-1}) < 1.45$. The difference $\beta_{\mathrm{expt}} - \beta_{\mathrm{squeeze}} - \beta_{\mathrm{kin}} = 1.09 \times 10^{-10}$ kg/s mbar^{-1} neatly falls in this range.

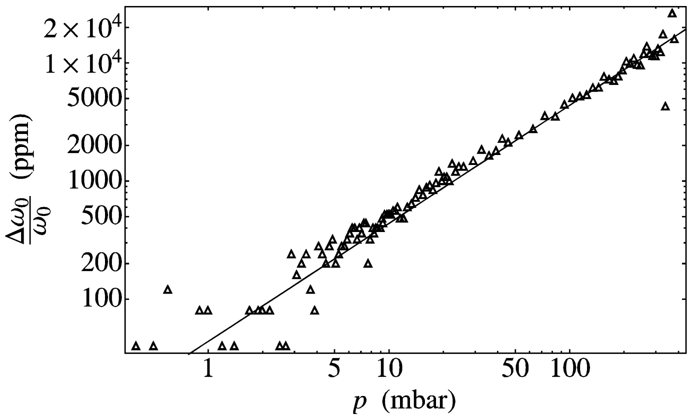

Figure 6: Out-of-plane 2.5 MHz mode: experimental result for the shift $\Delta\omega_0/\omega_0$ as function of the ambient pressure p.

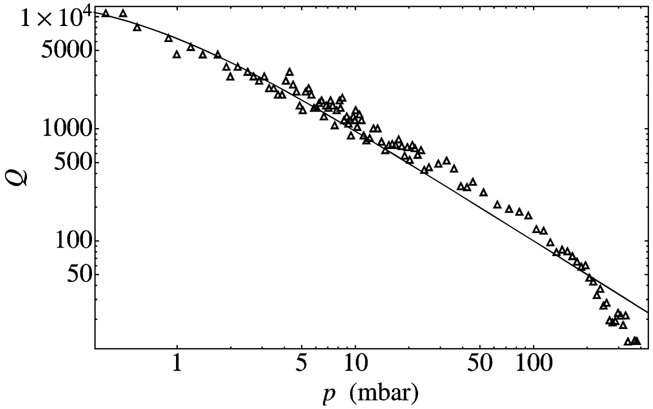

Figure 7: Out-of-plane 2.5 MHz mode: experimental results for the quality factor Q as function of the ambient pressure.

7 Pressure-sensing experiments

Because our device was not designed with cap/substrate electrodes for an electrostatic read-out of the out-of-plane motion, we use a Polytec laser vibrometer setup[2] to do it optically. Here, the device capping layer does not obstruct the laser beam and probing is unproblematic via the view port of the vacuum container. We simultaneously excite various distinct out-of-plane eigen-modes of the resonator by a white-noise driving voltage at the in-plane electrodes. The setup converts the detected (time domain) signal to a frequency spectrum resolving the resonance peaks that correspond to each of the eigenmodes. From the peak with the one but lowest resonance frequency – selected according to a modal frequency analysis in COMSOL –, we determine quality factor and shift of the resonance frequency as function of vacuum pressure. The considered 'butterfly' mode involves symmetric up and down movement of the two plates (Fig. 3). Simulated values for the corresponding frequency as well as stiffness are listed in Tab. 1. Experimental results are shown in Figs. 6 and 7.

7.1 Damping

Again extracting values of the cut-off pressure p_β and frequency sensitivity χ from curve fits on Eqs. (25) and (21), we note the increase of two – for χ even three – orders of magnitude with respect to the in-plane operation. In view of the two gaps characterized by d_3 and d_4, respectively, and the large area A_3 of a single resonator wing in the out-of-plane mode, the dominance of the squeeze film effect on gas damping is not surprising.

An effective model for the two coupled gaps (App. A) is based on our single-gap model. If we compare the experimental results to the predicted values of the three contributions to squeeze-film damping, we observe an excellent agreement with the experiment. All contributions are caused by coupled systems, using Eq. (9) with effective diffusion time τ_{eff} and gap height d_{eff} as given in Tab. 2. The two largest contributions (35% each) are caused by a rapid coupling of the squeeze-film box located directly underneath and above the oscillating plate with the etch box and the capping volume, respectively. The coupled system consisting of the etch box and the capping volume accounts for another 12% of the damping. Finally, kinetic damping also contributes 17% of the total value. From this good agreement we can conclude that our simple analytical model for coupled systems of squeeze-film boxes is a valuable extension of the result of Suijlen et al. for a single, isolated squeeze-film box. The only numerical input consists of a simple Monte Carlo calculation of the average values of the six relevant escape times τ_1 through τ_4, τ_b and τ_c.

---

[2] MSA-500-TPM2-20-D system, see `www.polytec.com`

Table 4: Experimental results for the pressure dependency of damping and stiffness of the out-of-plane mode of the ’dog-bone’, in comparison to calculated values based on the models presented in this chapter (squeeze-film) and Christian (kinetic). The listed κ values are understood to have units 10^{-2} N/m mbar^{-1} and the β values to have units 10^{-10} kg/s mbar^{-1}.

Parameter	Experimental	Model
Q_{mat} ($\times 10^3$)	17.4(9)	
$\omega_0/2\pi$ (MHz)	2.507	2.51
p_β (mbar)	0.58(5)	
χ (ppm/mbar)	44(1)	
Stiffness		
$\kappa^{\text{out}}_{\text{squeeze},b\leftrightarrow c}$		1.82
$\kappa^{\text{out}}_{\text{squeeze},3\leftrightarrow b}$		1.75
$\kappa^{\text{out}}_{\text{squeeze},4\leftrightarrow c}$		0.80
$\kappa^{\text{out}}_{\text{total}}$		4.37
κ_{expt}	4.66(11)	
Damping		
$\beta^{\text{out}}_{\text{squeeze},b\leftrightarrow c}$		4.2
$\beta^{\text{out}}_{\text{squeeze},3\leftrightarrow b}$		11.9
$\beta^{\text{out}}_{\text{squeeze},4\leftrightarrow c}$		12
$\beta^{\text{out}}_{\text{kin}}$		5.8
$\beta^{\text{out}}_{\text{drag}}$		0.1
$\beta^{\text{out}}_{\text{total}}$		34
β_{expt}	34(5)	

Conversely, from the value $\beta^{\text{in}}_{\text{drag}} = 1.09 \times 10^{-10}$ kg/s mbar^{-1} for the in-plane mode, we can readily estimate the contribution of damping by drag forces in the out-of-plane mode, by multiplying this value by the corresponding surface ratio as given by

$$\beta^{\text{out}}_{\text{drag}} = (A_2 + 2A_1)/(2A_3)\beta^{\text{in}}_{\text{drag}} \tag{27}$$

This results in a value $\beta^{\text{out}}_{\text{drag}} = 0.1{\times}10^{-10}$ kg/s mbar^{-1} for the out-of-plane mode as given in Tab. 4. As expected, the drag forces do not play a significant role in the out-of-plane mode.

7.2 Stiffness

All three coupled squeeze-film systems contribute equally to the stiffness of the device, with the smallest contribution from the coupled system of the plate to the capping volume. This is due to the short escape time τ_4 and the large ratio of the capping volume V_c to the volume V_p of the squeeze-film box under the plate.

7.3 Life-time testing

We can now assess the role of probing the out-of-plane mode as a measure for speeding up the testing of the device for its 10-year specification of stable oscillation in the functional in-plane mode. Experiment and modeling fully agree on the data for the pressure sensitivity of damping and the shift in operating frequency, as expressed by p_β and χ. For the two modes we find an increased sensitivity for the out-of-plane mode characterized by the ratio

$$\begin{aligned} p^{\text{out}}_\beta / p^{\text{in}}_\beta &= 1/162, \\ \chi^{\text{out}}/\chi^{\text{in}} &= 710. \end{aligned} \tag{28}$$

These numbers are on the same order of magnitude as the off-the-cuff estimates made in section 3, without looking into details of the processes involved. From these numbers we can conclude that measuring the shift in operating frequency has the largest gain in sensitivity to an increase in pressure. The increase in pressure during its 10-year lifetime can now be tested on a time scale that is a factor 700 shorter, i.e., a single week. This an attractive option for gaining insight in the quality of vacuum packaging.

8 Concluding remarks

We have presented a new approach to rapid characterization of the quality of the on-wafer capping of MEMS devices that have to be operated in vacuum conditions. High-frequency MEMS oscillators in the 10 - 500 MHz range, that function in an in-plane mode, can readily be operated in a low-stiffness out-of-plane mode. The radical different geometry of squeeze-film gaps results in a pressure sensitivity of damping and shifts in resonance frequency that are two to three orders larger for the diagnostic out-of-plane mode. This speeds up operational testing of the vacuum tightness of the capping considerably, allowing a new range of tests to investigate the desired lifetime for the functional high-frequency mode.

A Two-chamber squeeze film damping

A.1 Box-cap coupling

As a generic system, we consider two squeeze-film systems γ and δ with volume V_γ and V_δ, respectively. The system as a whole is closed, with $N_\gamma + N_\delta = n_0\,(V_\gamma + V_\delta)$ and n_0 the density in equilibrium. We assume an oscillating plate as a shared wall separating both systems, with area A_p. The systems are coupled by a current I that depends on a driving force derived from the oscillating plate. Each system is characterized by a gap height equal to d_γ and d_δ, respectively.

With regard to the density n_γ of system γ, the following equations hold:

$$I = \frac{V_\gamma}{\tau_\gamma}\,(n_\gamma - n_0) - \frac{V_\delta}{\tau_\delta}\,(n_\delta - n_0), \tag{29}$$

where the time constants τ_γ and τ_δ account for the ”resistance” that the flow experiences in the connection between the squeeze-film systems with volume V_γ and V_δ, respectively. This connection can for instance consist of trenches and etch holes.

Assuming a displacement $z(t) = z_0 \, e^{i\omega t}$ of the oscillating plate, we propose a trial solution $\Delta n_k(t) = \Delta n_{k,0} \, e^{i\omega t}$ with $k = \gamma, \delta$ with small amplitudes $z_0 \ll d_k$ and $\Delta n_{k,0} \ll n_0$. This results in the following coupled differential equations:

$$\begin{aligned} \frac{\mathrm{d}}{\mathrm{d}t}(N_\gamma + N_\delta) &= 0, \\ \frac{\mathrm{d}}{\mathrm{d}t} N_\gamma + I &= 0, \end{aligned} \tag{30}$$

$$\begin{aligned} N_\gamma \equiv n_\gamma \, V_\gamma &= (n_0 + \Delta n_\gamma(t)) \, (A_\gamma \, d_\gamma + A_p \, z(t)), \\ N_\delta \equiv n_\delta \, V_\delta &= (n_0 + \Delta n_\delta(t)) \, (A_\delta \, d_\delta - A_p \, z(t)), \end{aligned} \tag{31}$$

The role of the oscillating plate as a shared wall of the two systems is reflected in the different signs for the contribution $A_p \, z(t)$ in the expressions for N_γ and N_δ. In solving these equations we only consider terms that are first order in the amplitude $z(t)$. Together with Eq. (29) we then arrive at:

$$\Delta n_\gamma(t) = -n_0 \, \frac{A_p}{V_\gamma} \, \frac{i\omega\tau_{\text{eff}}}{i\omega\tau_{\text{eff}} + 1} \, z(t), \tag{32}$$

$$\frac{1}{\tau_{\text{eff}}} = \frac{1}{\tau_\gamma} + \frac{1}{\tau_\delta}, \tag{33}$$

$$\Delta n_\delta(t) = -\frac{V_\gamma}{V_\delta} \, \Delta n_\gamma(t). \tag{34}$$

The force F_{squeeze} on the resonator plate is readily derived from the ideal-gas law:

$$\begin{aligned} F_{\text{squeeze}}(t) &= \Delta p_{\text{squeeze}}(t) \, A_p \\ &= (n_\gamma - n_\delta) \, k_B \, T \, A_p = \frac{\Delta n_\gamma - \Delta n_\delta}{n_0} \, p_0 \, A_p \, , \end{aligned} \tag{35}$$

where $p_0 = n_0 \, k_B \, T$ denotes the pressure at temperature T for the case of a stationary resonator plate. Applying Eqs. (32) and (34), the squeeze force due to connected gaps satisfies:

$$\begin{aligned} F_{\text{squeeze}} &= -\frac{p_0 \, A_p}{d_{\text{eff}}} \, \frac{i\omega\tau_{\text{eff}}}{1 + i\omega\tau_{\text{eff}}} \, z, \\ \frac{1}{d_{\text{eff}}} &= \frac{A_p}{V_\gamma} + \frac{A_p}{V_\delta} \\ &= \left(\frac{A_p}{A_\gamma}\right) \frac{1}{d_\gamma} + \left(\frac{A_p}{A_\delta}\right) \frac{1}{d_\delta} \end{aligned} \tag{36}$$

Here, we assume that the volumes are given by $V_k = A_k\, d_k$ with $k = \gamma, \delta$. We see that our existing formula for the squeeze force holds, but with an effective time constant τ_{eff} and an effective gap height d_{eff}. The weight factors in the definition of the effective gap height take into account the fraction of the area that is actually driven by the oscillating plate (e.g., squeeze-film box) to the lateral dimension of the area of the total structure (e.g., etch box or cap).

A.2 Plate-box and plate-cap coupling

On a different time scale, the results of the previous section also hold for the coupled system of the squeeze-film box under and above the oscillating plate with the volume of the etch box and the cap, respectively. The obvious difference is in the expression for the squeeze force F_{squeeze}, as compared to Eq. 35. Here, both contributions Δn_γ and Δn_δ to the increase in density act on the same side of the oscillator plate, resulting in

$$F_{\text{squeeze}}(t) = \frac{\Delta n_\gamma + \Delta n_\delta}{n_0}\, p_0\, A_p. \tag{37}$$

By substituting the expressions for Δn_k with $k = \gamma, \delta$ we find the same expression for F_{squeeze} as in Eq. 36, however, with a different result for the effective gap height d_{eff}.

$$\frac{1}{d_{\text{eff}}} = \frac{A_p}{V_\gamma} - \frac{A_p}{V_\delta}. \tag{38}$$

Using $V_\gamma = A_p\, d_\gamma$ and $V_\delta = A_\delta\, d_\gamma$ this result can be written as

$$\frac{1}{d_{\text{eff}}} = \frac{1}{d_\gamma}\left(1 - \frac{A_p}{A_\delta}\right). \tag{39}$$

This result is rather easy to understand for $A_\delta \gg A_p$. With increasing volume of the etch box or the cap, as compared to the volume of the squeeze-film box under the oscillating plate, we observe that $1/d_{\text{eff}} \approx 1/d_\gamma$. This implies that both stiffness and damping approach the limit of an oscillating plate in a residual gas without flow restrictions.

In the limit of A_δ approaching A_p, the escape time goes to infinity and the system acts as a closed squeeze-film box under the plate, without damping and a pressure dependence of the stiffness equal to $\kappa_{\text{squeeze}} = A_p/d_\gamma$. This is the equivalent of an air cushion with its stopper in place.

References

[1] M. Waelti, N. Schneeberger, O. Paul, H. Baltes, Int. J. Microcircuits and Electronic Packaging **22** (1) (1999) 49-56.

[2] W. Reinert et al., Proc. IEEE EPTC (2005) pp 225.

[3] F. Mailly, N. Dumas, N. Pous, L. Latorre, O. Garel, E. Martincic, F. Verjus, C. Pellet, E. Dufour-Gergam, P. Nouet, Sens. and Actuators A **156** (2009) 201-207.

[4] Q. Li, J.F.L. Goosen, J.T.M. van Beek, F. van Keulen, Sens. Actuators A **162** (2010) 267-271.

[5] J.J.M. Bontemps et al., Digest Tech. Papers Transducers 2009 pp 1433-1436.

[6] P.J. van der Wel, J. Stulemeijer, J.A. Bielen, F.G.A. Theunis, A. den Dekker, M.A.J. van Gils, R.J. Havens, Proc. IEEE CFP08RPS-CDR (2008) pp 691.

[7] R.G. Christian, Vacuum **16** (4) (1966) 175-178.

[8] A. Agrawal, S.V. Prabhu, J. Vac. Sci. Technol. A **26** (4) (2008) 634-645.

Chapter 6

Modeling mTorr ambient-gas damping of intricate MEMS resonators: simple and sound

Abstract

We developed a simple analytical model for describing squeeze-film forces on MEMS resonators in the free molecular region, with the average escape time τ of a molecule from the squeeze-film box as the only device-based free parameter. A comparison of model predictions to the data found on devices of various geometries in recent literature yields relative differences that are normally distributed with a standard deviation of 12%. This result holds a promise for state-of-the-art modeling of MEMS resonator damping and efficient model-based design of intricate MEMS devices.

1 Introduction

Squeeze-film damping of MEMS resonators in the free molecular flow regime is an interesting problem that has been attracting a lot of attention in the last decade. However, the field is still trying to define an approach that combines insight in the underlying processes with accurate predictions of both damping and frequency shift. Also, numerical simplicity is a very important boundary condition, because the MEMS resonator devices are being manufactured with an increasingly complex geometrical structure.

At present, modeling of rarefied squeeze-film flow includes two approaches, roughly characterized as (1) solving the Reynolds equation coupled with an effective viscosity and (2) describing the behavior of individual molecules based on gas kinetics.

Although the first approach can predict both damping and frequency shift of the resonator due to film flow, its application to complex geometrical structures in real-life technology – including etch holes, springs and stacked devices – is impossible without a highly specialized and tedious programming effort. The second approach directly models molecular transport and is particularly appealing because of its simplicity and accuracy. A solid description of free molecular flow in the confined space of a squeeze-film is the only way to explain the dependence of device damping and resonance frequency on ambient pressure.

The basics are rather simple: due to the oscillation of the resonator according to $z_0 \sin(\omega t)$, the number density in the ”box” between resonator and the fixed substrate will vary proportional to $\sin(\omega t + \phi)$. The driving force for the variation of the density is the varying height of the gap $d(t) = d + z_0 \sin(\omega t)$. In a macroscopic picture, an increase in height results in an increase in volume and thus a decrease in number density and vice versa. In a microscopic picture, the increase in height results in an increase in the roundtrip time of the colliding molecules and thus in a decrease of the wall collision rate which indicates a decrease in number density. The phase difference ϕ reflects the time lag in equalizing the number density to its value outside the

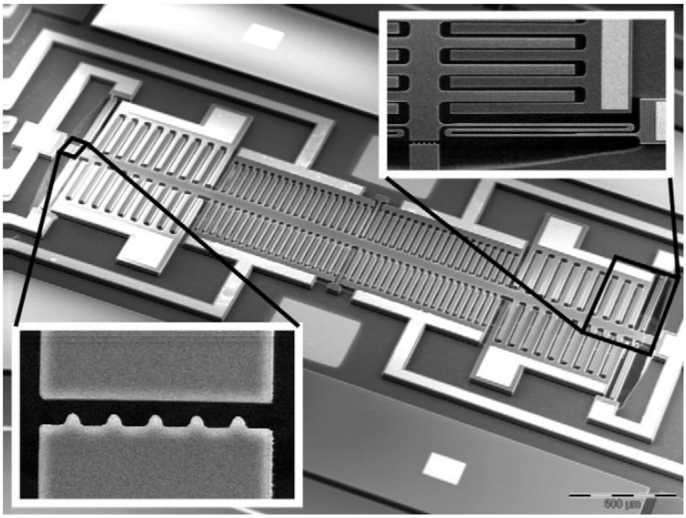

Figure 1: SEM image of the fabricated device reproduced from Mol et al. [1]. The narrow electrodes in the centre form the sensing capacitors and the wider ones on the outside are for electrostatic actuation. The insets show the details of a spring, a stopper and actuation electrodes.

squeeze film by the action of free molecular flow. This time lag will arguably equal the escape or diffusion time of gas out of (or into) the gap. Diffusing molecules will only cancel a density difference between gap and environment when moving between these spaces. Considering free molecular flow, the molecules will, totally independent of each other, perform a random walk in the gap between microstructure and substrate. Monte Carlo routines are ideally suited for the simulation of this transport and the calculation of quantities involved. By applying such routines for the calculation of diffusion times, we have found very good agreement with the experimentally observed damping and frequency shift of six different resonators due to squeeze-film damping.

Urged by the comparatively large modeling discrepancies in squeeze-film damping studies regarding the free molecular region, we tested our model on the data found with entirely different devices in recent literature. It turns out our model also fits well to these observations which holds a promise for state-of-the-art modeling of MEMS resonator damping. In this article we report on the quantitative comparison of model and experimental data that has come available in publications to date.

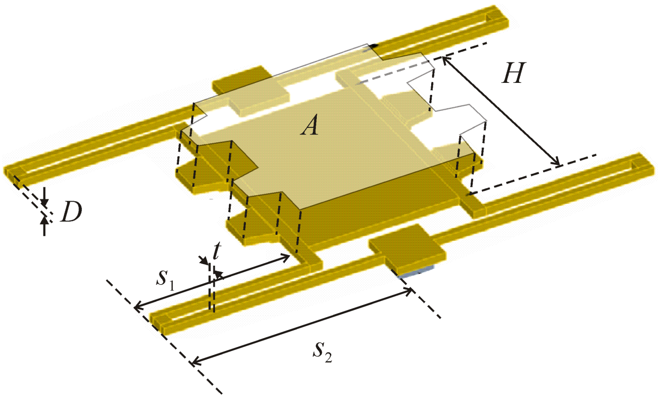

Figure 2: Sumali's resonator structure with indication of relevant sizes.

2 Available data

The data we found in literature on resonators op-erated in the free molecular flow regime with sufficient specifications and characterized as a function of vacuum pressure cover the articles of Mol et al. [1], Sumali [2], Legtenberg et al. [3] and Minikes et al. [4]. We would like to find numerical values for the pressure sensitivity $\beta = \mathrm{d}b/\mathrm{d}p$ of the damping coefficient b. This coefficient denotes the proportionality of the damping force F_d to the velocity of the resonator mass v:

$$F_d = -b \cdot v \tag{1}$$

As only Mol et al. express their observations in this quantity, we need to convert the particular forms that the other three articles use to express their damping results.

2.1 Multi-beam sensor/actuator

Mol et al. perform their measurements on a single Degree-Of-Freedom (1-DOF) MEMS resonator structure featuring a 25 µm device layer thickness (Fig. 1). The device consists of a central mass suspended on four folded springs. Four distinct sets of electrodes are attached to a central moving bar, which are interleaved with electrodes that are fixed to the substrate. The two narrow beam sets form a differential capacitor that is used to read out the device displacement, while each of the wider beam sets is used to excite the mass through electrostatic actuation in either direction. Table 1 lists the key properties of the device.

Table 1: Key properties of the MEMS resonator used by Mol et al.

Property	Value	Unit
Mass (m)	42.0	µg
Spring constant (k)	12.9	N/m
Undamped natural frequency (ω_0)	2.84	kHz
Sense capacity (C_s)	1.12	pF
Device layer thickness (H)	25.0	µm
Length sense arm (L_{sa})	230	µm
Length actuation arm (L_{aa})	300	µm
Number of sense arms (N_{sa})	40	
Number of actuation arms (N_{aa})	18	
Small gap width (d_1)	2.29	µm
Large gap width sense electrodes ($d_{2,s}$)	14.3	µm
Large gap width actuation electrodes ($d_{2,a}$)	12.3	µm

2.2 Parallel plate oscillator

Sumali's test structure (Fig. 2) consists of a plate suspended by four folded-beam springs. One end of each spring supports the plate and the other end is anchored to the substrate. Made of electro-deposited gold, the test structure has four trapezoidal tabs on the ends of the plate. However, in applying analytical models, this plate is assumed quasi-rectangular with a length equal to the *plate area* A including the tabs divided by the *plate width* H. Sumali introduces the quantity ζ which relates to b in the following manner:

$$b = 2m\,\omega_0\,\zeta \tag{2}$$

with m the resonator mass and ω_0 the resonance frequency of the device. We find:

$$\beta = 2m\,\omega_0\,\mathrm{d}\zeta/\mathrm{d}p \tag{3}$$

The resonator mass is found to be the sum of the static mass of the plate m_{plate} and a mass contribution from the springs according to Blevins [5]:

$$m = m_{\text{plate}} + 4 \cdot 0.37\,m_{\text{spring}} \tag{4}$$

Table 2: List of values for determined sizes in test structure of Sumali et al. [2].

Property	Value (μm)
Plate width H	154
Plate length L (= A/H)	193
Structure thickness D	5.7
Spring length s (= $s_1 + s_2$)	350
Spring width t	5.0

Using data on structure thickness as given by Hong [6] and known density for gold we calculate this mass to be:

$$m = \rho\,(D\,A + 4 \cdot 0.37\,D\,s\,t), \tag{5}$$

with ρ the density and D the structure thickness. The sizes s and t of a spring are determined by measuring them in the scale drawing. In common illustration software this is easily done to 5% accuracy.

2.3 Beam resonators

The resonators that Legtenberg et al. investigate consist of a prismatic beam with a rectangular cross section and are housed in an evacuated cavity. The beam thickness is approximately 1.5 μm. Furthermore, a beam-to-substrate gap of approximately 1.2 μm and a beam-to-cap gap of 1.5 μm were specified. In particular we consider the data of the ”310 μm-no cap” device that, as the name suggests, lacks a cap.

Legtenberg et al. and Minikes et al. choose to plot quality factor Q against pressure on a log-log scale. For the pressure range far from the low pressure region featuring Q values constant with pressure, one may use:

$$\beta = m\,\omega_0/(Q\,p) \tag{6}$$

with $m = \rho\,V$ and $V = A\,D$ the volume of the oscillating plate. Here, A is the area of the structure perpendicular to its velocity and D is the thickness of the structure.

2.4 Torsion mirrors

Minikes et al. conducted experiments on two different torsion mirrors having similar dimensions in terms of surface area and inertial moment, but having different gaps between the mirror and the actuation electrodes. The nominal values of the physical

Table 3: Experimental valuess of $\beta = \mathrm{d}b/\mathrm{d}p$ for devices as reported by Mol (2009), Sumali (2007), Legtenberg (1994) and Minikes (2005), together with essential data for calculating β.

	Mol	**Sumali**	**Legtenberg**	**Minikes1**	**Minikes2**
Material	Silicon	Gold	Silicon	Silicon	Silicon
ρ (10^3 kg/m^3)	2.33	19.3	2.33	2.33	2.33
A (μm^2)	-	154×193	100×310	500×500	500×500
D (μm)	25	5.7	1.5	30	30
m (μg)	42	3.5	0.11	31.1	31.1
$\omega_0/2\pi$ (kHz)	2.84	16.91	163	13.1	12.8
$\mathrm{d}\zeta/\mathrm{d}p$ (mbar^{-1})	-	$1.1\,10^{-3}$	-	-	-
$Q \cdot p$ (mbar)	-	-	95	$2.0\,10^3$	$6.7\,10^2$
β_{expt} (10^{-6} kg/s mbar^{-1})	5.0	0.81	1.16	0.96	2.82
$\Delta\beta_{\mathrm{expt}}/\beta_{\mathrm{expt}}$ (%)	5	7	7	6	6

parameters of the two mirrors (referred to as 'Minikes1' and 'Minikes2') are summarized in Tabs. 3 and 4.

Minikes et al. also plot the quality factor Q against pressure p on a log-log scale. This results in the same equation for β as is the case for Legtenberg (Eq. (6)). Because Minikes' torsion mirrors perform angular instead of linear movements, their effective mass however will be different. According to Minikes' analysis, a linear amplitude y can be found equivalent to the angular amplitude θ as given by

$$y = (H/4)\,\theta\,, \tag{7}$$

where H is the mirror width, transverse to the torsion axis. Requiring that the kinetic energy for this linear amplitude equals the rotational energy at given angular amplitude θ,

$$\frac{1}{2}m'\,\dot{y}^2 \cong \frac{1}{2}I\,\dot{\theta}^2\,, \tag{8}$$

with $I = (m/12)\,H^2$ the moment of inertia about the torsion axis, the effective mass m' is found to be:

$$m' = (4/3)\,m = (4/3)\,\rho\,V_{\mathrm{plate}} \tag{9}$$

Table 4: Results of the model comparison to devices of Mol (2009), Sumali (2007), Legtenberg (1994) and Minikes (2005), respectively.

		Mol		**Sumali**	**Legtenberg**	**Minikes1**	**Minikes2**
		’s’	’a’				
L	$(10^{-6}$ m)	230	300	193	310	500	500
H	$(10^{-6}$ m)	25	25	154	100	500	500
A	$(10^{-9}$ m$^2)$	5.75	7.50	29.7	31.0	250	250
N		80	36				
d_1	$(10^{-6}$ m)	2.29	2.29	4.1	1.18	28	13
d_2	$(10^{-6}$ m)	14.3	12.3				
τ_1	$(10^{-6}$ s)	0.151	0.154	1.01	1.86	1.10	1.47
τ_2	$(10^{-6}$ s)	0.135	0.139				
$\omega_0\tau_1$		0.0027	0.0027	0.107	1.90	0.091	0.118
$\omega_0\tau_2$		0.0024	0.0024				
β_{kin}	$(10^{-6}$ kg/s mbar$^{-1})$	0.79		0.03	0.03	0.14	0.14
$\beta_{\mathrm{squeeze,1}}$	$(10^{-6}$ kg/s mbar$^{-1})$	3.0	1.81	0.73	1.06	0.97	2.79
$\beta_{\mathrm{squeeze,2}}$	$(10^{-6}$ kg/s mbar$^{-1})$	0.43	0.29				
β_{model}	$(10^{-6}$ kg/s mbar$^{-1})$	6.32		0.76	1.09	1.11	2.93

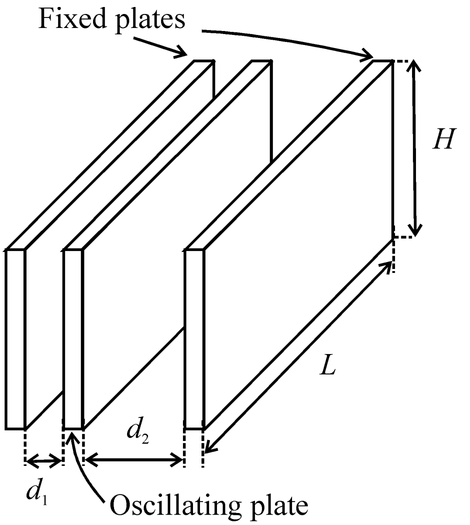

Figure 3: Two plates of length L and height H define a channel of width w. The gas in the gap between the plates causes a damping force to counteract the movement of the oscillating plate.

2.5 Pressure sensitivity

In Tab. 3 we have compiled the essential data of all devices, together with the experimentally obtained values for the pressure sensitivity β. By conservative judgment from the various source papers we estimated a value for the relative error $\Delta\beta_{\mathrm{expt}}/\beta_{\mathrm{expt}}$ of the observations. We used a value of 5% for the error in the extracted observable (β, $\mathrm{d}\zeta/\mathrm{d}p$ or $Q \cdot p$) and increased it with the eventual error related to the resonator mass, respectively dimensions.

3 Model comparison

We now will compare the experimental data to the predictions of our single parameter model for the pressure sensitivity β. Because we are interested in a comparison in the range of a few percent, we also must take into account the contribution β_{kin} of kinetic damping on the resonators according to Christian [7]. Therefore the sensitivity is modeled as:

$$\begin{aligned}\beta_{\mathrm{model}} &= \beta_{\mathrm{kin}}(A, \langle v \rangle) + \beta_{\mathrm{squeeze}}(A, d, \tau, \omega_0) \\ &= \frac{16}{\pi}\frac{A}{\langle v \rangle} + \frac{A}{d}\frac{\tau}{1 + (\omega_0 \tau)^2} ,\end{aligned} \tag{10}$$

with A the area of the squeeze-film box, d the height of the gap and $\langle v\rangle = \sqrt{8k_B\,T/(\pi\,M)}$ the average velocity. The parameter τ is the average value of the escape time of the molecules from the squeeze-film box, as calculated by random walk simulation of individual molecules using a TPMC procedure as described in chapter 3. The expression for β_{kin} is based on double-sided action of the impinging gas molecules. In contrast, the expression for β_{squeeze} is based on a single squeeze-film box at one side of the oscillating plate or beam. In general this is true, although exceptions occur when a device has a cap close to the top surface or when we consider multi-beam resonators as is the case with Mol's device. The devices of Sumali, Legtenberg and Minikes have a single vibrating plate, which allows an easy comparison with Eq. (10) (Tab. 4).

3.1 Multi-beam sensor/actuator

The squeeze-film damping of the device investigated by Mol occurs at both sides of the sensor and actuator beams, each with its own gap height (Fig. 3). The total number of beams that contribute equals $N_s = 80$ and $N_a = 36$ for the sense and actuation beams, respectively. Please note that the number of arms stated by Mol refers to a set of two arms, one at each side of the central connecting bar and thus is a factor of two lower than the values we give for N_s and N_a, respectively. We have a squeeze-film box at both sides of each arm, each with a different gap height. These values are $d_1 = 2.29$ µm for the narrow gap and $d_{2,s} = 14.3$ µm and $d_{2,a} = 12.3$ µm for the wide gap of the sense and the actuator arms, respectively. The escape times are also different for all these different squeeze-film boxes. The squeeze-film boxes are open along the long side with length $L = 230$ µm and 300 µm, respectively, and only connected along the short side with height $H = 25$ µm, eliminating the need to treat them as a system of coupled boxes. The expression for β_{kin} takes into account that both the top and bottom surface are bombarded by gas molecules. This implies that the surface area that contributes to kinetic damping is equal to $N_s\,A_s + N_a\,A_a$. For the total structure we obtain:

$$\begin{aligned}\beta_{\mathrm{Mol}} = {} & N_s\,\beta_{\mathrm{squeeze}}(A_s, d_{1,s}, \tau_{1,s}, \omega_0) + N_s\,\beta_{\mathrm{squeeze}}(A_s, d_{2,s}, \tau_{2,s}, \omega_0) + \\ & N_a\,\beta_{\mathrm{squeeze}}(A_a, d_{1,a}, \tau_{1,a}, \omega_0) + N_a\,\beta_{\mathrm{squeeze}}(A_a, d_{2,a}, \tau_{2,a}, \omega_0) + \\ & N_s\,\beta_{\mathrm{kin}}(A_s, \langle v\rangle) + N_a\,\beta_{\mathrm{kin}}(A_a, \langle v\rangle) \qquad (11)\end{aligned}$$

The subscript 's' and 'a' denotes the electrode beams for sensing and for actuation of the resonator, respectively.

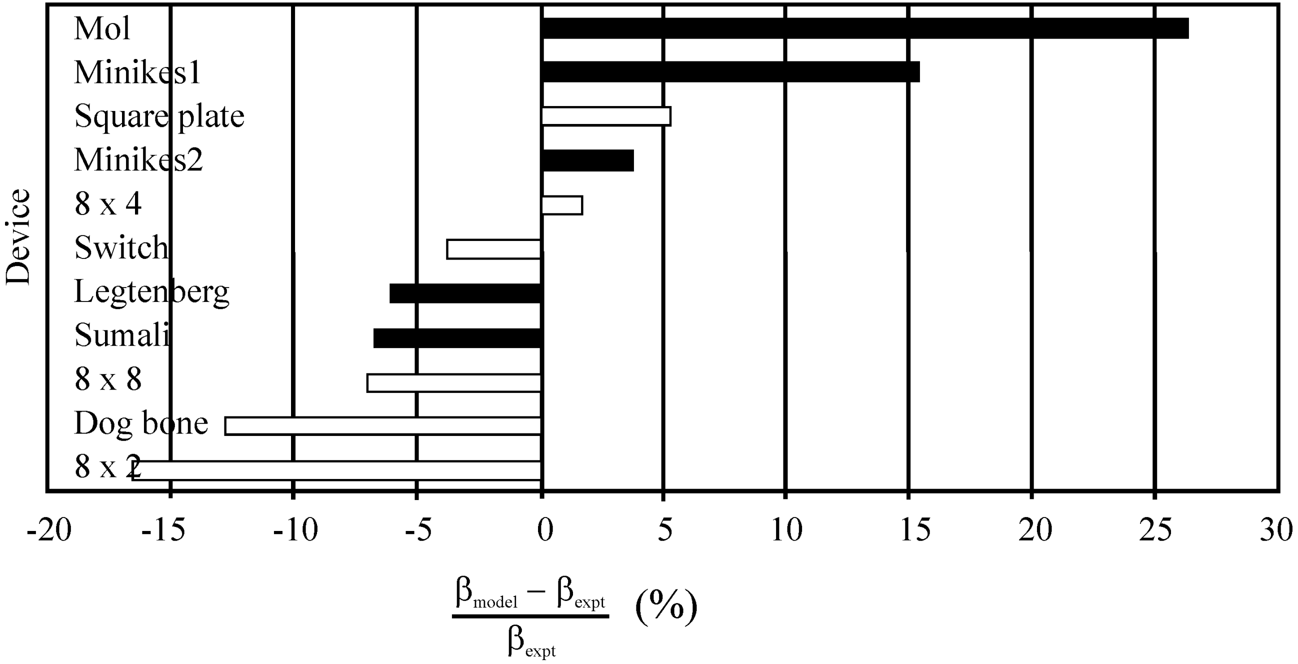

Figure 4: Deviation of model-predicted squeeze-film damping coefficient β_{model} from the experimental value β_{expt} of devices investigated in this thesis and in Refs. [1, 2, 3, 4]. The unfilled bars represent observations on our own devices.

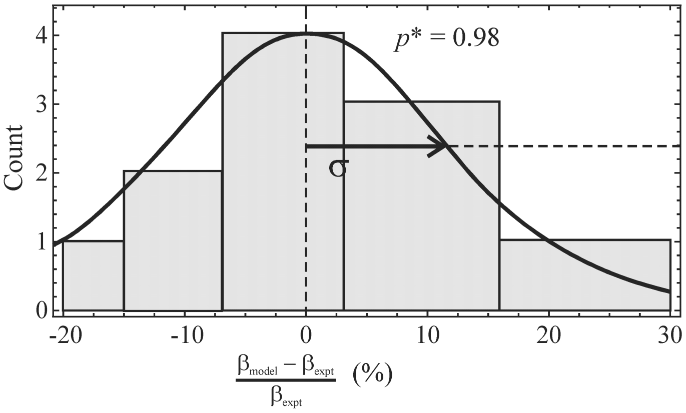

Figure 5: Histogram of the deviations of the eleven different resonators. The smooth curve denotes a Normal distribution with $\sigma = 0.12$.

4 Discussion

If we consider the deviation of β_{model} from β_{expt} for the devices presently investigated, we find that our model deviates from the experimental values quite randomly, exhibiting overratings as well as underratings. Including the relative deviations for the devices investigated in chapters 2 and 3, we have a total of eleven observations on different resonators giving evidence for our model with a standard deviation of 12% (Fig. 4). The devices cover a wide range of values of the device area A, gap width d and characteristic parameter $\omega_0\tau$, which gives this comparison a solid basis and thus avoiding any accidental coincidence of the model with experiments. This value of the variance in the difference between model and experiment should be compared to the standard deviation of the experimental results, as given in Tab. 3. These experimental errors are estimated to be on the order of 5%, although it is a tough job to assess the work of four different authors. As a check we have tested that the deviations are distributed according to a Normal distribution with $\sigma = 0.12$ using a chi-square statistic. Figure 5 illustrates the count distribution. The p-value is 0.98, implying that discrepancies greater or equal to the one observed are 98% of the time due to coincidence. This result is rather convincing in showing that the model gives a reliable result, free of large systematic errors. As discussed in chapter 3, the model does include approximations that are on the order of 10%.

5 Concluding remarks

Figure 5 leaves us with a Gaussian distribution for the relative differences between model and experiments with a standard deviation of 12%. Taking into account the approximations in the model – roughly estimated on 10% –, we can conclude that our model is fully adequate as a reliable tool for designing MEMS resonators. The single parameter that has to be evaluated numerically is the escape time τ, which is based on a simple Monte Carlo calculation taking up a few minutes. In this way we can design MEMS devices on a basis of software only, getting rid of the hardware approach of trial and error in short loop experiments in the micro-electronics fabrication plant. This approach saves the industry a vast amount of elapsed time and thus money.

References

[1] L. Mol, L.A. Rocha, E. Cretu, R.F. Wolffenbuttel, J. Micromech. Microeng. **19** (2009) 074021.

[2] H. Sumali, J. Micromech. Microeng. **17** (2007) 2231-2240.

[3] R. Legtenberg and H.A.C. Tilmans, Sens. Actuators A **45** (1994) 57-66.

[4] A. Minikes, I. Bucher, G. Avivi, J. Micromech. Microeng. **15** (2005) 1762-1769.

[5] R.D. Blevins, Formulas for Natural Frequency and Mode Shape (Florida: Krieger), 1995 pp 108, 159.

[6] G. Hong, W. Ye, Phys. Fluids **22**, 012001 (2010).

[7] R. G. Christian, Vacuum **16** (1966) 175-8.

Chapter 7

Conclusions

Reviewing the discoveries and results presented, we conclude that the mechanical interaction with gas of typical microstructures used for timing, filtering and further applications of resonant sensing can be catched in a single formula. By the flow of gas in the narrow electrode gaps of these devices, or *resonators* as they are commonly called, resisting forces on the microstructure emerge, known as *squeeze-film damping*. In the formula derived, the influence of this flow on the squeeze-forces is accommodated by a time constant τ, characterizing the flow resistance in the (coupled) electrode gaps. By simple modification according to the resonator's basic equation of motion, our formula of squeeze-forces reflects the effect of gas pressure on the characteristic parameters of resonators, which are Q-factor and resonance frequency ω_0. This result is excellent news with regard to designing reliable, accurate resonators for new MEMS applications and for assessing gas pressure/composition in resonators during fabrication. Time-consuming and labor-intensive improvement cycles of device design involving non-standard measurements and analysis can be avoided, thereby saving a lot of money for the industry.

Because of the small width of the gaps and reduced pressure in typical resonator packages, squeeze-film flow will behave in a free molecular fashion and gas molecules perform straight-line, randomly oriented gap-crossings when entering or leaving the gaps between resonator electrodes. Following this picture of gap flow, the time constant τ is appropriately represented by the average travel time of the molecules out of the gap and accurate numerical values can be found using rather simple simulation routines on an every-day computer system. These so called Test Particle Monte Carlo (TPMC) simulations track the trajectories of molecules in a rectangular bounding box which is usually a good representative of the gap geometries in resonators. The best aspect of this molecule tracing method is that implementing important geometrical details for the flow in gaps, like etch holes and trenches in the resonator structures, can be done with limited additional effort. This allowed us to straightforwardly simulate the damping of plates riddled with holes where simulations based on continuum flow would have needed sophisticated tricks. Another benefit is the straightforward dependence of the time constant on device temperature and molecular mass number, as the variable of average molecular speed occurs explicitly in the time expression for a single gap-crossing. The effect of temperature and gas species on squeeze-forces can thus readily be analyzed.

A challenge for future research would be to adapt the simulation routines used for more arbitrarily shaped gap geometries. Cylindrical boundaries on flat substrates do appear in for instance ring-shaped resonators which vibrate in the plane of substrate. The gaps involved would not be represented correctly by a rectangular bounding box and tracing consecutive gap-crossings at the cylindrical boundaries would require a more extensive collision detection method like in optical ray tracing. A TPMC routine with this ability then would be an essential add-on of future MEMS design software.

7.1 Acknowledgments

Performing this PhD-on-design during the last three years was a fantastic experience and this thesis awards my education as a physics engineer and designer which I started in 2005. For this, the help and attention of a few people has been indispensable. First of all, I would like to thank my promotor, Herman Beijerinck, for the opportunity to work with inspiring and ambitious people within NXP on such challenging subject. His supervision, stimulation and conditioning (write 'appendices' and have others comment on them!) has released an energy and focus in me which let me use my creativity on all design and research activities that have passed. Also today I still benefit from it with the planning and execution of all activities in my new job.

In addition I thank Jan-Jaap Koning for his help and involvement with my project in the last years. In his former position as *device physicist* of NXP and as such involved with NXP's MEMS oscillator project, he always challenged me to collaboration in the research project team and increased my awareness of the developments that one is faced as a designer/engineer in such business driven project. Furthermore I remember the pleasant atmosphere and inspiring company of his colleagues and students with our talks in Nijmegen which stimulated my activities a lot.

As next, but for the achieved result not less important persons, I thank Marcel van Gils, Reinout Woltjer and Joost van Beek. Marcel's efforts in defining project goal, realizing an important vacuum setup for testing MEMS resonators, providing expertise in FEM simulations have been the reason in the first place to start with investigations and design activities. First at the NXP production and innovation center in Nijmegen as part of my designer's education programme and consequently for this PhD on design building on the results obtained so far. As groupleader of the ”Microsystems technology” research group within NXP Eindhoven Reinout provided a pleasant working space and atmosphere in which I amongst the other researchers of the group felt home. Joost van Beek as projectleader of the MEMS oscillator project supported me with my efforts to process MEMS pressure sensors in the frame of the project and do the characterization on a dedicated setup in the lab.

Kim Le Phan helped me several times with these sensitive measurements to make signal processing and data recording successful. For that I am very grateful to him and Cas van der Avoort (vibrometer measurements) who also participated in the team.

Further acknowledgments are made to the PointOne project ”MEMSLand” which supported this PhD on design financially (`www.memsland.nl`).

Finally, I thank my family and friends for their interest in my work and all nice diversion outside work to recreate myself for every challenge.

Chapter 8

Summary

The massive integration of micromechanical structures on ICs to allow microsystems to sense and control the environment is expected to be one of the most important technological breakthroughs of the future. At present, cheap and small MEMS sensors are emerging in countless applications. Automotive and telecommunication industry have fueled the biggest R&D effort so far in this area. Prominent results, among others, are the accelerometer guarding the safety systems in vehicles, the miniature microphone in cellphones and inkjet printing heads.

Although miniaturization is the main driver of MEMS development in industry – reducing cost by decreasing material consumption and allowing batch fabrication, MEMS offer an important collateral benefit with respect to traditional systems: an increase of applicability and reliability. This development very much concerns existing microelectronic building blocks that by efficient integration with each other can grow to more functional, intelligent systems on the same chip. One such block is the crystal oscillator for frequency reference used in clocks, radios, computers and cellphones etc. to provide a stable clock signal for digital integrated circuits, and to stabilize frequencies for radio transmitters and receivers. Regarding the vast demand of timing devices for time-keeping and frequency reference applications, the research of MEMS based oscillators has a lot of attention. It is expected that these oscillators – built with a MEMS *resonator* – will offer smaller form factor, improved reliability, and lower solution cost than the common crystal oscillator with its IC incompatible quartz resonator. Efforts over recent years have shown that MEMS resonators are capable of high quality factor Q, exhibit low temperature drift and pair excellent phase noise performance to low power consumption.

As MEMS based oscillators need vacuum conditions for proper and reliable operation of the mechanical resonator, the packaging process of these devices must provide direct caps to the resonators that make a hermetic sealing. The life-time testing of these sealings pose a big challenge to in-situ pressure detection methods in resonator samples during fabrication. We have realized a sensitive pressure sensing operation of the resonator itself by reading out the damping forces exerted by the residual gas in an out-of-plane, low frequency resonance mode. No additional structures or signals other than the common resonance parameters, Q and ω_0, required!

The behavior of the damping forces in the resonator agrees well to a new model that we particularly developed for designing resonators as pressure sensors in the mbar range. Thanks to free molecular flow in the cavity of typical resonators these forces can be formulated analytically with just one parameter dependent on numerical evaluation. Because of the direct physical significance of this and other parameters in the derived formulas, the model provides valuable clues for the optimization of sensor design. It saves time-consuming trial-and-error loops of design and fabrication that would be needed alternatively.

The methods and results of this thesis demonstrate that out-of-plane, low frequency resonance mode operation of resonator samples establishes sensitive detection of cavity pressure offering cheap and easy life-time testing in industry. Our design-oriented model for the governing forces between residual gas and resonator structure holds for a multitude of different geometries within a margin of error of 12%, making model-based design of MEMS resonant pressure sensors to a reality.

8.1 Samenvatting

Een belangrijke technologische doorbraak van de toekomst is in vele ogen de naadloze wissel-/samenwerking van elektronica met de omgeving. Hierbij is de massa-integratie van (bewegende) micro-elementen in IC's om elektronica te laten 'voelen' een grote uitdaging. Zulke sensoren op microschaal (zogenaamde MEMS: Micro-ElektroMechanische Systemen) treffen we tegenwoordig aan in veel elektronica om ons heen. Hierbij vallen met name de toepassingen in auto's (airbag) en mobiele telefoons (smartphone) op. Belangrijke voorbeelden van MEMS zijn onder andere de accelerometer (versnellingsopnemer) voor de passieve en actieve veiligheidssystemen in onze auto's, de microfoon van mobiele telefoons maar ook het mechanisme van een printkop in inktjetprinters.

De ontwikkeling van MEMS komt voort uit de trend in de elektronica-industrie om nieuwe componenten te *miniaturiseren* zodat materiaalkosten gedrukt kunnen worden en gemakkelijk grote series gemaakt kunnen worden. Daarnaast hebben ook de afnemers van elektronica baat bij deze ontwikkeling omdat elektronische toepassingen in MEMS-uitvoering een toegenomen toepasbaarheid en betrouwbaarheid hebben. Hierbij kan men denken aan het kunnen integreren van bestaande, maar klassiek moeilijk verenigbare elektronische functies op één-en-dezelfde chip. Een van zulke functies is de kristaloscillator voor frequentiestabilisatie in klokken, radio's, computers en mobiele telefoons enz. Gezien de enorme vraag naar oscillatoren krijgt het onderzoek naar MEMS uitvoeringen van dit onderdeel steeds meer belangstelling. Verwacht wordt dat deze oscillatoren – met een MEMS *resonator* – in de kleinste toepassingen verwerkt kunnen worden, betrouwbaarder zijn en minder kosten dan de gangbare kristaloscillator met z'n IC-onverenigbare quartzkristal. Onderzoek van de laatste jaren toont aan dat MEMS resonatoren kunnen worden gemaakt met hoge kwaliteitsfactoren, lage temperatuurdrift vertonen en uitmuntende faseruisspecificaties koppelen aan laag energieverbruik.

Omdat micromechanisch geïntegreerde oscillatoren vacuumomstandigheden vereisen voor een juist en betrouwbaar functioneren van de resonator, moet de chipbehuizing zorgen voor een hermetisch 'deksel' op de resonator. Deze deksels van dunne (enkele micrometers) lagen materiaal maken het testen van het vacuum in de kleine holte tijdens productie tot een grote uitdaging. Dat testen is van belang omdat bij aanvankelijk goede resonatoren met een degradatie van het vacuum over enkele weken de betrouwbaarheid van de gehele MEMS oscillator voor de geplande levensduur in gevaar komt. Voor deze toepassing is er behoefte aan sensoren die binnenin de resonatorholte gevoelig vacuumdrukken kunnen detecteren. Wij hebben zo'n druksensor ontworpen bestaand uit een resonator waarvan de dempingskrachten een maat voor de absoluutdruk van het restgas zijn. Deze dempingskrachten zijn direct af te leiden uit de resonantiefrequentie en -amplitude waardoor signaalomzettingen overbodig zijn.

Het gedrag van de dempingskrachten op de resonator komt goed overeen met een nieuw model dat we speciaal hebben ontwikkeld voor het ontwerpen van resonatoren als druksensoren in het millibarbereik. Dankzij vrije moleculaire stroming in de holte van typische resonatoren kunnen deze krachten analytisch worden geformuleerd met slechts één numeriek te berekenen parameter. Wegens de directe fysische betekenis van deze en andere parameters in de afgeleide formules biedt het model nuttige aanwijzingen voor het optimaliseren van dit soort druksensoren. Het model versnelt het ontwerpwerk omdat tijdrovende iteraties met afwisselend specificeren, fabriceren, karakteriseren voor het bereiken van een bepaalde meetgevoeligheid voorkomen kunnen worden.

In het verlengde van ons druksensorontwerp en met het levensduurtesten van MEMS oscillatoren in gedachte, hebben we ontdekt dat het uit-het-vlak bedrijven van de resonator door de lage stijfheid al zo drukgevoelig is, dat er niet eens een aparte resonator voor het vacuumtesten nodig hoeft te zijn. Dit resultaat is een belangrijke verbetering voor levensduurtesten van MEMS resonatoren tijdens fabricage. Bovendien blijkt ons ontwerpgerichte model voor de optredende krachten tussen restgas en resonator te voldoen voor een veelheid aan geometrieën binnen een foutmarge van 12%. Dit bewijst het 'model-based' ontwerpen van MEMS resonatoren voor drukmeting in de praktijk.

8.2 Curriculum vitae

Matthijs Alexander Gerard Suijlen (1979) werd geboren in Gouda en studeerde, na doorlopen van het Coornhert Gymnasium in dezelfde plaats, natuurkunde aan de Universiteit Leiden (Masterdiploma in 2004). In 2005 specialiseerde hij zich verder in technologie en ontwerp van fysische instrumentatie bij de Technische Universiteit Eindhoven en behaalde in 2008 het diploma van deze op-ontwerpen-gerichte opleiding (DTI).

Van 2008 tot 2011 heeft hij een promotie-op-proefontwerp ('PhD on design') verricht op een MEMS druksensor in de researchafdeling van NXP Semiconductors te Eindhoven. De werkzaamheden hiervoor zijn integraal uitgevoerd binnen een industriëel project voor de ontwikkeling van MEMS oscillatoren. De ontworpen MEMS druksensor is gepatenteerd en beschreven in het proefschrift ”Model-based design of MEMS resonant pressure sensors”. De werkingsprincipes zijn eveneens gepubliceerd in een toonaangevend wetenschappelijk tijdschrift voor microsystemen.

Sinds februari 2011 werkt hij voor TMC Physics als 'development engineer' van MEMS scanning microspiegels bij Innoluce BV in Eindhoven (`www.innoluce.com`). Genoemde spiegels worden o.a. gecommercialiseerd voor lasergedreven pico-projectoren.